

AD-A100 812

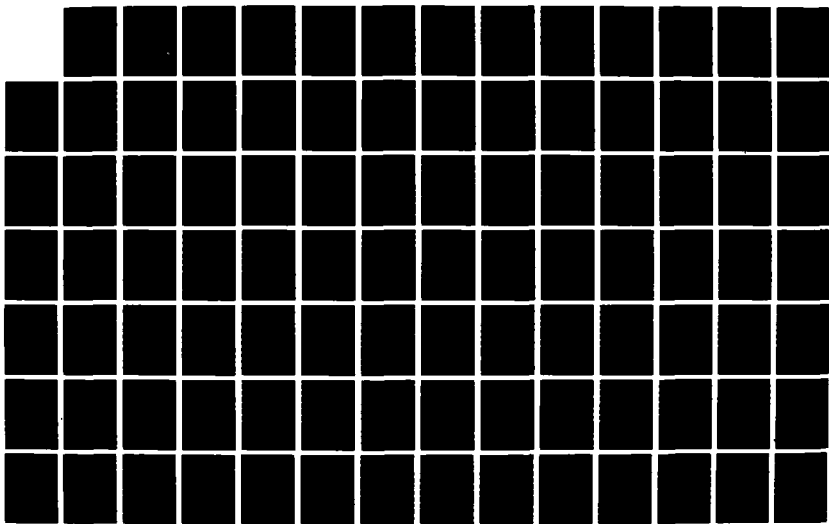
ON THE NATURE OF OBLIQUE INSTABILITY WAVES IN BOUNDARY
LAYER TRANSITION(U) CALIFORNIA INST OF TECH PASADENA
GRADUATE AERONAUTICAL LABS H F ROBEY 23 MAY 66
N00014-65-K-6265

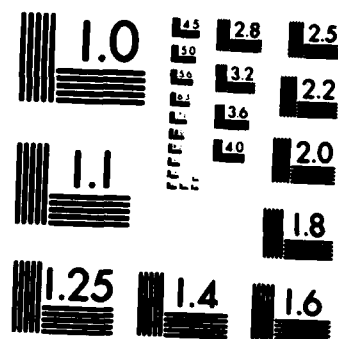
1/2

UNCLASSIFIED

F/G 28/4

NL





MICROCOPY RESOLUTION TEST CHART
NATIONAL BUREAU OF STANDARDS 1963 A

DTIC FILE COPY

4

12

GRADUATE AERONAUTICAL LABORATORIES CALIFORNIA INSTITUTE OF TECHNOLOGY

ON THE NATURE OF OBLIQUE INSTABILITY WAVES
IN BOUNDARY LAYER TRANSITION

Thesis by

Harry F. Robey III

N00014-85-K-0205

AD-A188 812

DTIC
ELECTE
DEC 04 1987
S H D

Firestone Flight Sciences Laboratory

Guggenheim Aeronautical Laboratory

Karman Laboratory of Fluid Mechanics and Jet Propulsion

DISTRIBUTION STATEMENT A

Approved for public release;
Distribution Unlimited

87 10 13 013

Pasadena

**ON THE NATURE OF OBLIQUE INSTABILITY WAVES
IN BOUNDARY LAYER TRANSITION**

**Thesis by
Harry F. Robey III**

**Report on Work Performed under Contracts
N00014-85-K-0205 and N00014-81-K-0551
for the Office of Naval Research**

**Also Submitted in Partial Fulfillment of
the Requirements for the Degree of
Doctor of Philosophy**

**California Institute of Technology
Pasadena, California**

1986

Submitted May 23, 1986



Accession For	
NTIS GRA&I	<input checked="checked" type="checkbox"/>
DTIC TAB	<input type="checkbox"/>
Unannounced	<input type="checkbox"/>
Justification	
By	
Distribution/	
Availability Codes	
Dist	Avail and/or Special
A-1	

© 1986

Harry F. Robey III

All Rights Reserved

- iii -

DEDICATION

to my parents

ACKNOWLEDGEMENTS

I wish to thank my advisor, Professor Hans W. Liepmann, for his continual support, encouragement, and enthusiasm through the years. The help and advice in the laboratory provided by Professor Dan M. Nosenchuck and Dr. Stephen E. Taylor were also greatly appreciated, as were the many stimulating discussions with Dr. Thomas Sobota.

In addition, I would like to thank all the members of the GALCIT community for their help and friendship throughout my years at Caltech.

This research was supported by the Office of Naval Research, contract nos. N00014-81-K-0551 and N00014-85-K-0205.

ABSTRACT

An experimental study of both the weakly non-linear as well as the three-dimensional nature of boundary layer transition is conducted using the active surface heating technique, of Liepmann et al. In the present study, this technique is extended to provide a means for controllably and repeatably introducing three-dimensional disturbances into a laminar boundary layer. A review of the surface heating technique is presented along with a discussion of some peculiarities encountered in extending this technique to three-dimensional geometries. A thorough description of the design and operation of a programmable 32-element heater array and the supporting instrumentation are also given.

The heater array is first used to study the effect of weak non-linearity on boundary layer transition. By keeping the forced disturbances as two-dimensional as possible, it is shown that the effects of weak non-linearity are relatively benign. The growth rates are seen to follow the linear theory up to perturbation amplitudes (r'_w/r') of nearly twelve percent. The only deviation from the linear theory arises in the form of non-linearly generated harmonics phase-locked to the fundamental. It is concluded that although these non-linearly generated harmonics do alter the wave behavior to some extent, they are by themselves not sufficient to explain the transition from small linear oscillations to the large amplitude, broad-band, three-dimensional oscillations characteristic of a fully turbulent boundary layer.

The effect of three-dimensionality on boundary layer transition is then investigated through an analytical and experimental study of single oblique instability waves. This subject has remained largely unexplored, as such disturbances were generally thought to be more stable and therefore less dangerous than their two-dimensional counterparts. Through a series of experiments, however, it is shown that certain conditions exist for which oblique waves are observed to be more unstable than any two-dimensional wave. It is shown that oblique waves exhibit a non-stationary period-doubling behavior that

is not seen in two-dimensional disturbances. A vortex pairing mechanism is proposed to explain this behavior, and is shown to occur in a manner consistent with the Biot-Savart law for the induced velocity field. (Planned)

TABLE OF CONTENTS

Chapter	Page
Copyright	ii
Dedication	iii
Acknowledgements	iv
Abstract	v
Table of Contents	vii
List of Figures	x
List of Symbols	xiii
1.0 INTRODUCTION	
1.1 Background and Motivation	1
1.2 Objective of Present Study	5
1.3 Active Surface Heating Technique	7
1.4 On Comparisons with Other Experiments	11
2.0 EXPERIMENTAL FACILITY AND INSTRUMENTATION	
2.1 GASCIT High Speed Water Tunnel	14
2.2 Flat Plate Model	14
2.3 Flow Documentation	16
2.4 Phased Heater Array	17
2.5 Instrumentation	17
2.6 Flow Diagnostics and Data Acquisition	20
3.0 TWO DIMENSIONAL WAVE EXCITATION	
3.1 Introduction	22
3.2 Experimental Conditions	24

3.3	Results for Single Mode Excitation	24
3.3.1	Disturbance Growth Rates	24
3.3.2	Generation of Higher Harmonics	27
3.3.3	Frequency Dependence	28
3.3.4	Summary of Observed Non-Linear Effects	29
4.0	GEOMETRICAL NATURE OF OBLIQUE WAVES	
4.1	Introduction	30
4.2	Spatial Growth Rates	31
4.3	On the Direction of Propagation	32
4.3.1	The Nature of Viscous Instability	35
4.4	A Look at the Vorticity Field	37
4.5	Three-Dimensional Stability Theory Revisited	39
5.0	THREE-DIMENSIONAL, OBLIQUE WAVE EXCITATION	
5.1	Introduction and Preliminary Observations	43
5.2	The Onset of Non-Stationary Behavior	45
5.2.1	Time Series Behavior	46
5.2.2	Frequency Analysis of Non-Stationary Signals	46
5.2.3	Comparison with Proposed Resonance Mechanisms	48
5.2.4	An Alternative Mechanism : Vortex Pairing	49
5.3	Results for Oblique Wave Excitation	50
5.3.1	Frequency Dependence	50
5.3.2	Wave Angle Dependence	52
5.3.3	Amplitude Dependence	54
5.3.4	Eigenfunction Behavior	55
5.4	Summary of Three-Dimensional Effects	57

6.0	CONCLUSION	59
-----	------------	----

APPENDICES

A	Similarity Analysis of the Surface Heating Technique	63
---	--	----

B	Present Implementation of the Wigner Distribution	65
---	---	----

C	Microprocessor Control and Data Acquisition System	70
---	--	----

	REFERENCES	76
--	------------	----

	FIGURES	80
--	---------	----

List of Figures

Figure		Page
1.1	Neutral Stability Curve	80
1.2	Comparison Between Wall-Shear Fluctuations and Velocity Fluctuations	81
2.1	GALCIT High-Speed Water Tunnel (HSWT)	82
2.2	Schematic of Flat Plate Model	83
2.3	Mean Velocity Profile	84
2.4	Phased Heater Array	85
2.5	Schematic of Phased Heater Array Control Electronics	86
2.6	Power Amplifier Circuit	87
2.7	Three-Dimensional Views of T. S. Wave "Surfaces"	88
2.8	Constant Temperature Anemometer Circuit	89
3.1	Naturally Occuring Tollmien-Schlichting Waves	90
3.2	Forced Two-Dimensional Tollmien-Schlichting Waves	91
3.3	Two-Dimensionality of Forced Waves	92
3.4	Disturbance Amplitude vs. Forcing Level	93
3.5	Growth Rate vs. Disturbance Amplitude	94
3.6	Time Series Behavior of Fundamental and First Harmonic	95
3.7	Amplitude of First Harmonic vs. Forcing Level	96
3.8	Amplitude of First Harmonic vs. Amplitude of Fundamental	97
3.9	Appearance of Higher Harmonics	98
3.10	Frequency Dependence	99
4.1	Spanwise Amplitude Distribution for a Single Oblique Mode	100
4.2	Phase Velocity vs. Spanwise Wavenumber	101
5.1	Disturbance Amplitude vs. Frequency for Oblique Waves	102

5.2	Time Series Behavior of a 15° Oblique Wave	103
5.3	Wigner Transform of a Non-Stationary Time Signal	104
5.4	Altered Streamline Pattern due to Vortex Pairing	105
5.5	Time Series Response vs. Forcing Frequency for Two-Dimensional Waves	106
5.6	Spectral Response vs. Forcing Frequency for Two-Dimensional Waves	107
5.7	Time Series Response vs. Forcing Frequency for 10° Oblique Waves	108
5.8	Spectral Response vs. Forcing Frequency for 10° Oblique Waves	109
5.9	Time Series Response vs. Wave Angle	110
5.10	Spectral Response vs. Wave Angle	111
5.11	Integrated Amplification vs. Wave Angle (Mack)	112
5.12	Geometry of Oblique Waves	113
5.13	Time Series Response vs. Forcing Amplitude	114
5.14	Eigenfunction Behavior for Oblique Waves	115
A.1	Geometry for Similarity Analysis of Heating Technique	116
B.1	Wigner Transform of a Stationary Signal	117
B.2	Wigner Transform of a Non-Stationary Signal	118
B.3	Wigner Transform of a Signal Containing Two Stationary Contributions	119
B.4	A Detailed Look at the Wigner Transform of Figure B.3	120
B.5	The Result of Low-Pass Filtering on the Wigner Transform	121
C.1	Experimental Aparatus	122
C.2	Block Diagram of the Central Processing Unit (CPU)	123
C.3	Block Diagram of the CPU / Peripheral Interface	124

C.4 Circuit Diagram of the Phased Heater Array Control Electronics 125

List of Symbols

Symbol	Description
A	Disturbance Amplitude
b	Spanwise Length of Heater
c	Disturbance Phase Velocity, ω/α_r
C_f	Skin Friction Coefficient, $\tau_w/\frac{1}{2}\rho U_\infty^2$
C_g	Disturbance Group Velocity, $\partial\omega/\partial\vec{\kappa}$
D	Operator Notation for $\partial/\partial y$
f	Disturbance Frequency
F	Non-Dimensional Disturbance Frequency
H_{fe}	Current Gain Factor for Darlington Power Transistors
k	Thermal Conductivity
L	Streamwise Length of Heater
p	Static Pressure
Pr	Prandtl Number, ν/κ
\vec{q}	Local Heat Flux Vector
\vec{Q}	Integrated Heat Flux Vector
R	Heater Resistance
Re	Reynolds Number
t	Time, or Heater Thickness
T	Temperature
u	Streamwise Component of Disturbance Velocity Field
U	Mean Velocity
v	Vertical Component of Disturbance Velocity Field
V	Heater Voltage
w	Spanwise Component of Disturbance Velocity Field
$W(t, f)$	Wigner Transform

x	Streamwise Distance Measured from the Plate Leading Edge
y	Distance Normal to Surface of Plate
z	Spanwise Distance Measured from the Plate Centerline
α	Streamwise Wavenumber of the Disturbance
β	Spanwise Wavenumber of the Disturbance
δ^*	Boundary Layer Displacement Thickness, $\int_0^\infty (1 - u/U_\infty) dy$
δ_T	Thermal Boundary Layer Thickness, $(3\mu\kappa\xi/\tau_w)^{1/3}$
ΔT	Temperature Difference, $T_w - T_\infty$
η	Similarity Coordinate, y/δ_T
κ	Thermal Diffusivity
$\vec{\kappa}$	Disturbance Wavenumber Vector
λ_x	Streamwise Disturbance Wavelength, $2\pi/\alpha$
λ_z	Spanwise Disturbance Wavelength, $2\pi/\beta$
μ	Dynamic Viscosity
ν	Kinematic Viscosity
ξ	Streamwise Distance as Measured from the Heater Leading Edge
ρ	Density
τ_w	Wall-Shear Stress
θ	Oblique Wave Angle, $\tan^{-1}(\beta/\alpha)$
ω	Angular Frequency of Disturbance, $2\pi f$
$\vec{\omega}$	Vorticity Field of the Disturbance

Subscripts

f	Fluid
s	Substrate
t	Total
w	Value Evaluated at the Wall
∞	Free-Stream Value

CHAPTER 1

INTRODUCTION

1.1 Historical Background and Motivation

The subject of boundary layer transition has been of great interest for over fifty years and remains a very active area of research. Historically, the most fruitful method by which transition has been studied is a consideration of the stability of small amplitude disturbances of the form

$$\bar{u}(\bar{x}, t) = \bar{u}(y)e^{i(\alpha x - \omega t)} \quad (1.1)$$

where α is the streamwise wavenumber, and ω is the frequency of the disturbance. Both α and ω are in general complex. Disturbances of the form 1.1 are most commonly referred to as Tollmien-Schlichting waves after a series of fundamental papers by Tollmien and Schlichting from 1929 to 1940. When a velocity field of the form 1.1 is substituted into the linearized equations of motion, a fourth order eigenvalue problem results and is typically written in terms of the vertical component of the disturbance velocity field $v(y)$ as

$$v'''' - 2\alpha^2 v'' + \alpha^4 v = i\alpha Re \left[\left(U - \frac{\omega}{\alpha} \right) (v'' - \alpha^2 v) - U'' v \right] \quad (1.2)$$

$U = U(y)$ is the mean velocity profile, and Re is the Reynolds number. Equation 1.2 is the Orr-Sommerfeld equation derived independently by Orr (1907) and Sommerfeld (1908). Solutions are easily obtained by numerical methods and are usually represented in terms of the neutral stability curve, an example of which is given in figure 1.1. The existence of such travelling wave disturbances was firmly established in the classical experiments of Schubauer and Scramstad (1947) in which two-dimensional oscillations were artificially introduced into a laminar boundary layer by means of an electromagnetically excited vibrating metal ribbon. Aided by the extremely low turbulence level (0.02 National Bureau of Standards' wind tunnel, Schubauer and Scramstad were able to verify the linear theory in virtually every respect.

The existence of the disturbances predicted by the linear theory has thus been established beyond doubt, yet the connection between these small amplitude, low frequency, slowly growing oscillations and the complicated, three-dimensional phenomenon of turbulence still remains unclear. Two primary directions have been pursued in an attempt to relate these two phenomena. One approach is a consideration of non-linearity in the development of finite amplitude oscillations. This approach has been taken by numerous investigators, and is admirably reviewed in a recent survey by Herbert (1984). Though the results of the various analyses vary in specific details, the general conclusion reached by this line of investigation is that non-linearity alters the growth rates and the region of unstable parameter space only slightly and cannot in and of itself explain the transition from linear oscillations to fully developed turbulent flow.

Essential to a more complete understanding of the transition process is some account of the origin of three-dimensionality in the flow. As early as 1933, Squire related the stability of three-dimensional disturbances in the form of oblique waves given by

$$\bar{u}(\bar{x}, t) = \bar{u}(y) e^{i(\alpha x + \beta z - \omega t)} \quad , \quad \beta = \frac{2\pi}{\lambda_s} \quad (1.3)$$

to the well understood two-dimensional problem. By a simple scaling argument, Squire showed that the stability of oblique waves was governed by an equation of the form 1.2, and thus the eigenvalues and eigenvectors could be obtained for this type of three-dimensional disturbance just as in the two-dimensional case. The principal result to come from this analysis was the observation that the minimum critical Reynolds number for disturbances of the form 1.3 occurs for the purely two-dimensional case, $\beta = 0$. It is at least partly for this reason that in the 50 years since Squire's analysis, very few experiments exploring the stability characteristics of oblique waves have been conducted. Such disturbances were generally considered to be more stable and therefore less dangerous than two-dimensional disturbances.

It was not until the experiments of Klebanoff, Tidstrom, and Sargent (1962) that

interest in the three-dimensional nature of boundary layer transition began to grow. In those experiments, it was noticed that the boundary layer tended to develop a spanwise modulation in the disturbance amplitude with a seemingly preferred spanwise wavelength, λ_z . This behavior was enhanced by placing physical disturbances on the surface of a flat plate at pre-selected spanwise intervals. A very regular "peak-valley" structure of the disturbance waveform was then clearly seen. The "peaks" correspond to regions of maximum wave amplitude and the "valleys" to regions of minimum amplitude.

Recent flow visualization studies by Saric et al. (1984) and Kachanov and Levchenko (1984) have suggested that this peak-valley corrugation of the boundary layer can occur in two fundamentally different geometrical patterns. The first pattern, which was observed by Klebanoff and co-workers, is characterized by an alignment of successive peaks in the streamwise direction; i.e. peaks follow peaks and valleys follow valleys. An alternative pattern is one in which a staggered structure develops; i.e. peaks follow valleys and vice versa.

Numerous mechanisms have been proposed in an attempt to explain and predict these various three-dimensional wave patterns. Most mechanisms involve a weakly non-linear resonance phenomenon between a two-dimensional Tollmien-Schlichting wave and some form of three-dimensional wave. The following table lists several of the resonance mechanisms which have been proposed:

Table 1.1 Various Proposed Resonance Mechanisms

Author	Model
Benny and Lin (1960) Benny (1961) Stuart (1962,1971)	$Ae^{i(\alpha z - \omega_1 t)} + B(\cos \beta z)e^{i(\alpha z - \omega_2 t)}$
Herbert and Morkovin (1980) Itoh (1980)	same as above, but to 3 rd order in A,B
Craik (1971)	$Ae^{i(\alpha z - \omega t)} + Be^{i(\frac{1}{2}\alpha z \pm \beta z - \omega t)}$
Raetz (1959,1970)	$Ae^{i(\alpha_1 z - \omega_1 t)} + Be^{i(\alpha_2 z + \beta z - \omega_2 t)} + Ce^{i(\alpha_3 z + \beta z - \omega_3 t)}$ $\alpha_1 = \alpha_2 + \alpha_3, \quad \omega_1 = \omega_2 + \omega_3$
Nayfeh and Bozatli (1979)	$Ae^{i(\alpha z - \omega t)} + Be^{i(2\alpha z - 2\omega t)} + Ce^{i(\alpha z + \beta z - 2\omega t)}$
Herbert and Morkovin (1980)	$Ae^{i(\alpha z - \omega t)} + Be^{i\beta z}$
Benny and Gustavson (1981)	$Ae^{i(\alpha z + \beta z - \omega t)} + \text{"Squire Modes"}$

Each model differs in the exact form of the three-dimensional wave chosen, but all predict growth rates for the assumed disturbances that are in excess of those predicted by the linear theory alone. The so called "Squire modes" of the Benny-Gustavson model are solutions of the linearized equations of motion of the form 1.3 but with zero vertical component of the disturbance velocity field, i.e. $v(y) = 0$. Such disturbances consist of streamwise and spanwise periodic arrays of vertical vortices and were found by Squire (1933) to be everywhere stable. They are variously termed "Squire modes" or "vertical vorticity modes" in the literature.

In addition to the above mentioned resonance mechanisms, several analyses have been put forth treating the onset of three-dimensionality as a secondary instability problem. Currently receiving much attention is the analysis of Herbert (1983,1984) which employs Floquet theory to study the instability of a streamwise periodic base flow consisting of a mean flow profile plus a Tollmien-Schlichting wave that is neither growing nor being damped. This is strictly valid only for Pouiseuille flow, but is suggested to provide

a plausible mechanism for the boundary layer as well. This analysis is appealing in that it provides theoretical support for both the corrugated three-dimensional breakdown seen by Klebanoff et al. as well as the staggered structure of Saric and Kachanov.

1.2 Objective of present study

Apart from those studies already mentioned, experimental investigations into the three-dimensional nature of boundary layer transition remain few and far between. At least partly responsible for the lack of experimental studies is the fact that there has not existed a good technique for introducing three-dimensional perturbations into a laminar flow in a controllable and repeatable manner. It is a primary goal of this research to describe such a technique.

The technique used throughout the experiments is the active surface heating technique introduced by Liepmann, Brown, and Nosenchuck (1982). A review of the surface heating technique will be presented in the following section along with a discussion of some peculiarities introduced by the use of such a technique for forcing in three-dimensional geometries. Chapter 2 will then describe the design and operation of the fully programmable 32-element heater array and supporting instrumentation used in the present experiments.

A second goal of this study is to attempt to separate as much as possible the role of non-linearity from the role of three-dimensionality in the rapid breakdown of a laminar boundary layer flow. To that end, chapter 3 will be devoted entirely to a study of two-dimensional, non-linearly developing disturbances. It will be shown that non-linearity manifests itself primarily in the generation of higher harmonics which are related to the self-interaction of the fundamental wave with itself. It will be further shown that rather large amplitude two-dimensional waves can be easily generated when three-dimensional

effects are kept to a minimum. This chapter will serve the dual role of demonstrating the phased heater array capabilities on a relatively well known flow (2-D T.S. waves) while at the same time establishing a reference for further work on three-dimensional waves.

As three-dimensional disturbances are considerably more complicated and have been theoretically and experimentally studied in much less detail, we restrict our attention for the present study to one particular form of three-dimensional disturbance; that of oblique waves. These disturbances are perhaps the most fundamental type of three-dimensional disturbance, as they are normal modes of the linearized equations of motion. It is curious to note that although oblique waves are widely used in theoretical studies (as can be seen in table 1.1), virtually no experimental data exists on this type of disturbance. In order to establish a framework for the experimental work, Chapter 4 will be devoted to a detailed discussion of some of the unique properties of oblique waves. It will be seen that while many similarities between oblique waves and two-dimensional waves exist, a number of striking differences are to be found as well.

Finally, Chapter 5 will present some experimental results on the behavior of forced oblique waves. It will be shown by careful analysis of the fluctuating wall-shear time series and of the disturbance eigenfunctions that oblique waves exhibit inherently non-stationary behavior. This behavior will be analyzed in light of the geometrical structure revealed in Chapter 4, and will be shown to be consistent with a simple mechanism which has been known to play a fundamental role in shear flow development for many years, that of vortex pairing. The relation of the present results to ideas prevalent in the current literature will be discussed, and extensions to other related shear flows (wakes, shear layers, jets, etc.) will be made.

1.3 Active Surface Heating Technique

Throughout the present experiments, the active surface heating technique introduced by Liepmann and Nosenchuck (1981) was used to excite various three-dimensional normal modes of the boundary layer. The technique is based on the viscosity-temperature relation of the fluid. Using an analysis similar to that of Nosenchuck (1982), we consider the zero pressure gradient, x -momentum, boundary layer equation with variable viscosity, $\mu = \mu(T) = \mu(y)$:

$$\frac{\partial u}{\partial t} + u \frac{\partial u}{\partial x} + v \frac{\partial u}{\partial y} = \frac{1}{\rho} \frac{\partial \tau}{\partial y} = \nu \frac{\partial^2 u}{\partial y^2} + \frac{1}{\rho} \frac{\partial \mu}{\partial y} \frac{\partial u}{\partial y} \quad (1.4)$$

Rearranging,

$$\frac{\partial u}{\partial t} + u \frac{\partial u}{\partial x} + (v + v_{eff}) \frac{\partial u}{\partial y} = \nu \frac{\partial^2 u}{\partial y^2} \quad (1.5)$$

where we have defined an "effective" vertical velocity,

$$v_{eff}(y) = -\frac{1}{\rho} \frac{\partial \mu}{\partial T} \frac{\partial T}{\partial y} \quad (1.6)$$

As it is well known that the boundary layer is most susceptible to disturbances in the vicinity of the critical layer (see for example Lin (1955) and Meier and Maier (1984)), we would like to evaluate expression 1.6 at the critical layer, y_{cr} . We therefore need an expression for the temperature profile $T(y)$ above the heater.

An approximate expression for the temperature profile under the conditions of steady, parallel, two-dimensional boundary layer flow can be derived by a similarity analysis. The full analysis is given in appendix A, but for the present only the result is needed. We take as the similarity variable

$$\eta = \frac{y}{\delta_T} \quad , \quad \delta_T = \left(\frac{3\mu\kappa\xi}{\tau_w} \right)^{1/3} \quad (1.7)$$

where ξ is the streamwise distance measured from the leading edge of the heater. This is shown schematically in figure A.1. Above the heater, the temperature profile is then

given by

$$T(\eta) = T_w + 0.776\Delta T \int_0^\eta e^{-\eta^3/3} d\eta \quad (1.8)$$

where T_w is the temperature at the wall, and $\Delta T = (T_\infty - T_w)$ is the temperature difference between wall and freestream. Combining 1.8 and 1.6, we obtain

$$v_{eff}(\xi, y) = -\frac{1}{\rho} \frac{\partial \mu}{\partial T} \left[0.776\Delta T \frac{e^{-\eta^3/3}}{(3\mu\kappa\xi/\tau_w)^{1/3}} \right] \quad (1.9)$$

It is desirable to express the temperature difference ΔT in terms of quantities easily measurable in the laboratory. We can relate ΔT to the total heat flux Q_f introduced into the flow by

$$Q_f = b \int_0^L q_w d\xi \quad (1.10)$$

where b is the heater span and L the streamwise length of the heater. Evaluating $q_w = -k\partial T/\partial y$ from 1.8, equation 1.10 becomes

$$Q_f = 0.807k\Delta T b (Pr Re_L^2 C_f)^{1/3} \quad (1.11)$$

It may be noted that this is exactly the same relation that would be obtained through the use of Lighthill's heat transfer formula.

Q_f may be further related to the total power delivered to the heater, $Q_t = V^2/R$. Following the analysis of Taylor (1986), we take

$$Q_t = Q_f \left(1 + \frac{Q_s}{Q_f} \right) \quad (1.12)$$

where Q_s is the heat transferred to the substrate via conduction. This conduction loss can be estimated by assuming that the length scale over which the substrate temperature gradients are maintained will scale with the frequency of the forcing, ω ; i.e. the relevant length scale in the substrate is $\theta_s \approx (\kappa_s/\omega)^{1/2}$. Thus we obtain

$$Q_s \approx k_s \Delta T \left(\frac{\kappa_s}{\omega} \right)^{-1/2} bL \quad (1.13)$$

Combining with 1.11,

$$\frac{Q_s}{Q_f} \approx \frac{k_s}{k_f} \left(\frac{L^2 \omega}{\kappa_s} \right)^{1/2} (Pr Re_L^2 C_f)^{-1/3} \quad (1.14)$$

Under the present conditions this quantity is of order 10^{-1} , so we may approximate 1.12 as simply $Q_f \approx .9Q_t$. Combining this result with 1.9 and 1.11 and simplifying, we obtain the final approximate result that

$$v_{eff}(\xi, y) \approx \frac{1}{\rho} \frac{\partial \mu}{\partial T} \frac{Q_t}{kb(L^2 \xi)^{1/3}} e^{-r_w y^2 / 9 \mu \kappa \xi} \quad (1.15)$$

This expression gives the effective vertical velocity introduced by the heating technique. It is in a convenient form for pointing out several features. First, it is noted that the fluid response depends linearly on the power input, Q_t . This is in agreement with experimental results as can be seen in figure 3.4 in which the disturbance amplitude measured far downstream of the heater is seen to be a very nearly linear function of the heater power. In this case, there would be additional multiplicative factors introduced by the integrated disturbance growth and the conversion to wall shear, but the linear dependence upon Q_t remains the same. This is very convenient to know, for it means that in order to increase the disturbance amplitude by say a factor of 2, one simply needs to increase the heater power by a factor of 2.

Another feature of equation 1.15 is that the vertical dependence of the effective velocity is now made explicit. For instance, evaluating 1.15 at the wall and integrating over ξ , we obtain

$$v_{eff}|_{y=0} \approx \frac{1}{\rho} \frac{\partial \mu}{\partial T} \frac{Q_t}{kbL} \quad (1.16)$$

This is easily shown to be identical to the expression for the effective wall velocity as found in Nosenchuck. Nosenchuck then argued that the streamwise extent of the heater should be wide compared to the local boundary layer thickness to allow for penetration of the heat flux to the critical layer. The nature of this penetration is seen directly

in 1.15. At the wall, the effective velocity perturbation decreases as $\xi^{-1/3}$ due to the increasing thermal boundary layer thickness and the correspondingly decreasing wall temperature gradient. Away from the wall, however, the exponential term dominates, and the effective velocity now increases exponentially with ξ as

$$v_{eff}(\xi, y) \sim e^{-y^3/\xi} \quad (1.17)$$

As we move further away from the wall, this spatial localization of the effective velocity increases greatly, as the streamwise dependence on ξ is multiplied by a cubic term in y . Therefore in the vicinity of the critical layer, the effective velocity increases exponentially with streamwise distance along the heater reaching a maximum at the heater trailing edge. Though our similarity analysis extends only to the heater trailing edge, it is easily seen that a further increase in ξ will result in a decrease in the effective velocity as there is no longer any heat input at the wall, and all existing thermal gradients will decay rapidly.

In the present study, the streamwise extent of the heater is 7.6 mm and the displacement thickness δ^* is typically on the order of 1 mm. The heater is therefore rather large compared to the boundary layer thickness. Also of interest is the wavelength of the disturbance which in the present experiments is on the order of 25 mm. The heater is seen to cover a significant fraction of this distance as well. Due to the exponential dependence on ξ as seen in equation 1.17, however, the spatial localization of the forcing is maintained, and the resulting resolution of the forced oscillations in both time and space is excellent.

As the discussion thus far has dealt with a two-dimensional heater, it is necessary to make a few comments with regard to the spanwise segmentation of the present heater array. As will be shown in the next chapter, the present heater array consists of 32 elements which are separated by a heater-to-heater gap of 0.76 mm. This gap is small, but it is not negligible when compared to the displacement thickness or critical layer

height both of which are of the order of 1 mm. The input disturbance cannot then be considered as a single eigenmode, but must rather be represented as a sum of normal modes over all possible spanwise wavenumbers with the frequency of oscillation set by the heater forcing. Thus we have as our input disturbance

$$\vec{u}(\vec{x}, t) = \sum_{\beta} \vec{u}(\beta) e^{i(\alpha(\beta)x \pm \beta z - \omega t)} \quad (1.18)$$

Though no measurements were made of this transient disturbance development, it is believed that the preferential amplification of the boundary layer for disturbances of low spanwise wavenumber will insure that the dominant mode amplified will indeed be the lowest mode. This preferential amplification is seen in figure 5.11 which is taken from the calculations of Mack (1984). Thus the high wavenumber contributions to the sum in equation 1.18 will be strongly damped, and the resulting disturbance waveform observed far downstream will be very close to a single normal mode.

1.4 On Comparisons with Other Experiments

In the present study, the primary flow diagnostics are hot-film wall shear sensors, and the results are correspondingly presented in terms of normalized fluctuating wall shear, τ'_w/τ_w . In the current literature, however, hot-wire anemometry is the most commonly used method of measurement, and results are typically presented in terms of velocity fluctuations at the critical layer normalized by the free stream velocity, u_{max}/U_{∞} . It is therefore necessary to relate these two quantities in order that reasonable comparisons between experiments may be made.

Close to the wall, a reasonable approximation to the form of the disturbance eigenfunction, $u(y)$, can be taken as

$$u(y) \approx u_{max} \sin(\kappa_y y) \quad (1.19)$$

As the maximum in the disturbance eigenfunction occurs very nearly at the critical layer y_{cr} , we can evaluate the vertical wavenumber κ_y in terms of y_{cr} as

$$\kappa_y = \frac{\pi}{2y_{cr}} \quad (1.20)$$

Assuming that this expression for the vertical wavenumber holds at the wall, we can evaluate the fluctuating wall shear as

$$\tau_w' = \mu \frac{\partial u}{\partial y} \Big|_{y=0} = \frac{\pi \mu u_{maz}}{2y_{cr}} \quad (1.21)$$

Normalizing τ_w' by the mean wall shear $\bar{\tau}_w$ and u_{maz} by the freestream velocity U_∞ ,

$$\frac{\tau_w'}{\bar{\tau}_w} = \frac{\pi \mu U_\infty}{2 \bar{\tau}_w y_{cr}} \frac{u_{maz}}{U_\infty} \quad (1.22)$$

Using the Blasius value for the mean wall shear,

$$\bar{\tau}_w = 0.332 \rho U_\infty^2 Re_x^{-1/2} \quad (1.23)$$

we obtain

$$\frac{\tau_w' / \bar{\tau}_w}{u_{maz} / U_\infty} = \frac{\pi \nu Re_x^{1/2}}{0.664 U_\infty y_{cr}} \quad (1.24)$$

Using the approximation that $y_{cr} \approx \delta^*$, and that $Re_{\delta^*} = 1.721 Re_x^{1/2}$, we obtain

$$\frac{\tau_w' / \bar{\tau}_w}{u_{maz} / U_\infty} \approx 2.75 \quad (1.25)$$

This is, of course, only a rough estimate, but it provides us with an approximate figure for comparing the magnitudes of wall-shear fluctuations with velocity fluctuations.

This approximate relation can be verified experimentally by simultaneously measuring these two quantities. The full details of the experimental apparatus will be discussed in the next chapter. For the present, though, it is necessary only to note the result. A cylindrical hot-film velocity probe was positioned at the maximum in the eigenfunction profile. In this case, that corresponds to a distance of 0.3 mm above the plate surface.

The velocity probe was positioned directly above a hot-film wall-shear probe that was flush mounted on the plate surface. A two-dimensional Tollmien Schlichting wave was then generated. Figure 1.2 shows the simultaneously recorded time traces. The maximum amplitude of the fluctuating velocity u_{max}/U_{∞} is seen to be approximately two percent, while the peak amplitude of the fluctuating wall-shear signal $\tau_w'/\bar{\tau}_w$ is approximately five percent. Thus, the experimentally measured ratio of 2.5 compares quite well with the predicted value of 2.75.

CHAPTER 2

EXPERIMENTAL FACILITY AND INSTRUMENTATION

2.1 GALCIT High Speed Water Tunnel

All of the experiments in the present study were conducted in the GALCIT (Graduate Aeronautical Laboratories, California Institute of Technology) High Speed Water Tunnel (HSWT). A complete description of the HSWT can be found in Ward (1976). As shown in figure 2.1, the HSWT is a closed-circuit facility. The test section was of circular cross section with an internal diameter of 35.6 cm and an overall streamwise length of 1.05 m. The test section is preceded on the upstream end by a 20:1 contraction section that is three meters long, and it is followed on the downstream side by a 6:1 diffuser section that is six meters in length. A stainless steel honeycomb and a 40-mesh screen are positioned at the beginning of the contraction section. Throughout the present experiments, the tunnel pressure, which is adjustable over the range 0.2 to 6 bar, was maintained near atmospheric pressure.

A 35 cm wide lucite flat plate was mounted in the test section, completely spanning the test section diameter. Throughout the experiments, the freestream velocity was maintained at approximately 120 cm/s resulting in a Reynolds number of 1.4×10^6 based upon the total plate length. The flow quality was generally found to be quite acceptable. Using a cylindrical hot-film probe, the r.m.s. turbulence intensity was measured to be 0.05 percent in the freestream.

2.2 Flat Plate Model

Figure 2.2 shows the flat plate test model used throughout the experiments. The plate was machined from lucite and consisted of a central flat section preceded by a 6:1 elliptical leading edge and followed by an adjustable trailing edge flap. The overall

plate dimensions (including leading and trailing edges) were 104 cm in length by 35 cm in width by 2.0 cm in thickness. The leading edge was chosen to be a 6:1 ellipse, as that geometry provided a reasonable laminar flow profile over a large portion of the plate center body while maintaining a small but finite region of adverse pressure gradient close to the leading edge. The phased heater array was deliberately located in this region so as to take advantage of the enhanced growth rates offered by the adverse gradient and thus augment the effectiveness of the heating technique.

The central flat section of the plate contained most of the forcing and flow diagnostic equipment. The phased heater array was flush mounted 7.0 cm from the leading edge. At a typical freestream velocity of 120 cm/s, the heater Reynolds number Re_{δ^*} was approximately 520. Thus with respect to the neutral stability curve, the heater was located very close to the minimum critical Reynolds number. When not in operation, the heater presents a very minimal disturbance to the flow. For example, non-dimensionalizing by the wall friction velocity $u^* = (\tau_w/\rho)^{1/2}$, the protrusion of the heater into the flow is seen to be a mere $y^+ = u^*t/\nu \approx 1.5$, where t is the thickness of the etched copper layer.

Hot-film wall-shear sensors were located at various streamwise and spanwise locations far downstream of the heater array, and provided the primary flow diagnostics. The plate also contained a static pressure tap which together with a pitot probe located upstream of the contraction section was used to obtain the freestream flow conditions and thereby calibrate the wall-shear sensors. For several experiments, a dye injector was also located on the plate for flow visualization.

All electrical leads and tubing were connected to the bottom, non-active side of the plate and exited through sealed plugs on the bottom wall of the test section. As the substantial number of connections together with the finite thickness of the plate itself provided a non-negligible flow blockage, the trailing edge flap was used to position the leading edge stagnation point such as to minimize the overall plate pressure gradient.

2.3 Flow Documentation

As mentioned previously, the plate contained a 6:1 elliptical leading edge. This created a region of adverse pressure gradient immediately downstream of the leading edge. From static pressure measurements on earlier models with similar leading edge configurations, it was found that the flow returned to an essentially undisturbed Blasius flow very quickly. In order to measure the mean velocity profile, a cylindrical hot-film velocity probe (TSI model 1260-10W) was used. The supporting structure for the probe was designed with a streamlined cross-section so as to provide adequate rigidity while minimizing flow induced vibration due to vortex shedding. The boundary layer thickness $\delta_{99\%}$ at the probe location was approximately 3.0 mm, and the probe traversed this distance in 32 increments of 0.1 mm per step. The probe was positioned by a stepper motor which was interfaced to the central microprocessor. A physical stop was provided which limited the probe to a minimum vertical position of 0.125 mm ($y^+ \approx 3.5$).

The measured boundary layer profile is shown in figure 2.3 with the computed Blasius curve included for comparison. As can be seen, the measured profile at this x-location is very nearly Blasius. Thus, the local behavior of the forced disturbances as measured at locations far from the leading edge should agree quite well with the predictions of the linear theory for a Blasius mean profile. Measurements of integrated quantities such as the disturbance amplitude, however, will depend upon the exact pressure gradient history encountered by the disturbance as it travels downstream from the heater to the point of measurement. For this reason, most results in this study will emphasize measurements of local quantities as opposed to integrated quantities. In this way, comparisons with other experiments or numerical calculations may be made.

2.4 Phased Heater Array

Figure 2.4(a) shows a planform view of the heater array. The array consists of 32 individual heater elements, each with one lead running to the side of the array for connection to the driving electronics and the other lead connected to a common ground. An enlarged view of a single heater is shown in figure 2.4(b). The overall dimensions of each individual element are 1.0 cm in width by 0.76 cm in the streamwise direction. Within each heater the line width is 0.254 mm, and the total line length is approximately 16.3 cm. This results in a nominal heater resistance of 0.50 ohms. The low heater resistance was chosen in order to enable large power input into the flow at relatively low voltages. The advantages of this scheme are twofold. First, the low heater voltages prevented the occurrence of electrolysis and the associated bubble formation. Secondly, and of equal importance, was the fact that very large amounts of power could be easily supplied at such low voltages by simply using two 12 volt batteries as the sole power supply. Separating each heater is a gap of 0.76 mm making the entire array 34.9 cm in width which spans the GALCIT High Speed Water Tunnel cross section of 35.5 cm. The array is fabricated from a commercially available material consisting of a 0.035 mm layer of copper deposited on an epoxy-glass laminated substrate and was etched using conventional photolithographic techniques. All design and construction was carried out at GALCIT.

2.5 Instrumentation

To control and supply power to the heater array, a good deal of supporting instrumentation was necessary. Figure 2.5 shows a schematic diagram of the control apparatus. The entire array was under control of an 8-bit microprocessor (Intel 8085) which established the frequency, relative phase, and amplitude of the 32 heating elements. A

programmable frequency generator was employed to generate sinusoidal signals covering the range from 0 to 50 Hz. The frequency was programmable in 256 discrete steps with an incremental step size of less than 0.2 Hz. As the heat flux into the flow Q_f is proportional to the square of the applied heater voltage (or current), the available forcing frequency range seen by the flow was actually twice that of the input or from 0 to 100 Hz. This completely spanned the range of unstable Tollmein-Schlichting frequencies at the flow conditions encountered throughout the experiments.

To produce three-dimensionality in the form of arbitrary spanwise phase distributions, a bank of 32 individually programmable, unity-gain phase shift stages was provided. These circuits were again under control of the central microprocessor and were programmable in 16 discrete increments. The minimum heater to heater phase shift was 5.6° and the maximum possible was 90° . The phase control was primarily used for the forcing of single oblique eigenmodes, and it was thus found convenient to tie the output of phase shift $n - 1$ to the input of phase shift n resulting in a linear phase shift across the span of the array.

For example, with each heater programmed for an 11.2° phase shift, a total phase shift of 360° would result over the 35 cm span of the array. Thus, a disturbance would be generated with a spanwise wavelength λ_s of 35 cm. Under the present experimental conditions, a typical streamwise wavelength λ_x would be on the order of 2 cm, and the resulting disturbance would therefore be an oblique eigenmode with wavenumber vector \vec{k} oriented at an angle $\theta = \tan^{-1}(\lambda_x/\lambda_s) \approx 4^\circ$ from the freestream flow direction.

In addition to the phase-shift capability, the array control electronics also allowed for amplitude modulation of each individual heater voltage. As with the phase shift circuitry, these were again under control of the microprocessor with outputs ranging from 0.5 volts to 8.0 volts in increments of 0.5 volts. These were used to create arbitrary amplitude distributions across the span of the array. As an example, the array could be

programmed for a sinusoidal spanwise amplitude distribution producing a disturbance waveform very similar to that produced by the vibrating ribbon technique.

Finally, before reaching the heater array, each signal went through a power amplification stage. There were 32 such circuits, one to supply power to each heating element. The circuit as seen in figure 2.6 was a simple push-pull emitter follower with Darlington power transistors to supply the necessary current amplification ($h_{FE} \approx 4000$). The push-pull configuration was used in order to allow for symmetrical forcing about ground and thus minimize the unnecessary D.C. heating. During the experiments, the output voltage was limited to 5.0 volts resulting in a maximum r.m.s. power output of approximately 25 watts/heater or over 700 watts for the entire array.

In order to obtain a physical picture of the types of disturbances which can be produced with the array, three separate cases are considered. Figure 2.7 shows a three-dimensional perspective view of the resulting Tollmien-Schlichting wave surfaces for each case. In each plot the axes are time, spanwise distance, and the normalized wall-shear amplitude, τ'_w/τ_w . To obtain these plots, the programmability of the array was employed. Rather than move the sensor relative to a fixed disturbance as is customarily done, the disturbance in this case was moved relative to a fixed sensor located on the plate centerline at a Reynold's number of 1240. In this way, the measurement apparatus is greatly simplified.

Figure 2.7(a) shows a two-dimensional Tollmien-Schlichting wave surface. In this case, each heater was forced with the same phase and amplitude across the span of the array. The two-dimensionality of the waves has been measured at several spanwise locations and is seen to be excellent. Using this type of two-dimensional forcing, wave amplitudes of 15 percent have been obtained. Figure 2.7(b) shows a single oblique eigenmode. The array in this case was programmed for a constant phase shift from heater to heater while maintaining a constant amplitude across the span of the array.

Though such oblique waves have been known to be unstable for over 50 years, they have never been systematically studied due to lack of an appropriate experimental technique.

Finally, figure 2.7(c) shows a wave packet; i.e. a disturbance localized in both space and time. The forcing in this case consisted of 4 cycles of a sinewave forced by a single heater element with all other elements turned off. The single active element was then swept across the array creating the spanwise disturbance seen in the figure. These plots are shown at the present time merely to give a qualitative picture of the possible types of disturbances that can be generated by the phased heater array. A much more detailed look at the experimentally generated wave patterns will be given in chapters 3 (two-dimensional waves) and 5 (oblique waves).

2.6 Flow Diagnostics and Data Acquisition

This section describes the flow diagnostic equipment used throughout the experiments. The primary means of measurement was provided by hot-film wall-shear sensors (TSI model 1240) that were flush mounted on the plate at various streamwise and spanwise locations. The sensor dimensions were 1.0 mm by 0.125 mm (aspect ratio 8:1) and were oriented such as to measure the streamwise component of the wall shear. These probes were used to obtain measurements of growth rates, phase velocities, spanwise phase relationships, etc. Measurements could be made at streamwise locations separated by as little as 3 mm, a distance corresponding to roughly $0.1 \lambda_x$, where λ_x is a typical streamwise Tollmien-Schlichting wavelength. In this way, measurements of instantaneous growth rates could be obtained even when the disturbances exhibited non-linear or non-stationary behavior. It is important to emphasize the non-stationary aspect at this point. If the wave growth were purely stationary, then a single probe could be traversed in the streamwise direction to obtain the disturbance growth rates. As soon as the problem

becomes non-stationary, however, measurements at different locations must necessarily be made simultaneously in order to capture the relevant phenomena.

Both the wall-shear sensors and the velocity sensor were operated in the constant temperature mode. The probe resistance (and therefore temperature) was maintained at a constant value by the bridge circuit of figure 2.8. The circuit is a simple voltage feedback loop with an emitter-follower (2N2270) to supply the necessary current. A 200 ohm potentiometer was used to adjust the probe overheat, $\Delta T/T = (R_{hot} - R_{cold})/R_{cold}$, which was typically on the order of 6 percent. The bridge circuit also contained a current limiting resistor which maintained the probe current at a safe operating level. The output from the top of the bridge was then buffered and low-pass filtered at 200 Hz to prevent aliasing in data acquisition. Power was supplied by two 12-volt marine batteries which eliminated the 60 Hz line noise usually introduced by rectifying power supplies. The noise level was thus kept to a quite acceptable low level of 5 millivolts peak-to peak.

CHAPTER 3

TWO DIMENSIONAL WAVE EXCITATION

3.1 Introduction

In this chapter, we will examine the results from several experiments on the forcing of two-dimensional Tollmien-Schlichting waves. Emphasis will be put on understanding the nature of the non-linear effects arising as the disturbance amplitude is increased. As indicated earlier, numerous studies have been undertaken to explore the non-linear aspects of boundary layer transition. The question thus arises as to why the need for another study on this same subject. The reason for the present investigation is two-fold.

First, the present state of knowledge on the subject is far from complete. As a specific example, consider the following question: at what disturbance amplitude does the linear theory cease to hold? That is, we seek the threshold amplitude beyond which either non-linearity or three-dimensionality or both must be taken into account in order to explain the disturbance behavior. This specific point provides a convenient benchmark by which experiments and theory may be compared, as the threshold amplitude is a frequently quoted figure in the current literature. Furthermore, from a practical standpoint, the threshold amplitude is significant in that it is a measure of the point at which large dynamical growth rates take over from the much smaller viscous growth rates predicted by the linear theory. It therefore gives an approximate measure of the point at which transition to turbulence may be said to occur.

A significant number of investigators report a threshold amplitude on the order of one percent; i.e. at $u'_{max}/U_{\infty} \approx 1\%$, a strong departure from the linear theory is observed. This figure is reported in the experiments of Saric, Kozlov, and Levchenko (1984) and Kachanov and Levchenko (1984), the theoretical analyses of Craik (1971) and Herbert (1983), and the numerical simulations of Spalart (1984).

In contrast to these investigations are several experimental studies which report no apparent threshold amplitude for disturbances of 5 to 6 percent. Strykowski and Sreenivasan (1985), for example, using a purely two dimensional mechanical suction and blowing device report wave amplitudes of close to 6 percent. The agreement between experimental data and the linear eigenfunction are good. Williams, Fasel, and Hama (1984) likewise report waves of 5.5 percent, again with excellent agreement to the linear theory. The forcing mechanism in this case was a small wire located at the critical layer oscillated by a mechanical lever-cam arrangement.

Clearly there is some disagreement on this issue. It is to be noted that in all of the studies reporting a threshold amplitude near one percent, the departure from linearity is coincident with the onset of three-dimensionality. This is evident in the flow visualization of Saric et al. and Kachanov et al. as well as the numerical particle tracing of Spalart. On the other hand, the experiments of Williams et al. clearly document the fact that the observed waves in their experiment are two-dimensional. This discrepancy is most likely due to the different types of forcing mechanisms used in these experiments. Both the investigations of Strykowski and Sreenivasan and of Williams et al. employ forcing mechanisms which were very two-dimensional in nature. The vibrating ribbon, however, necessarily has a spanwise variation in forcing amplitude of 100 percent from the maximum in the center to zero at the fixed ends. This causes no problem, of course, if the resulting disturbances are observed very close to the ribbon and thus far from the region of influence of the clamped ends. This was precisely the case in the experiments of Schubauer and Scramstad. If the disturbances are observed far from the ribbon, however, the influence of the finite ends cannot be ignored.

A second and equally important reason for looking at the non-linear development of two-dimensional waves is that it provides a point of departure for the results of the next few chapters on oblique waves. As will be seen, oblique waves of sufficiently large ampli-

tude show interesting behavior arising from both the non-linear nature of the problem as well as the three dimensional geometry of the waves. Having first studied the non-linear effects in the two dimensional case, it will be much easier to recognize and identify the role of these two distinct mechanisms in the oblique wave development.

3.2 Experimental Conditions

In the present experiments, much care was taken to insure that the forced disturbances were as two-dimensional as possible. Two sources of three-dimensionality were inherent in the forcing mechanism employed in these experiments. As pointed out previously, the finite segmentation of the heater array introduces higher spanwise wavenumber components into the initial disturbance waveform. These are expected to be strongly damped in accordance with the linear theory, and the departure from two-dimensionality due to this effect should therefore be small far downstream of the heater.

A second source of three-dimensionality is the variation in the resistance of the heaters themselves. Though great care was taken in the array fabrication, the individual heater resistances can vary by as much as ten percent from the mean. The heat flux delivered to the flow, however, can be made constant across the span of the array by adjusting the forcing voltage via a variable resistor (one per heater) in the control electronics. In this way, the power delivered to the flow could be maintained at a very nearly constant level across the 35 cm span of the tunnel.

3.3 Experimental Results for Single Mode Excitation

3.3.1 Disturbance Growth Rates

Figure 3.1 shows a typical wall shear time series of the naturally occurring T. S.

waves. In the upper plot, the fluctuating wall-shear τ' is plotted normalized by the mean wall shear $\bar{\tau}$ and has an rms value of less than one percent. Plotted below is the amplitude spectrum. Nearly all of the energy is found between 20 and 30 hz (non-dimensional frequency, $F = 0.78$ to 1.18). Virtually no energy is seen outside of this narrow frequency band. With the forcing turned on, the observed wall shear is as shown in figure 3.2. In this particular case the forcing frequency is 22 hz ($F = 0.86$), and the power supplied to the 32 element heater array is approximately 460 watts (18 watts per square cm). The forced waves are seen to be quite regular, with the variation in amplitude due almost entirely to the naturally occurring background waves.

In order to verify the two-dimensionality of the forced oscillations, two hot-film wall-shear sensors at spanwise locations $z = \pm 2.0\text{cm}$ were used. As seen in figure 3.3, the waves are indeed quite two-dimensional. There is a slight difference in disturbance amplitude at the two probes, but it is generally less than a few percent of the mean value. One possible reason for this difference would be a variation in the amplitude of the naturally occurring waves at each sensor location. Also, a slight mismatch in the trimming resistors in the control electronics could account for this difference.

In order to assess the extent of non-linearity in the disturbance development, it is instructive to look at the wave amplitude as a function of the power input to the heater array. Figure 3.4 shows the normalized disturbance amplitude at two sensor locations as a function of the input power. It is noted that the disturbance amplitude is a very nearly linear function of the heat input up to forcing levels of about 300 W. Beyond this forcing level, a departure from linearity is observed. The linearity of the fluid response is in agreement with equation 1.16 provided that the quantity $\partial\mu/\partial T$ remains constant. At the higher forcing levels, however, the temperature difference ΔT as obtained from equation 1.11 becomes quite large ($\Delta T = 20^\circ\text{C}$ for $Q_t = 500\text{W}$), and the change in $\partial\mu/\partial T$ over this temperature range can no longer be neglected. For a temperature

increase of 20°C , $\partial\mu/\partial T$ decreases by nearly fifty percent. This change in the fluid properties with temperature therefore accounts for the change in the magnitude of the velocity perturbation introduced into the fluid.

It is important at this point to differentiate between the mechanism by which the disturbances are introduced into the fluid and the mechanism of viscous instability which governs their subsequent development. As has just been seen, the velocity perturbation is introduced into the fluid by a non-linear mechanism. Even at the largest forcing amplitudes, however, the velocity perturbation which is initially introduced into the fluid is very small. The downstream development of the disturbance, then, is governed by the linear theory. It is the effect of weak non-linearity in this region which is of primary interest.

In the absence of non-linear effects, the disturbance amplitude measured at a given location, x , would be given by

$$A(x) = A(x_0) \int_{x_0}^x e^{-\alpha_i x} dx \quad (3.1)$$

where α_i is the spatial growth rate given by the linear theory, and $A(x_0)$ is a reference amplitude measured at x_0 . Thus, if we examine the amplitudes at two different sensors located at streamwise positions x_0 and x_1 , the amplitude ratio $A(x_1)/A(x_0)$ should be a constant value. Any departure from this value would indicate a departure from the linear theory. Figure 3.5 shows a plot of such an amplitude ratio evaluated at Reynolds numbers $Re_{\delta^*} = 1178$ and 1240 . The amplitude ratio A_1/A_0 is plotted as a function of the amplitude A_1 evaluated at $Re_{\delta^*} = 1240$. As can be seen in figure 3.5, the amplitude ratio is quite constant up to disturbance amplitudes of nearly 12 percent. Substantial variation is seen at the lower disturbance amplitudes since the forced oscillations are on the order of those naturally occurring, and the resulting growth rate depends on the exact phase relation between these two. As the amplitude of the forced oscillations increases, however, the contribution of the background waves becomes less important.

It is thus concluded that the growth rates as predicted by the linear theory remain valid for disturbance amplitudes of at least 12 percent.

3.3.2 Generation of Higher Harmonics

Returning to the spectrum of figure 3.2, one further feature is observed. A small but clearly evident peak exists at 44 Hz ($F=1.72$), exactly twice the forcing frequency. This peak was not apparent in the unforced case (figure 3.1). The nature of this component of the disturbance can be seen by narrowly band-pass filtering the time series data around the two dominant spectral peaks at 22 Hz and 44 Hz and superposing these two filtered time series traces as shown in figure 3.6. The smaller amplitude 44 Hz trace can now be identified as a non-linearly generated first harmonic of the fundamental T. S. wave at 22 Hz. This is evident by noting that the two time series traces are perfectly phase-locked. If the wave at 44 Hz were a linear wave itself, the wavespeed would be different from that of the 22 Hz wave and phase-locking would not occur.

Further insight into the nature of the first harmonic is obtained by examining its amplitude. This is shown in figure 3.7 as a function of the forcing level. The amplitude is generally seen to increase with the forcing level, but the important point to notice here is that the amplitude is increasing with the Reynolds number as well. According to the linear theory, a disturbance at this frequency and Reynolds number should be strongly damped, i.e. decreasing with increasing Reynolds number. This is clearly shown in the neutral curve of figure 1.1.

The behavior of the first harmonic wave is therefore not described by the linear theory. This is not surprising since this is in fact a non-linear phenomenon. It arises due to the self-interaction of the fundamental wave with itself. The amplitude of the first harmonic is directly related to that of the fundamental as seen in figure 3.8. The

dependence is quadratic as expected. Higher harmonics are also generated but are only seen in this investigation when the fundamental amplitude becomes very large. Figure 3.9 shows one example of the appearance of higher harmonics. The fundamental, first harmonic, and second harmonic are clearly visible, and a very small peak at the third harmonic is also seen.

3.3.3 Frequency Dependence

In the previous section, it was shown that the integrated amplification A_1/A_0 was independent of the disturbance amplitude at least up to amplitudes of twelve percent. This is a local result in that we have examined the wave behavior over a very narrow range of Reynolds numbers. Furthermore, we have so far studied disturbances at only one frequency.

In order to obtain a more global view, the frequency dependence of the forced oscillations was studied by performing the following experiment. The phased heater array was initially programmed to force two-dimensional waves of small amplitude. The frequency of the forced disturbance was then increased in increments of 2 Hz, completely covering the range of unstable frequencies seen by a sensor at $Re_\delta \approx 1240$. In this way, the integrated disturbance amplitude is obtained as a function of frequency. The output voltage of the heater array was then increased, and the experiment was repeated. Figure 3.10 shows the result of this experiment, where the normalized fluctuating wall-shear $\tau'/\bar{\tau}$ is plotted as a function of both the frequency and the forcing level. At each forcing level, a Gaussian least squares fit is shown as well. There is no a priori reason for choosing a Gaussian other than that it seems to fit the data reasonably well.

The important point to be noticed from figure 3.10 is that the region of unstable frequencies as seen by the wall-shear sensor is virtually independent of the amplitude of

the forced waves. At each forcing level, the most amplified frequency is 25 hz, and the range of unstable frequencies extends from 12 hz to 40 hz. Since figure 3.10 gives the integrated amplification from the heater to the sensor, it seems reasonable to conclude that the growth rates, α_i , are independent of the disturbance amplitude for a very wide range of frequencies and Reynolds numbers. Thus if one were to inquire as to the shape of the neutral curve for finite amplitude waves, the present results suggest that it is essentially unchanged up to disturbance amplitudes of 12 percent.

3.3.4 Summary of Observed Non-linear Effects

The effect of weak non-linearity in boundary layer transition is thus seen to be relatively benign. The growth rates were seen to follow the linear theory up to perturbation amplitudes of nearly twelve percent. This was seen by analyzing both the local growth rates as well as the integrated amplification over a wide range of frequencies and Reynolds numbers. The only deviation from the linear theory arose in the form of a non-linearly generated first harmonic wave phase-locked to the fundamental, whose amplitude depended quadratically upon that of the fundamental. Higher harmonics were also observed, but as their amplitudes scale with higher powers of the fundamental amplitude, they are only seen at very large forcing levels. The appearance of these non-linear harmonics will certainly alter the wave behavior somewhat, but as will be seen in the next few chapters, the onset of three-dimensionality has a much more profound impact on the transition process.

CHAPTER 4

GEOMETRICAL NATURE OF OBLIQUE INSTABILITY WAVES

4.1 Introduction

Before we begin to examine the behavior of oblique instability waves in a boundary layer flow, it is necessary that we first define the type of disturbance that is to be studied. Throughout the next several chapters, the disturbance velocity field will be assumed to be of the form

$$\bar{u}(\vec{x}, t) = \bar{u}(y) e^{i(\alpha x + \beta z - \omega t)} \quad (4.1)$$

The velocity components $\bar{u}(\vec{x}, t)$ are complex; all experimental data will of course correspond to only the real part, however. The angular frequency $\omega = 2\pi f$ will be taken as a purely real quantity corresponding to the physically realistic spatial growth problem. Most analytical studies, on the other hand, consider the temporal growth problem where ω is complex. The streamwise wavenumber α is complex with α_i giving the rate of growth ($\alpha_i < 0$) or decay ($\alpha_i > 0$) of the disturbance amplitude. The real part $\alpha_r = 2\pi/\lambda_x$ is the streamwise wavenumber of the disturbance. The spanwise wavenumber β is in general also complex, but under the present experimental conditions it can be shown to be purely real; i.e. $\beta = \beta_r = 2\pi/\lambda_z$. This will be shown in the next section.

Equation 4.1 is the most commonly used form for oblique waves, but other notations are frequently also found in the literature. For example, equation 4.1 could equally well be written as

$$\bar{u}(\vec{x}, t) = \bar{u}(y) e^{i\vec{\kappa} \cdot (\vec{x} - \vec{c}t)} \quad (4.2)$$

where $\vec{\kappa} = \alpha\hat{i} + \beta\hat{k}$ is the total wavenumber vector, and $\vec{c} = c_x\hat{i} + c_z\hat{k}$ is the phase velocity vector of the disturbance. Written in this form, one must ask the question: In what direction does the disturbance travel? That is, we seek the components of the phase velocity vector, c_x and c_z . For that matter, one would also like to know the magnitude and direction of the group velocity vector $C_g = \partial\omega/\partial\kappa$, as well, as this quantity gives

the direction in which energy is propagated. These quantities are of little importance in theoretical studies, since the disturbances are usually assumed infinitely periodic in the x and z directions and are thus prevented from "propagating" out of the computational domain. In an experiment, however, the direction of propagation must be known in order to correctly position sensors for measurement. Determination of the group and phase velocities is thus an important practical matter, and it will be shown in section 4.3 that an understanding of these quantities adds a good deal of physical insight into the nature of oblique instability waves as well.

Finally, section 4.4 will take a look at the vorticity field of a single oblique mode. It will be shown that whereas the vorticity field of a two-dimensional disturbance is purely one-dimensional (i.e. a scalar, ω_x), the vorticity field for an oblique normal mode is fully three-dimensional with ω_x , ω_y , and ω_z each being a non-vanishing quantity. The implications of this revealed three-dimensional structure on the stability of the disturbances will be discussed as well.

4.2 Spatial Growth Rates

In the words of Mack (1984), "It is also possible to conceive of wavemakers that excite single oblique normal modes in boundary layers that are independent of z . Such normal modes will have an initial β_i which matches that of the wavemaker, and, because the wave can grow only in x , the initial β_i must be zero." The phased heater array used in the present study is precisely such a wavemaker.

It is easy to see why β_i must be identically zero by performing the following thought experiment. Imagine a heater array such as the one described in Chapter 2 but with a span extending to infinity in both directions. Assume now that the elements of such an array are excited with the same amplitude and phased so as to produce a single

oblique normal mode. A sensor located some distance downstream of this heater would measure the same r.m.s. disturbance amplitude everywhere across the span as there is no preferred spanwise direction and no definable spanwise origin for the disturbance. The present heater array completely spans the test facility very nearly approximating such a hypothetical array. Thus for the present experimental conditions, we may justifiably assume that $\beta_i = 0$.

4.3 On the Direction of Propagation

The group and phase velocities are important quantities in any wave-like phenomenon. An examination of the current literature shows that there is some confusion regarding these quantities. For example, Craik (1971) considers a disturbance of the form 4.1, with ω complex and α real, and assumes that

$$\bar{c} = \frac{\omega_r}{\alpha} \hat{i} \quad (4.3)$$

That is, the phase velocity is assumed to be parallel to the freestream direction. Mack (1984), on the other hand, considers the very same disturbance and assumes that

$$\bar{c} = \frac{\omega_r}{|\bar{\kappa}|^2} \bar{\kappa} \quad (4.4)$$

i.e. the phase velocity is assumed to be parallel to the wavenumber vector $\bar{\kappa}$. Similarly, Kachanov and Levchenko (1983) take \bar{c} parallel to $\bar{\kappa}$ in the analysis of their experimental results.

In an attempt to resolve this issue, the following experiment was conducted. A single oblique wave of finite span was generated by the phased heater array. The span of the disturbance was 35 cm, i.e. the full span of the test section. To study the effects of finite span as well as the direction of propagation, the disturbance was then "shifted" across the span of the array. The finite disturbance was "shifted" by turning heater elements

off in a sequential manner beginning at one end of the array and proceeding across the array to the other end. As far as the sensor on the plate centerline is concerned, this procedure is the same as shifting the disturbance through the tunnel side wall, since disturbances near the side walls have no effect on the flow at the plate centerline. In this way a single probe located on the plate centerline was used to record the entire spanwise extent of the disturbance. This procedure was then repeated, "shifting" the disturbance in the opposite direction; i.e. "through" the other tunnel side wall.

The spanwise amplitude distribution obtained in this manner gives results which are comparable to those that would be obtained by moving a sensor relative to a fixed disturbance of essentially twice the span. Thus, we have effectively doubled the width of the tunnel. The advantages of this scheme are twofold. First, the edge contamination region near the tunnel side walls is completely avoided. Similarly, the finite end effects of the disturbance itself are kept to a minimum by making the disturbance width as large as possible. This leaves a substantial segment in the center of the disturbance which is not affected by the finite ends. It is the disturbance in this region that is of most interest, as it corresponds very nearly to a single oblique normal mode.

Figure 4.1a shows the amplitude distribution obtained in this manner. Several observations can be made from this plot. The disturbance is seen to extend approximately 20 cm to either side of the plate centerline with a relatively constant amplitude section from -10 cm to 10 cm. A significant amount of scatter exists in the amplitude and is accounted for by the naturally occurring background oscillations. If we assume a spreading angle of 16 degrees for the finite end effects as suggested by Mack (1984), then spanwise locations where $|z| > 20$ should be free of the influence of the forced oscillations. The scatter in this region of the flow thus represents the scatter in the naturally occurring oscillations.

The angle of the oblique wave in this experiment was approximately 15 degrees.

The streamwise distance that the disturbance has travelled from its origin at the heater to the point of measurement is over 30 cm. From figure 4.1a, it is seen that the energy of the disturbance has travelled very nearly in the stream direction, spreading perhaps a few centimeters further to values of positive z than to values of negative z . This slight asymmetry will be discussed later, but for the present, it seems reasonable to conclude that the group velocity of this disturbance, or the velocity with which energy is propagated, is very nearly oriented in the freestream direction. It is certainly not parallel to the wavenumber vector $\vec{\kappa}$, as propagation in that direction would have displaced the energy distribution nearly 9 cm from the plate centerline. Furthermore, since the center region of the disturbance consists of a single normal mode, the phase velocity in this region must be equal to the group velocity. This must be the case, since there can be no possible dispersion for a single mode. We therefore conclude that the phase velocity is oriented in the freestream direction as well.

An interesting comparison with the preceding experiment is provided by the point source calculations of Mack (1984). Figure 4.1b shows a plot of the normalized disturbance amplitude of a single oblique normal mode of finite span. The origin of the disturbance in this case was physically oblique; i.e. one end of the disturbance was located at a higher Reynolds number than the other end. As in figure 4.1a, a region in the center exists which is free of the effects of the finite ends. In this case, however, the amplitude is not constant but rather increases monotonically across the span. This is due to the physically oblique nature of the disturbance origin. The disturbance has simply travelled different distances and therefore undergone a different integrated amplification at each spanwise location. It is also to be noted that the disturbance amplitude falls off rather more smoothly on the left side of each figure and is seen to fluctuate somewhat more on the right side. Surprisingly, this is a very repeatable feature of the experimental data.

A plausible explanation for this feature is offered by noting that a sum over oblique normal modes as in equation 1.18 would have to be constructed in these regions in order to properly represent the finite nature of the disturbance span. As will be seen later in this chapter, the vortex filaments of such a disturbance are oriented very nearly perpendicular to the wavenumber vector and thus lay at an oblique angle to the flow direction. By analogy with the starting vortex of a finite span airfoil, these vortices must also connect to some form of starting vortex system at the heater. The more downstream end of the oblique vortices must therefore turn through a greater angle in order to connect with a starting vortex system than the more upstream end. Thus the sum of equation 1.18 would consist of different combinations of spanwise modes for the two finite ends of the disturbance. The more downstream end would require more energy at higher spanwise wavenumbers in order to turn the corner and could thereby account for the observed short wavelength oscillation on the right side of both figure 4.1(a) and 4.1(b) as well as the slight difference in lateral spreading of the disturbance. It must be remembered, however, that this argument is strictly valid only for an inviscid fluid, whereas the present flow is viscous. It is nevertheless believed to provide a useful explanation for the finite span vorticity field in the present experiments.

4.3.1 *The Nature of Viscous Instability*

In the previous section, the direction of propagation of an oblique wave was studied. It is also of interest to examine the magnitude of this propagation velocity. In particular, it is interesting to see how this quantity varies with the angle of the wave. Consider the following experiment. The phased heater array was initially programmed to force two-dimensional waves. Two hot-film wall-shear sensors separated by 3 mm in the streamwise direction were used to obtain the phase velocity. The time of flight of individual wave

crests was measured and averaged over 50 cycles of the disturbance. Dividing the sensor separation distance by the time of flight gives the phase speed of the disturbance. The heater array was then programmed to output oblique waves at increasingly greater angles to the flow direction, and each time the phase speed was measured.

The result of this experiment is shown in figure 4.2. The normalized phase velocity c_x/U_∞ is plotted as a function of the spanwise wavenumber β . Surprisingly, the phase velocity is seen to remain constant. That is, the propagation velocity c_x is independent of the angle of the disturbance. In order to see why this should be the case, let us examine the physical mechanism governing viscous instability.

The physical mechanism governing these instability waves can be viewed as follows. Sinusoidal oscillations in the velocity profile cause vorticity to be generated at the wall. This vorticity then diffuses away from the wall and is convected by the mean velocity field in the streamwise direction. Convection by the disturbance velocity field can be neglected, as it is zero in the mean. When the vorticity from the wall has diffused to the critical layer, it adds to the vorticity which is already present in the disturbance. If the frequency of oscillation and critical layer height $y_{cr}(Re)$ are such that the vorticity shed from the wall arrives at y_{cr} in phase with that already present, then the vorticity of the disturbance increases. If, on the other hand, the shed vorticity is out of phase upon reaching the critical layer, then the vorticity of the disturbance decreases. Viewed in this way, it is seen that viscous instability waves are in a sense not waves at all. It was seen earlier that these waves do not propagate in the direction normal to their phase fronts as normal waves do, but rather travel in the freestream flow direction. It is perhaps not even correct to speak of wave "propagation" at all, *since the problem is really one of diffusion and convection of periodic vorticity rather than propagation of a wave.*

When the vortices are oblique, the situation is basically the same. Now, oscillations of the velocity profile cause both x-vorticity and z-vorticity to be created at the wall.

This vorticity again diffuses away from the wall and is convected by the mean flow in the x -direction. Therefore, it is not really suprising that the phase speed of the waves is seen to be independent of the wave angle as in figure 4.2, for the same mechanisms of diffusion and convection of vorticity govern the disturbance development regardless of the orientation of the lines of constant phase.

4.4 A Look at the Vorticity Field

A great deal of insight can be gained by looking at the vorticity field of the perturbation. For example, in the two dimensional case, the vorticity field is seen to consist of a streamwise periodic array of vortices with the only non-vanishing vorticity component being that in the spanwise direction,

$$\omega_z = \frac{\partial v}{\partial x} - \frac{\partial u}{\partial y} = (i\alpha v - \frac{\partial u}{\partial y})e^{i(\alpha x - \omega t)} \quad (4.5)$$

In the case of oblique disturbances of the form 4.1, it is natural to expect that the vorticity field would be very similar to that of a two-dimensional disturbance, with the only difference being that the vortex filaments are rotated by an angle $\theta = \tan^{-1}(\beta/\alpha)$. Thus, we would expect two vorticity components, ω_x and ω_z . This picture of the vorticity field of an oblique wave is, however, not entirely correct. To see why this physical picture is incorrect, it is necessary to look at the mathematical form of the disturbance velocity field as given in equation 4.1. Taking the curl of 4.1, the vorticity field is obtained as

$$\omega_x = \frac{\partial w}{\partial y} - \frac{\partial v}{\partial z} = \left(\frac{\partial w}{\partial y} - i\beta v\right)e^{i(\alpha x + \beta z - \omega t)} \quad (4.6a)$$

$$\omega_y = \frac{\partial u}{\partial z} - \frac{\partial w}{\partial x} = (i\beta u - i\alpha w)e^{i(\alpha x + \beta z - \omega t)} \quad (4.6b)$$

$$\omega_z = \frac{\partial v}{\partial x} - \frac{\partial u}{\partial y} = (i\alpha v - \frac{\partial u}{\partial y})e^{i(\alpha x + \beta z - \omega t)} \quad (4.6c)$$

The difference between the two-dimensional and three-dimensional vorticity fields now becomes apparent. In our previous picture of the three-dimensional vorticity field,

the vortex filaments were straight and everywhere perpendicular to the wavenumber vector $\vec{\kappa} = \alpha \hat{i} + \beta \hat{k}$. More importantly though, this picture of the vorticity field contained no vertical vorticity ω_y , whereas from 4.6b, it is seen that ω_y is *not* identically zero.

To prove that ω_y is in fact a non-vanishing quantity for an oblique wave, consider the linearized equations of motion:

$$\nabla \cdot \vec{u} = 0 \quad (4.7a)$$

$$\left(\frac{\partial}{\partial t} + U \frac{\partial}{\partial x}\right) \vec{u} + v \frac{\partial U}{\partial y} \hat{i} = -\nabla p + \frac{1}{Re} \nabla^2 \vec{u} \quad (4.7b)$$

Substituting the assumed form of the disturbance from 4.1 and correspondingly taking the pressure perturbation as

$$p(\vec{x}, t) = p(y) e^{i(\alpha x + \beta z - \omega t)} \quad (4.8)$$

we obtain

$$i\alpha u + \frac{\partial v}{\partial y} + i\beta w = 0 \quad (4.9a)$$

$$\left[-i\omega + i\alpha U - \frac{1}{Re} \left(\frac{\partial^2}{\partial y^2} - \alpha^2 - \beta^2\right)\right] u + v \frac{\partial U}{\partial y} = -i\alpha p \quad (4.9b)$$

$$\left[-i\omega + i\alpha U - \frac{1}{Re} \left(\frac{\partial^2}{\partial y^2} - \alpha^2 - \beta^2\right)\right] v = -\frac{\partial p}{\partial y} \quad (4.9c)$$

$$\left[-i\omega + i\alpha U - \frac{1}{Re} \left(\frac{\partial^2}{\partial y^2} - \alpha^2 - \beta^2\right)\right] w = -i\beta p \quad (4.9d)$$

Multiplying 4.9(b) by $i\beta$, 4.9(d) by $i\alpha$, and subtracting, we obtain

$$\left[i\omega - i\alpha U + \frac{1}{Re} \left(\frac{\partial^2}{\partial y^2} - \alpha^2 - \beta^2\right)\right] (i\beta u - i\alpha w) = i\beta v \frac{\partial U}{\partial y} \quad (4.10)$$

The fact that ω_y is not identically zero then follows by contradiction, for assuming that $\omega_y \equiv 0$ implies that the left hand side of 4.10 vanishes. Since $\partial U / \partial y \neq 0$ and $\beta \neq 0$, this implies that v must be zero everywhere. This problem was considered in 1933 by Squire, where he showed that such a disturbance (an oblique wave with $v(y) \equiv 0$) is

always stable. Therefore if $\omega_y \equiv 0$, no instability exists for oblique waves at all. Since it is known from experiments that this is not the case, it must be concluded that ω_y is not identically zero and is in fact given by the expression 4.6(b).

4.5 Three-Dimensional Stability Theory Revisited

Having determined that the vorticity field of an oblique wave is indeed fully three-dimensional, let us now examine the possible impact that this might have on the stability of the disturbance. It is convenient to begin with the full (non-linearized) equations of motion expressed in terms of the vorticity:

$$\frac{\partial \bar{\omega}}{\partial t} + (\bar{u} \cdot \nabla) \bar{\omega} = (\bar{\omega} \cdot \nabla) \bar{u} + \nu \nabla^2 \bar{\omega} \quad (4.11)$$

Here $\bar{\omega}$ represents the total vorticity of the flow, i.e. the mean vorticity plus that of the disturbance. The velocity vector \bar{u} is likewise that of the mean flow plus that of the disturbance. Each term in 4.11 is easily interpreted as follows: $\partial \bar{\omega} / \partial t$ is the rate of change of vorticity, $(\bar{u} \cdot \nabla) \bar{\omega}$ is the convection of vorticity by the velocity field, $(\bar{\omega} \cdot \nabla) \bar{u}$ corresponds to the rotation and stretching of vorticity by the strain field, and the final term is of course the dissipation due to viscosity. It is the first term on the right-hand side that is of particular interest here, as it was identically zero in the two-dimensional case. For oblique waves, however, it provides an alternate means of vorticity production that was not available for two-dimensional disturbances.

It is easily shown that equation 4.11 can be rewritten as

$$\frac{\partial \bar{\omega}}{\partial t} + (\bar{u} \cdot \nabla) \bar{\omega} = \bar{\omega} \cdot \epsilon + \nu \nabla^2 \bar{\omega} \quad (4.12)$$

where the strain rate tensor ϵ is given by

$$\epsilon_{ij} = \frac{1}{2} \left(\frac{\partial u_i}{\partial x_j} + \frac{\partial u_j}{\partial x_i} \right) \quad (4.13)$$

If we now linearize 4.12, making the usual parallel flow assumption, $U = U(y)$, we obtain

$$\frac{\partial \bar{\omega}'}{\partial t} + U \frac{\partial \bar{\omega}'}{\partial x} - v' \frac{\partial^2 U}{\partial y^2} = \bar{\omega}' \cdot \bar{\epsilon} + \bar{\Omega} \cdot \epsilon' + \nu \nabla^2 \bar{\omega}' \quad (4.14)$$

where $\epsilon = \bar{\epsilon} + \epsilon'$ and $\bar{\omega} = \bar{\Omega} + \bar{\omega}'$. The vorticity production term, $(\bar{\omega} \cdot \nabla) \bar{u} = \bar{\omega} \cdot \epsilon$, has thus been separated into the two linear components shown on the right-hand side of 4.14. The first of these corresponds to the distortion of the disturbance vorticity field by the mean strain field, and the second term gives the distortion of the mean vorticity field by the disturbance strain field.

In order to explore the nature of these vorticity production terms, let us look at the simplest possible problem, that of Couette flow. Couette flow is known to be stable to small two-dimensional disturbances, but the three-dimensional problem remains relatively unexplored. The mean flow profile is linear, and the third term on the left-hand side of 4.14 therefore vanishes. If we confine our attention for the moment to only the first of the vorticity production terms and take $\bar{\Omega} \cdot \epsilon'$ to be zero, we arrive at the equation (dropping primes on the disturbance quantities):

$$\frac{D\bar{\omega}}{Dt} = \bar{\omega} \cdot \bar{\epsilon} + \nu \nabla^2 \bar{\omega} \quad (4.15)$$

where $D/Dt = (\partial/\partial t + U\partial/\partial x)$. The mean strain rate tensor $\bar{\epsilon}$ is given by

$$\bar{\epsilon} = \begin{pmatrix} 0 & \frac{\partial U}{\partial y} & 0 \\ \frac{\partial U}{\partial y} & 0 & 0 \\ 0 & 0 & 0 \end{pmatrix} \quad (4.16)$$

The eigenvalues of $\bar{\epsilon}$ are found to be $\partial U/\partial y$, $-\partial U/\partial y$, and 0. The corresponding principal directions are $\hat{e}_1 = (\hat{e}_x + \hat{e}_y)$, $\hat{e}_2 = (\hat{e}_x - \hat{e}_y)$, and $\hat{e}_3 = \hat{e}_z$. Rewriting equation 4.15 in terms of the vorticity components in the principal coordinate system, ω_1 , ω_2 , and ω_3 , we obtain the following set of uncoupled equations for the vorticity components:

$$\frac{D\omega_1}{Dt} = \frac{\partial U}{\partial y}\omega_1 + \nu \nabla^2 \omega_1 \quad (4.17a)$$

$$\frac{D\omega_2}{Dt} = -\frac{\partial U}{\partial y}\omega_2 + \nu \nabla^2 \omega_2 \quad (4.17b)$$

$$\frac{D\omega_3}{Dt} = \nu \nabla^2 \omega_3 \quad (4.17c)$$

From equations 4.17, the nature of the additional vorticity production terms now becomes more apparent. In equation 4.17(a), for example, it can be seen that following the fluid, there are two competing mechanisms operating. The first term on the right hand side corresponds to the stretching of the disturbance vorticity by the mean strain field, $\partial U/\partial y$, and the second term is the usual viscous dissipation term. For sufficiently low Reynolds numbers or for $\partial U/\partial y \rightarrow 0$, the viscous term will dominate and the magnitude of ω_1 will decay with time. On the other hand, for large Reynolds numbers or large shear rates, the stretching term will dominate, and the magnitude of ω_1 will increase exponentially. The exponential growth would, of course, not continue without bound, but rather would give rise to turbulent flow. The qualitative behavior of equations 4.17 is therefore in agreement with the experimentally observed behavior, for it is known that turbulent Couette flow does indeed exist. In addition, in the purely two-dimensional case, only equation 4.17(c) remains, and all disturbances are damped following the fluid. This is also in agreement with the known result that Couette flow is stable to two-dimensional disturbances.

The exact conditions for instability would of course require that the full linearized equation 4.14 be solved with all terms included. The present brief examination of the disturbance vorticity suggests, however, that instability may indeed occur for three-dimensional disturbances even when two-dimensional disturbances are stable. This is due to the additional vorticity production terms inherent in the three-dimensional problem. In the next chapter, experimental evidence will be presented that indicates that under

identical forcing conditions, oblique waves can in fact be much more unstable than any two-dimensional disturbance.

Chapter 5

THREE-DIMENSIONAL, OBLIQUE WAVE EXCITATION

5.1 Introduction and Preliminary Observations

In this chapter, we will examine the results of several experiments designed to explore the behavior of single oblique instability waves. Such disturbances have been discussed in the literature for over 50 years and are currently employed as an integral part of several proposed resonance mechanisms as seen in Chapter 1. Virtually no experiments exist, however, which either confirm or deny the predictions of the linear theory with regard to the behavior of oblique waves. It is the goal of this section to shed some light on this subject. In particular, attention will be focused on the following issue. It is the general consensus in the literature that oblique waves are less dangerous, that is, less unstable than their two-dimensional counterparts. The simple analysis of the preceding chapter, however, suggests that the additional vorticity production terms inherent in the three-dimensional problem may indeed result in much higher growth rates than those given by the linear theory. If this were to be the case, then oblique waves should be seen to be more unstable than two-dimensional waves. As will be shown, certain regimes of the parameter space exist for which this is indeed the case.

In order to get a feel for the behavior of oblique waves, consider the following experiment. The phased heater array was programmed to force oblique waves at increasing angles to the mean flow direction. The amplitude of the forcing was held constant throughout as were the freestream flow conditions. At each angle, the frequency was varied, completely spanning the range of unstable frequencies. Figure 5.1 shows a plot of the normalized disturbance amplitude as recorded at $Re_{\delta^*} = 1240$. In order to obtain the points in figure 5.1, the spectra were locally band-pass filtered at the forcing frequency. The response shown is thus the integrated flow response at the forcing frequency alone.

A flow response at frequencies other than the forcing frequency (the subharmonic, for example) would not appear in figure 5.1. As will be seen, the flow response does indeed contain energy at frequencies other than the forcing frequency. This behavior constitutes a major departure from the anticipated results and is discussed in great detail in the next few sections.

Several observations can be made from figure 5.1. First, it is noted that the integrated flow response at the forcing frequency decreases with increasing wave angle. Thus it appears that oblique waves become less unstable as the wave angle is increased. That this is not a correct statement will be shown in detail in the section 5.3.2. The reason is, as mentioned above, that we have not taken into account the possible flow response at frequencies other than the forcing frequency. For the present, then, it can only be stated that the flow response at the forcing frequency decreases with increasing wave angle.

A second observation from figure 5.1 is that approximately the same frequency range is seen to be unstable regardless of the wave angle. This suggests that the region of unstable frequency-Reynolds number space (i.e. the neutral surface) is essentially the same for all wave angles. It should be recalled that in Chapter 4, it was seen that the phase speed of oblique disturbances was independent of the wave angle as well. These two observations are consistent with the physical description of viscous instability as a balance between convection and diffusion of vorticity. Thus it is seen that the behavior of oblique waves is quite similar to that of two-dimensional waves. The only difference seen thus far has been that the integrated amplification at the forcing frequency decreases with increasing wave angle. This is not the only difference, however. As will be seen, certain regions of the parameter space exist in which a different mechanism dominates the oblique wave development. This results in a radical departure from the type of behavior seen in two-dimensional waves, and is therefore the subject of the remainder of the chapter.

5.2 The Onset of Non-stationary Behavior

The remainder of this chapter breaks down into two separate parts. The first half is concerned with a simple observation from the experimental data. That observation is the following: certain regions of the parameter space exist for which oblique waves exhibit inherently non-stationary behavior. By non-stationary we mean that the spectral content of the signal changes with time. This behavior occurs under well controlled forcing conditions to be described and is an entirely repeatable feature of the disturbance. Section 5.2.1 will explore the time series behavior in an attempt to characterize the nature of this non-stationary behavior. Section 5.2.2 will then discuss the subject of spectral analysis for non-stationary signals, as the usual methods such as the Fast Fourier Transform are no longer applicable. The Wigner distribution will be introduced as a means of non-stationary frequency analysis and will be used to support the direct observations made from the time series data. Finally, the implication of this simple observation on several of the currently proposed resonance mechanisms will be discussed.

The second half of the chapter will present a simple mechanism which is again suggested by direct observation of the time series data. This mechanism is simply that the non-stationary behavior is due to the intermittent roll-up or pairing of adjacent vortices of the disturbance. This mechanism has long been known to play a major role in the development of unbounded shear flows such as the mixing layer and wake. The results from a thorough experimental examination of the parameter space will then be discussed and will be shown to be consistent with this simple model. Finally, the entire picture of the role of oblique waves in boundary layer transition will be summarized by relating the geometrical properties revealed in chapter 4 to the experimental observations and proposed mechanism of the present chapter.

5.2.1 Time Series Behavior

Figure 5.2 shows a typical wall-shear time signal. The heater array in this case was programmed to force a single oblique wave at approximately 15 degrees. The forcing frequency was 11 Hz, producing a 22 Hz disturbance due to the squaring of the forcing voltage. The signal shown in figure 5.2 was recorded by a hot-film wall-shear probe at a Reynolds number of approximately 1300. Several observations can be made from this plot.

The first point to be noticed is that the signal is quite non-stationary. This is easily seen by noting that in the interval $0.3 < t < 0.6$ a single dominant frequency exists in the wall-shear fluctuations. This is the frequency corresponding to the forcing, i.e. 22 hz. The r.m.s. fluctuation is typically on the order of five percent of the mean wall-shear. Moving to the interval $0.6 < t < 0.8$ a curious behavior is observed. Adjacent peaks in the time trace corresponding to local maxima in the wall-shear fluctuations are seen to merge yielding a signal which now contains considerable energy at twice the fundamental period of oscillation. The result of this pairing is further demonstrated in the initial portion of the time trace, $0.0 < t < 0.3$, where very large magnitude fluctuations are observed with a primary period twice that of the fundamental period of oscillation. The fluctuations are seen to approach 50 percent of the mean wall-shear level and are much larger in the positive direction than in the negative. This asymmetry with respect to the sign of the fluctuations is a very consistent feature of the observed experimental data. These observations will be shown in section 5.2.4 to be consistent with a simple physical mechanism, that of vortex pairing.

5.2.2 Frequency Analysis of Non-stationary Signals

In analyzing the spectral content of a time signal such as that in figure 5.2, the usual methods such as the Fast Fourier Transform can no longer be used, as Fourier

analysis relies on the basic assumption that the time series is stationary. An alternative procedure would be to take the FFT of a short segment of the data with the assumption that the frequency content of the signal is nearly constant over that portion of the data. This method has a serious drawback, though. Taking a short segment of the data implies a multiplication in the time domain with a suitably chosen windowing function. In the frequency domain, this is then a convolution of the spectrum with the convolution of the windowing function. As the length of the window is decreased to provide a closer approximation to a stationary signal, the effect of the convolution in the frequency domain is to smear out the spectral content and thus resolution in frequency is lost.

An alternative method is provided by the use of the Wigner transform. For the present purposes, the Wigner transform will merely be defined and then used to corroborate some of the observations from the time series data. Appendix B will contain a more thorough description of the transform properties and the particular implementation used in this study. Additional detailed analyses of the Wigner transform are also to be found in the recent work of Imberger and Boashash (1985) and Claasen and Mecklenbrauker (1980).

The Wigner transform of a function $g(t)$ is given by

$$W(t, f) = \int_{-\infty}^{\infty} g\left(t + \frac{\tau}{2}\right) g^*\left(t - \frac{\tau}{2}\right) e^{-i2\pi f\tau} d\tau \quad (5.1)$$

where g^* is the complex conjugate of g . In practice some form of windowing function is also used, so $g(t)$ would be replaced by $g_1(t) = w(t)g(t)$, where $w(t)$ is the chosen windowing function. Figure 5.3 shows an example of the use of the Wigner transform on a typical data sample. The time series is shown on the left hand side of the figure for comparison. The standard FFT of the entire record is given at the bottom of the figure. From the full FFT, one can see that the signal contains most of its energy at the two dominant frequencies, 12.5 Hz and 25 Hz. All information regarding the phase, however, is lost. That is, we have no idea if these two frequency components

were present throughout the record or occurred in some non-stationary manner. The Wigner transform provides precisely this information. For this particular record, the Wigner transform was evaluated at intervals of 0.1 sec. The entire spectral content of the signal at each of these points in time is thus obtained. A Hanning window was chosen to minimize the effects of the finite record length of the signal. This is especially important near the ends of the record. The question regarding the phase is thus resolved by examination of the time-frequency plot of the Wigner transform. As can be seen in figure 5.3, the energy at the subharmonic is not present at all times. In fact, substantial periods are observed in which no subharmonic exists at all. These observations are of course equally well verified by direct examination of the time series data.

5.2.3 Comparison with Proposed Resonance Mechanisms

The observations of the preceding sections have a direct bearing on some of the current ideas in the literature regarding resonance mechanisms. As indicated in the introduction, a wide variety of resonance mechanisms between a two-dimensional wave and some form of three-dimensional wave have been proposed to explain the onset of three-dimensionality in boundary layer transition. They are summarized in table 1.1. Many of these mechanisms involve a subharmonic wave; i.e. a wave with frequency one half that of the fundamental wave. As has been indicated, the present data show the appearance in the spectrum of energy at the subharmonic of the forcing frequency. It is natural to ask whether this behavior can be explained by some form of resonance. From direct observation of the time series behavior as well as the combined time-frequency analysis afforded by the Wigner transform, it seems that this is not the case, since the temporal behavior of the subharmonic does not seem to correlate well with that of the fundamental. As is seen in figure 5.3, the subharmonic content of the signal increases and decays without regard to the magnitude of the fundamental which remains relatively

constant throughout.

On the other hand, it could be argued that what is observed in figure 5.3 is a non-stationary resonance between the forced oblique wave and the randomly occurring background oscillations. That is, resonance only occurs when the naturally occurring oscillations attain a certain amplitude and thus is seen to be non-stationary. This argument implies that there should exist a strong correlation between the amplitude of the naturally occurring waves and the appearance of non-stationary behavior in the resulting time series data. That this is not the case will be seen in section 5.3.1 when the frequency dependence of the non-stationary behavior is examined. It will be shown that the non-stationary behavior increases with increasing frequency of the forced oscillations, and that there is little correlation between the amplitude of the background waves (which are limited to a band of relatively low frequencies) and the appearance of the non-stationary behavior (which is seen primarily at higher frequencies).

5.2.4 An Alternative Mechanism: Vortex Pairing

An alternative mechanism that can be offered as an explanation for the observed behavior is the simple phenomenon of vortex pairing. If one were to move at the speed of the disturbance, the streamlines of the flow would appear as shown in figure 5.4(a). This "cat's eye" streamline pattern shows clearly that the disturbance consists of a periodic array of co-rotating vortices. In general, the relatively slow growth rates of the instability waves implies that the strength of adjacent vortices will vary little over a few wavelengths. Thus, the induced velocity on any given vortex will be very nearly zero, as contributions from those vortices immediately preceding and those immediately following that vortex will tend to cancel. Any imbalance in the induced velocity field, however, will cause adjacent vortices to pair together forming one large vortex. This is shown schematically in figure 5.4(b). This type of vortex pairing is widely observed in

free shear flows such as the wake and mixing layer, but has never been clearly observed in the boundary layer.

In the following section, it will be shown that there exist conditions for which the induced velocity field due to neighboring vortices cannot be neglected in the disturbance development. The induced velocity field at any point \vec{x}_0 is given by the Biot-Savart relation

$$\vec{u}(\vec{x}_0, t) = -\frac{1}{4\pi} \int_V \frac{(\vec{x} - \vec{x}_0) \times \vec{\omega}}{|\vec{x} - \vec{x}_0|^3} dV \quad (5.2)$$

From this expression, it can be seen that the induced velocity field increases linearly with an increase in the amplitude of the disturbance (i.e. an increase in $|\vec{\omega}|$). Thus, any imbalance in the induced velocity field will be magnified by an increase in the disturbance amplitude. In addition, it can be seen that the induced velocity field increases with a decrease in the vortex-to-vortex spacing. Therefore, any conditions which cause a decrease in the vortex spacing will further increase the tendency for vortices to pair.

Several experiments can be performed which lend support for this proposed mechanism of vortex roll-up. Specifically, the frequency dependence, wave angle dependence, and amplitude dependence of the forced instability waves will be examined and will be shown to be consistent with this mechanism. Furthermore, the behavior of the eigenfunction will be studied to gain insight into the vertical nature of the flow during the periods of non-stationary oscillation. Finally, the mechanism of vortex pairing will be discussed in light of the geometrical structure of the vortex filaments which was revealed in chapter 4.

5.3 Results for Oblique Wave Excitation

5.3.1 Frequency Dependence

In order to examine the frequency dependence of the instability waves, the following

experiment was conducted. The phased heater array was initially programmed to force purely two-dimensional waves. The forcing amplitude was kept constant throughout the experiment as were the freestream flow conditions. Figure 5.5 shows the resulting wall-shear time series as a function of the frequency of the forcing. This is a visual cut through the stability surface at a single Reynolds number. As expected, the oscillations are highly damped at the low and high ends of the forcing spectrum, and in the center there is a region in which the oscillations are most strongly amplified. Figure 5.6 shows the resulting amplitude spectra corresponding directly to the time series traces of figure 5.5. The spectra are seen to be quite clean; i.e. there is little observed response at frequencies other than the forcing frequency. This behavior is in qualitative agreement with the predictions of the linear theory.

Consider next the very same experiment, but with the phased heater array now programmed to generate a single oblique normal mode at an angle of approximately ten degrees. The time series traces and amplitude spectra are shown in figures 5.7 and 5.8 as a function of the forcing frequency. A very striking difference is noted. At the lower forcing frequencies, the observed flow response is quite similar to that observed previously in the two-dimensional case. At the higher end, however, the response is quite different. The time series behavior is seen to be non-stationary with large amplitude fluctuations. This type of behavior is observed to occur over a substantial range of frequencies. At frequencies greater than 40 hz, however, the observed flow response returns to the type of behavior seen in the two-dimensional case.

A look at the spectra of figure 5.8 provides further insight into this behavior. Appropriate caution must be taken, however, when discussing these spectra as the signals were observed to be non-stationary. At the lower frequencies, a very clean response is seen at the forcing frequency. The response in this frequency range is thus quite similar to that of the two-dimensional case. At the higher end, however, the flow response at

the forcing frequency decreases in accordance with the linear theory, but the level of activity throughout the rest of the spectrum has greatly increased. This corresponds to the observed non-stationarity observed in figure 5.7. Beyond a forcing frequency of approximately 40 hz, a return to the essentially undisturbed flow conditions is observed.

In the previous section, it was suggested that the observed non-stationary behavior could be explained in terms of a roll-up of adjacent vortices of the disturbance. The frequency behavior observed in figures 5.5-5.8 can now be discussed in terms of this mechanism. Specifically, we must ask why the non-stationary behavior is seen to occur primarily at the higher end of the unstable frequency range. From equation 5.2, it is seen that the induced velocity at any point in the boundary layer, \vec{x}_0 , due to neighboring vortices varies inversely with the square of the distance to the adjacent vortices. Since it is known that the phase speed c of the waves varies little from $c \approx .35U_\infty$, it can be seen that an increase in the frequency of the disturbance corresponds to a decrease in the disturbance wavelength. Thus, the effect of increasing the frequency is to decrease the separation distance between adjacent vortices. This then increases the induced velocity quadratically according to equation 5.2. A mismatch in the induced velocity from vortices immediately preceding and those immediately following a given vortex will therefore have a much greater effect upon the tendency for vortices to roll-up. This mismatch could be the result of random disturbances in the flow or perhaps even the difference in amplitude due to the spatial growth of the disturbance. The observed increase in the non-stationary nature of the oscillations with increasing frequency is thus consistent with the mechanism of vortex roll-up.

5.3.2 Wave Angle Dependence

A second parameter that can be explored is the angle $\theta = \tan^{-1}(\beta/\alpha)$ of an oblique wave. To study the effect of this parameter, consider the following experiment. The

forcing amplitude and freestream flow conditions were again held constant as in the previous experiment. The forcing frequency in this case, however, was fixed at 28 Hz and the angle θ of the disturbance was varied. Figures 5.9 and 5.10 show the resulting time series and spectra as a function of the wave angle. Two observations can be made from these figures. First, the response at the forcing frequency is seen to decrease with increasing wave angle. This is in agreement with the theorem of Squire (1933) which stated that the critical Reynolds number increased with increasing wave angle, and thus the integrated amplification as recorded in figures 5.9 and 5.10 decreases with increasing wave angle. This theorem is strictly valid only for temporally growing waves, however. A more direct explanation is afforded by the calculations of Mack in which it is shown that the growth rates for oblique waves generally decrease with increasing wave angle. This is shown in figure 5.11 in which the integrated amplification $\ln(A/A_0)$ is shown as a function of the wave angle ψ .

The second feature observed from figures 5.9 and 5.10 is that the occurrence of non-stationary behavior in the time series waveforms is seen to increase with increasing angle just as was the case with increasing frequency. This is not surprising when we consider the geometry of the situation as sketched in figure 5.12. It must first be recalled from section 4.3 that the phase speed vector was found to be parallel to the freestream flow direction and furthermore was seen to be independent of wave angle θ . Thus an increase in wave angle (at constant frequency) leaves $\lambda_x = c/f$ unchanged while λ_z decreases. Therefore as seen in figure 5.12, the separation distance, S , between adjacent vortices in the oblique wave decreases with increasing wave angle. The induced velocity as given by equation 5.2 therefore increases with increasing wave angle just as was the case with increasing frequency. This observed behavior is again consistent with our proposed mechanism of vortex roll-up.

5.3.3 Amplitude Dependence

Returning to the spectra of figure 5.8 (forcing frequency dependence) or figure 5.10 (wave angle dependence), an additional observation can be made. It is clearly seen that the occurrence of the non-stationary behavior is a much stronger function of the forcing frequency or wave angle than it is a function of the disturbance amplitude. This is seen by noting that at the most amplified frequency of approximately 24 Hz, the disturbance waveform is seen to be quite stationary. At higher forcing frequencies or wave angles, however, where the disturbance amplitude (at the forcing frequency) is smaller, a much greater non-stationarity is observed. This observation is again in agreement with the mechanism of vortex roll-up, for equation 5.2 shows that the induced velocity field depends linearly on the disturbance amplitude, whereas the dependence on frequency or wave angle (via vortex separation distance) is quadratic. Thus, the dependence on the disturbance amplitude should not be expected to be as great as the dependence on frequency or angle of the disturbance.

In order to directly examine the impact of disturbance amplitude on the occurrence of non-stationarity, the following experiment was conducted. The array was programmed to force a single oblique wave at an angle $\theta = 15^\circ$ and at a frequency of 25 Hz. The power input to the array was then continually increased. Figure 5.13 shows the time series behavior for this experiment. As can be seen, the response to the forcing is initially in accordance with the linear theory; i.e. a nice stationary response is observed. At a forcing level of approximately 200 W, though, significant portions of the time series are seen to exhibit the typical period doubling non-stationary behavior that we have been observing. As the power is increased further, this type of behavior becomes more and more prevalent. Though no scale is shown, the fluctuations in the final trace at times exceed 50 percent of the mean shear level. The dependence on amplitude shown here is not as strong as was previously seen in the frequency or wave angle dependence but it

is clearly a factor.

5.3.4 Eigenfunction Behavior

Further evidence for this proposed mechanism of vortex roll-up is obtained by studying the vertical nature of the disturbance; i.e. the eigenfunction profile. If vortex roll-up is occurring, then the eigenfunction should clearly show evidence of velocity fluctuations further from the plate surface than would normally occur. It should first be pointed out that the occurrence of vortex pairing or roll-up is almost certainly a three-dimensional phenomenon. Thus the velocity sensor will see all three components of the disturbance velocity field. Due to the high aspect ratio (8:1), though, the sensor is much more sensitive to velocity fluctuations perpendicular to its long axis, $u(y)$ and $v(y)$, than it is to those that are parallel, i.e. $w(y)$. Furthermore, fluctuations in the vertical direction are much smaller than those in the stream direction. The fluctuations seen by the probe, then, are essentially from the single component, $u(y)$.

In order to explore the nature of the eigenfunction, the following experiment was conducted. The phased heater array was initially programmed to force an oblique wave at 15 degrees. The frequency of the forcing was set at 22 Hz. As can be seen in figure 5.5, the response of oblique waves at such low frequencies is very clean. Thus, a very stationary oblique wave was generated. The hot-film velocity sensor then traversed the boundary layer in steps of 0.1 mm beginning at a vertical position 0.1 mm from the surface of the plate. Figure 5.14 shows the resulting flow response as a function of the vertical distance, y . The shape of the eigenfunction profile is quite typical. The maximum fluctuation level of $u_{max}/U_{\infty} \approx 2\%$ is seen to occur at $y = 0.3\text{mm}$ from the plate

The experiment was then repeated with one small change in the forcing conditions. The forcing amplitude was kept at the same level as before, and the array was again pro-

grammed to output oblique waves of 15 degrees. The only change was in the frequency of the forcing. The forcing frequency was set to 30 Hz. Reference to figure 5.5 shows that at this frequency, highly non-stationary behavior is observed. Measurement of the eigenfunction just as before results in the second profile plotted in figure 5.14. The magnitude of the fluctuations is seen to be much larger than in the previous case. This is not in accordance with the linear theory, as waves at 22 Hz should be more strongly amplified than those at 30 Hz. This is accounted for by the very large amplitude fluctuations typically observed when the disturbance becomes non-stationary.

The important point to be observed in figure 5.14 is that in the neighborhood of the wall, the entire character of the eigenfunction profile has changed. There is no longer a clearly observed maximum. Approximately the same fluctuation level is seen from $y = 0.1mm$ to $y = 0.6mm$. The large increase in the magnitude of the fluctuations occurs as a result of the stretching of vortex filaments which occurs in the pairing process. It is the displacement of the vortex centers, however, that accounts for the distorted profile shape as seen in figure 5.14.

It is to be noted that the maximum fluctuation level in the case of vortex pairing is found roughly twice as far from the wall ($y = 0.6mm$) as was found in the non-pairing case ($y = 0.3mm$). This is in agreement with the simplest intuitive notion of vortex pairing, where one vortex simply rolls over another and thus doubles the height. It is interesting to note also that this increase in activity away from the wall has been observed in other experiments. For example, in the classic paper of Klebanoff, Tidstrom, and Sargent (1962), the following statement is made: "The position of the maximum in the intensity distribution as given by the linear theory is at 0.2δ , but in the non-linear range the position of the maximum at a spanwise position corresponding to a peak moves away from the surface as breakdown is approached, and at breakdown has moved out to about 0.4δ ." This is clearly demonstrated in figure 5 of their paper. The flow in

that experiment was highly three-dimensional and non-linear having been disturbed by a physical obstruction (celophane tape) placed at regular intervals on the plate surface. It is believed that the driving mechanism in that experiment was precisely the same as in the present study, namely vortex pairing.

5.4 Summary of Three-Dimensional Effects

In the preceding two chapters, the nature of oblique instability waves has been explored analytically as well as experimentally. It has been shown that a great number of similarities exist between oblique waves and their two-dimensional counterparts. Some of these similarities are indeed quite suprising. For instance, a series of experiments involving forced oblique waves has shown that several of the properties are independent of the angle of an oblique wave. It was indicated that the direction of propagation is essentially the same for all types of disturbances, two-dimensional as well as oblique. Specifically, the direction of propagation is parallel to the freestream flow direction in all cases. In addition, the magnitude of the phase velocity was measured and was found to be independent of wave angle as well. Finally, it was found that the region of unstable frequency-Reynolds number space (i.e. the stability surface) was also seen to be independent of wave angle. Combining these observations with our knowledge of the dominant forces in a boundary layer, a mechanism describing the physical nature of viscous instability is offered. Namely, it has been suggested that viscous instability waves are caused by convection and diffusion of periodic vorticity generated at the wall. This explains why several of the observed disturbance properties are independent of the wave angle, as the mechanisms of diffusion and convection occur without regard to the orientation of the lines of constant phase.

In addition, it has been shown that several differences exist which set oblique waves apart from two-dimensional waves. In Chapter 4, the vorticity fields of these two types of

disturbances was examined, and it was found that a very important fundamental difference exists. In the two-dimensional case, the vorticity field was purely one-dimensional (i.e. a scalar, ω_z). In the three-dimensional case, however, the vorticity field is fully three-dimensional with each component ω_x , ω_y , and ω_z being a non-vanishing quantity. It was then shown that the existence of a three-dimensional vorticity field gives rise to an additional source of vorticity production that was unavailable in the two-dimensional case. It was further suggested that this additional source of vorticity production could cause instability to oblique disturbances even when two-dimensional disturbances were completely stable. The example used to illustrate this possibility was the as yet unresolved stability problem of Couette flow.

Finally, it was shown that certain regions of the parameter space exist for which oblique waves are indeed observed to be more unstable than any two-dimensional wave. This behavior is believed to originate from the additional vorticity production mechanism outlined above, and is seen to manifest itself in a roll-up of adjacent vortices of the disturbance waveform. It was further shown that the occurrence of this vortex pairing behavior was seen to increase with increasing frequency of oscillation, increasing oblique wave angle, and increasing amplitude. All of these factors occur in a manner consistent with the usual Biot-Savart law for the induced velocity field.

CHAPTER 6

CONCLUSIONS

An experimental study of the weakly non-linear as well as the three-dimensional nature of boundary layer transition has been conducted using a new technique. The active surface heating technique of Liepmann, Brown, and Nosenchuck was employed and in this study was extended to provide a means for controllably and repeatably introducing three-dimensional disturbances into a laminar boundary layer. A simple analysis of the heating technique was offered in an effort to clarify the mechanism by which the fluctuations in the wall heat flux are translated into localized velocity fluctuations in the vicinity of the critical layer. It was shown that the effective velocity perturbation introduced by the heating technique increases exponentially with the streamwise distance along the heater reaching its maximum value at the heater trailing edge. In this way, the spatial resolution of the disturbance is maintained even when heaters of large streamwise extent are used.

The details of the present experimental configuration have been described. The particular heater geometry used in this study consisted of a 32-element heater array spanning the test facility at a single streamwise location. Each element of the array is independently programmable in both amplitude and relative phase making possible a wide range of three-dimensional disturbances. The design and construction of the heater array are detailed along with a description of the control and power electronics necessary to drive the array.

The effect of weak non-linearity on boundary layer transition was then examined by an experimental study of two-dimensional instability waves of increasing amplitude. It has been shown that the effect of weak non-linearity is relatively benign. The growth rates were seen to follow the linear theory up to perturbation amplitudes of nearly twelve percent. This was seen by analyzing the local growth rates as well as the integrated

amplification over a wide range of frequencies. The only deviation from the linear theory arose in the form of a non-linearly generated first harmonic wave phase-locked to the fundamental, whose amplitude depended quadratically upon that of the fundamental. Higher harmonics were also observed, and their amplitudes correspondingly scaled with higher powers of the fundamental amplitude. It was concluded that even though these non-linearly generated harmonics do indeed alter the wave behavior to some extent, they are by themselves not sufficient to explain the transition from small linear oscillations to the large amplitude, broad-band, three-dimensional oscillations characteristic of a fully turbulent boundary layer.

Furthermore, the relation of the present study to some of the ideas prevalent in the current literature was discussed. It was shown that the results of the present study are not consistent with those experimental and theoretical investigations which report a rather low ($u/U_\infty \approx 1\%$) threshold amplitude for the spontaneous onset of three-dimensionality and the consequent departure from the predictions of the linear theory. Rather, it is believed that with sufficient care, very large amplitude two-dimensional disturbances can be generated with little observed departure from the relatively slow growth rates as predicted by the linear theory.

The effect of three-dimensionality on boundary layer transition was then investigated through an analytical and experimental study of single oblique instability waves. Single oblique waves were chosen (as opposed to oblique wave pairs or some other more elaborate combination of waves) since they are normal modes of the boundary layer. They are thus the fundamental three-dimensional structure in a transitional boundary layer. They have the additional advantage of having a relatively simple analytic description which is amenable to some elementary analysis.

It has been shown that a great number of similarities exist between oblique waves and their two-dimensional counterparts. Some of these similarities are indeed quite surprising.

For instance, a series of experiments involving forced oblique waves has shown that several of the properties are independent of the angle of an oblique wave. It was shown that the direction of propagation is essentially the same for all types of disturbances, two-dimensional as well as oblique. Specifically, the direction of propagation is parallel to the freestream flow direction in all cases. In addition, the magnitude of the phase velocity was measured and was found to be independent of wave angle as well. Finally, it was found that the region of unstable frequency-Reynolds number space (i.e. the stability surface) was also independent of wave angle.

Combining these observations with our knowledge of the dominant forces in a boundary layer, a mechanism describing the physical nature of viscous instability has been offered. Namely, it has been suggested that viscous instability waves are caused by diffusion and convection of periodic vorticity generated at the wall. The diffusion is directed normal to the wall, as the largest gradients occur in this direction, and the convection is in the freestream direction, since convection due to the disturbance velocity field is zero in the mean. This explains why several of the observed disturbance properties are independent of the wave angle, as the mechanisms of diffusion and convection occur without regard to the orientation of the lines of constant phase.

In addition, it has been shown that several differences exist which set oblique waves apart from two-dimensional waves. The vorticity fields of these two types of disturbances was examined, and it was found that a very important fundamental difference exists. In the two-dimensional case, the vorticity field was purely one-dimensional (i.e. a scalar, ω_z). In the three-dimensional case, however, the vorticity field is always fully three-dimensional with each component ω_x , ω_y , and ω_z being a non-vanishing quantity. It was then shown that the existence of a three-dimensional vorticity field gave rise to an additional source of vorticity production that was unavailable in the two-dimensional case. It was further suggested that this additional source of vorticity production could cause

instability to oblique disturbances even when two-dimensional disturbances were completely stable. The example used to illustrate this possibility was the as yet unresolved stability problem of Couette flow.

Experimentally, it was shown that certain conditions exist for which oblique waves are observed to be more unstable than any two-dimensional wave. This behavior is believed to originate from the additional vorticity production mechanism outlined above, and is seen to manifest itself in a roll-up of adjacent vortices of the disturbance waveform. It was further shown that the occurrence of this vortex pairing behavior was seen to increase with increasing frequency of oscillation, increasing oblique wave angle, and increasing wave amplitude. All of these factors occur in a manner consistent with the usual Biot-Savart law for the induced velocity field. In addition the eigenfunction was measured and was also found to be consistent with the mechanism of vortex pairing.

Finally, it is concluded that the behavior of oblique waves is much more complicated than was previously believed. The widely held belief that oblique waves are more stable and therefore less dangerous than two-dimensional waves is seen to be unfounded. Furthermore, it is concluded that oblique waves undoubtedly play a major role in the transition to turbulence. It is to be noted, however, that the results of this study deal only with the early stages of transition, and the resulting high frequency oscillations characteristic of fully developed turbulent flow were not seen. It is believed, though, that additional study on the further development of oblique waves will indeed reveal this behavior.

APPENDIX A

SIMILARITY ANALYSIS OF THE SURFACE HEATING TECHNIQUE

In order to obtain an approximate expression for the temperature profile above the heater element, consider the situation as sketched in figure A.1. The energy equation is given as:

$$\nabla \cdot \left[\rho \bar{u} \left(h + \frac{u^2}{2} \right) - \tau \cdot \bar{u} + \bar{q} \right] = 0 \quad (A.1)$$

If we now consider two-dimensional, parallel, low speed flow, we can make the following approximations:

$$\frac{u^2}{2} \ll h, \quad \tau \cdot \bar{u} \ll \bar{q}, \quad \bar{u} = (u, 0, 0) \quad (A.2)$$

Substituting into A.1, we obtain

$$\rho u \frac{\partial h}{\partial \xi} = k \frac{\partial^2 T}{\partial y^2} \quad (A.3)$$

The thermal boundary layer should be well within the linear region of the viscous boundary layer, and we can therefore take

$$u = \frac{\tau_w}{\mu} y \quad (A.4)$$

If it is further assumed that the streamwise extent of the heater is small compared to the distance from the leading edge, we may take τ_w to be constant over the heater.

Substituting A.4 into A.3 we obtain

$$\frac{\tau_w}{\mu} y \frac{\partial T}{\partial \xi} = \kappa \frac{\partial^2 T}{\partial y^2}, \quad \kappa = \frac{k}{\rho c_p} \quad (A.5)$$

If we now choose for the similarity variable $\eta = y/(\alpha \xi)^{1/3}$, and substitute into equation A.5, we obtain

$$\frac{\partial^2 T}{\partial \eta^2} + \frac{\alpha \tau_w}{3 \mu \kappa} \eta^2 \frac{\partial T}{\partial \eta} = 0 \quad (A.6)$$

Taking $\alpha = 3\mu\kappa/\tau_w$ and $\theta(\eta) = (T - T_w)/(T_\infty - T_w)$, we arrive at the simple ordinary differential equation

$$\frac{\partial^2 \theta}{\partial \eta^2} + \eta^2 \frac{\partial \theta}{\partial \eta} = 0 \quad , \quad \theta(0) = 0 \quad , \quad \theta(\infty) = 1 \quad (A.7)$$

This is easily integrated once to obtain

$$\frac{\partial \theta}{\partial \eta} = C e^{-\eta^3/3} \quad (A.8)$$

and once more, yielding

$$\theta(\eta) = C \int_0^\eta e^{-\eta^3/3} d\eta \quad (A.9)$$

The constant in A.9 is evaluated by making the substitutions, $\eta = (3t)^{1/3}$ and $d\eta = (3t)^{-2/3} dt$ and evaluating at $\eta = \infty$. Thus,

$$\theta(\infty) = C \cdot 3^{-2/3} \int_0^\infty t^{-2/3} e^{-t} dt = C \cdot 3^{-2/3} \Gamma\left(\frac{1}{3}\right) = 1 \quad (A.10)$$

The final result is obtained as

$$\theta(\eta) = 0.776 \int_0^\eta e^{-\eta^3/3} d\eta \quad (A.11)$$

From this expression the temperature profile and the heat transfer rates above the heater are easily obtained.

APPENDIX B

PRESENT IMPLEMENTATION OF THE WIGNER DISTRIBUTION

As indicated in Chapter 5, several excellent references are available which contain detailed discussions of the general properties of the Wigner distribution. The present discussion, however, will be concerned primarily with the particular implementation of the Wigner distribution as used in the analysis of the weakly non-stationary signals encountered throughout this investigation. The Wigner distribution will be shown to provide a viable alternative to spectral methods such as the Fourier transform and will therefore be frequently referred to as the Wigner transform. A brief introduction to the Wigner transform will be given followed by several instructive examples which point out several of the advantages as well as the disadvantages of this method.

The Wigner transform of a real function $x(t)$ is defined as follows:

$$W(t, f) = \int_{-\infty}^{\infty} z\left(t + \frac{\tau}{2}\right) z^*\left(t - \frac{\tau}{2}\right) e^{-i2\pi f\tau} d\tau \quad (B.1)$$

where $z(t)$ is an analytic signal whose real part is identical to the original function $x(t)$, and $z^*(t)$ is its complex conjugate. The analytic signal $z(t)$ is defined as

$$z(t) = x(t) + \frac{i}{\pi} \int_{-\infty}^{\infty} \frac{x(r)}{(t-r)} dr \quad (B.2)$$

It can be seen to be formed by a convolution of the original real time series $x(t)$ with a function $y(t)$ given by

$$y(t) = \delta(t) + \frac{i}{\pi t} \quad (B.3)$$

The Fourier transform of $y(t)$ is easily shown to be twice the unit step function, i.e. :

$$Y(f) = \begin{cases} 2 & f > 0 \\ 1 & f = 0 \\ 0 & f < 0 \end{cases} \quad (B.4)$$

Thus, the spectrum of $z(t)$ is equal to twice that of $x(t)$ for positive frequencies and is zero for all negative frequencies. In the present implementation, this forms an operational

definition of the analytic signal. The Fourier transform of $x(t)$ is calculated. It is then multiplied by a factor of two for all positive frequencies and set equal to zero for all negative frequencies. The DC component remains unchanged. Taking the inverse transform yields the analytic signal, $z(t)$. As a simple example, consider the signal, $x(t) = \cos(2\pi ft)$. Substituting into B.2 gives

$$z(t) = e^{i2\pi ft} = \cos(2\pi ft) + i\sin(2\pi ft) \quad (B.5)$$

In order to accommodate signals with finite record length, a windowing function is also used. In the examples to follow a Hanning window was chosen. It is defined as follows:

$$w(t) = \frac{1}{2} - \frac{1}{2}\cos\left(\frac{2\pi t}{T_w}\right) \quad (B.6)$$

where T_w is the width of the window. This has the usual effect of broadening the spectral peaks but is very useful in minimizing leakage effects inherent in a signal of finite duration. Thus the transform becomes

$$W(t, f) = \int_{-\infty}^{\infty} w(\tau) z(t + \frac{\tau}{2}) z^*(t - \frac{\tau}{2}) e^{-i2\pi f\tau} d\tau \quad (B.7)$$

In practice this transform is evaluated by first evaluating the kernel, $w(\tau)z(t + \tau/2)z^*(t - \tau/2)$. In order to evaluate this signal at times $t/2$, either interpolation or over-sampling is used. If over-sampling is employed, the original sampled signal $x(t)$ must be sampled at a rate of at least twice the Nyquist frequency. Standard fast Fourier transform methods are then used to evaluate B.7 with the time t specified as a parameter.

In order to further explore the properties of the Wigner transform, we will now take a look at several specific examples. In each example, the Wigner transform will be evaluated analytically according to B.1 and numerically by the above mentioned method using a sampled version of the input signal, $x(t)$.

EXAMPLE 1

Consider first the stationary signal,

$$x(t) = \sin(2\pi f_0 t) \quad (B.8)$$

The corresponding analytic signal is easily obtained as

$$z(t) = e^{i2\pi f_0 t} \quad (B.9)$$

Substituting into B.1,

$$W(t, f) = \int_{-\infty}^{\infty} e^{i2\pi f_0 (t+\tau/2)} e^{-i2\pi f_0 (t-\tau/2)} e^{-i2\pi f \tau} d\tau \quad (B.10)$$

Simplifying, this gives

$$W(t, f) = \int_{-\infty}^{\infty} e^{-i2\pi (f-f_0)\tau} d\tau = \delta(f - f_0) \quad (B.11)$$

Thus the Wigner transform consists of a single peak in the spectrum at $f = f_0$ and is independent of time. Figure B.1 shows a plot of $W(t, f)$ for a sampled version of $x(t)$ where $f_0 = 50\text{Hz}$. The time series $x(t)$ is shown on the left hand side of the plot, and the standard FFT is included on the bottom of the figure. $W(t, f)$ is evaluated at intervals of 0.1 sec using a Hanning window of width 0.4 sec. The window is rather wide, but temporal resolution is maintained due to the nature of the kernel used in the Wigner transform. A slight ringing is noted near the ends of the record because of the width of the window chosen, but otherwise the spectral content of the signal is seen to be relatively unchanged throughout the length of the signal.

EXAMPLE 2

Consider now a non-stationary signal of the form,

$$x(t) = \sin 2\pi f_1 t = \sin 2\pi [f_0 + (f_{\max} - f_0)t]t \quad (B.12)$$

The frequency, $f_1 = f_0 + (f_{\max} - f_0)t$, is a linearly increasing function of time. The corresponding analytic signal is

$$z(t) = e^{i2\pi f_1 t} \quad (B.13)$$

The Wigner transform is calculated exactly as in the previous example and is given as

$$W(t, f) = \delta(f - f_1(t)) \quad (B.14)$$

That is, the spectral content of the signal at any time t consists of a single peak at $f = f_1(t)$. This is seen graphically in figure B.2. The time series shown increases linearly in frequency from $f_0 = 30\text{Hz}$ to $f_{\max} = 70\text{Hz}$. As can be seen, the standard FFT shows only that the entire signal contains energy from $f = 30\text{Hz}$ to $f = 70\text{Hz}$. All temporal or phase information, however, is lost in this representation. The Wigner transform, on the other hand, shows that at any time t , the signal contains essentially one frequency component that increases linearly with time. This shows clearly the advantage of the Wigner transform, as both frequency and phase information are retained.

EXAMPLE 3

In the previous two examples, we considered signals which contained only one frequency at any given time. As a third example, consider a signal consisting of two stationary contributions:

$$x(t) = \sin 2\pi f_1 t + \sin 2\pi f_2 t \quad (B.15)$$

The analytic signal is correspondingly,

$$z(t) = e^{i2\pi f_1 t} + e^{i2\pi f_2 t} \quad (B.16)$$

Substituting into B.1 and simplifying, we obtain

$$W(t, f) = \delta(f - f_1) + \delta(f - f_2) + 2\cos 2\pi(f_2 - f_1)t \cdot \delta\left[f - \left(\frac{f_1 + f_2}{2}\right)\right] \quad (B.17)$$

The first two terms correspond to the two peaks in the spectra at f_1 and f_2 as expected. The third term, however, is an unfortunate byproduct of the non-linear nature of the Wigner transform. It consists of a peak located at the average of the two frequencies, f_1 and f_2 . Unlike the other two peaks, though, it is modulated in time by the factor $\cos 2\pi(f_2 - f_1)t$. Figure B.3 shows a computed Wigner transform for a signal consisting of two sine waves at 30 Hz and 70 Hz. The cross term at 50 Hz appears stationary, but upon closer inspection as shown in figure B.4, it is seen to oscillate in time.

Under certain conditions, this cross term can be avoided, however. For example, if the time series is only weakly non-stationary (i.e. the spectral content of the signal changes slowly with time), the cross term can be removed by low-pass filtering $W(t, f)$ in time at each frequency component. That is, for each frequency component f_i , we have a time series $W(t, f_i)$ which can be low-pass filtered to remove the cross term. The result of this operation is shown in figure B.5 in which the Wigner transform of figure B.4 has been filtered with a cutoff frequency of 10 Hz. In this way, non-stationary oscillations slower than 10 Hz are allowed to remain. Higher frequency non-stationary oscillations, however, are eliminated. In this case, only the two stationary components at 30 Hz and 70 Hz remain.

We have therefore identified two types of time series for which the Wigner transform provides a viable means of spectral analysis. The first type is a time series which contains energy at only one frequency at any given time. The second type is a time series which may contain several frequency components, but whose spectral content changes slowly with time. Both of these types of signals are frequently encountered in transition studies such as the present investigation. The observed oscillations are typically quite band limited, and changes in spectral content (i.e. due to Re variation, vortex pairing, etc.) occur rather slowly compared to the frequency of oscillation of the disturbance.

APPENDIX C

MICROPROCESSOR CONTROL AND DATA ACQUISITION SYSTEM

As indicated earlier, a small microprocessor system was used for control of various aspects of the experiments as well as for data acquisition. Figure C.1 shows a block diagram of the electronic portion of the experimental apparatus. As can be seen, the microprocessor is central to virtually every aspect of the experiment. Several of the components shown in figure C.1 have already been discussed such as the sensors, anemometers, and the phased heater array control electronics. In this section, we will be concerned primarily with the central microprocessor and the way in which it is interfaced to the other various components of the system.

The entire system was designed and constructed in-house, and it is the purpose of this section to describe only the principal features that pertain to the present experiments. The system is based on an 8-bit central processing unit (CPU), the Intel 8085-AH. The 8085 has an 8-bit data bus and a 16-bit address bus enabling the direct access of 64 kbytes of memory. Though capable of running at 5 Mhz, the present system configuration uses a 2 Mhz clock resulting in a basic clock cycle of $0.5\mu s$. The 8085 operates in conjunction with an Intel 8155 which provides 256 bytes of local "scratch pad" RAM (Random Access Memory), three I/O (Input/Output) ports, and a timer/counter. In addition, 4 kbytes of ROM (Read Only Memory) are provided on the CPU board, the lower 2 kbytes of which contain the system monitor program.

In order for the CPU to communicate with the various peripheral devices involved in the experiments, a 72-bit system bus was organized containing the 16 address lines, 8 data lines, and a host of control signals established by the CPU and the various peripherals to be described. An 8-bit I/O port (Intel 8212) was used to drive the address and control signals onto the bus, and a bidirectional bus buffer/driver (8216) was employed to assert and/or receive data on the data bus. Figure C.2 shows a functional block diagram of the

above mentioned portion of the system. The remainder of the system can be organized into five logical sub-systems as follows:

1. Operator Interface
2. Data Acquisition/Storage (via DMA Interface)
3. Data Manipulation
4. Phased Heater Array Interface
5. Stepper Motor Interface

These five units communicate with the CPU via the system bus and are schematically shown in relation to the CPU in figure C.3

Operator Interface

To provide for direct access to the CPU, the operator interface consisting of a keyboard/display unit and an optional speech synthesizer were made available. The keyboard contains 24 keys (16 hexadecimal numbers and 8 command keys). It is continually scanned by an Intel 8279 Programmable Keyboard/Display Interface which upon key closure interrupts the CPU. The CPU then executes an appropriate interrupt service routine which is contained within the system monitor. In this way, data and/or any of the instructions contained in the 8085 instruction set may be directed to the CPU.

Data are displayed by the CPU by means of a 6-bit hexadecimal display. The display elements are 7-segment LED's (Light Emitting Diodes) which are organized into a 4-digit (hexadecimal) address field (0000-FFFF) and a 2-digit data field (00-FF). Thus, the contents of the 2^{16} possible addresses may be examined. An additional means of communication with the system is provided by a speech synthesizer. A Votrax SC-01 containing 64 possible phonemes is programmed by the CPU and interfaced via a 2-watt audio amplifier to an 8-ohm front panel speaker. This provides the capability for vocal verification of stored programs and verbal prompts when data entry is requested by the CPU. In addition, the vocal output is quite useful in alerting the operator of any

portions of the experimental apparatus which might be malfunctioning or inadvertently left off-line.

Data Acquisition/Storage (via DMA Interface)

This portion of the system contained the necessary hardware for acquisition and mass storage of data from the various transducers involved in the experiments. The data acquisition circuitry was fairly extensive and was physically housed in a separate enclosure. The system was built around the Analog Devices DAS1128, a 16-channel, 12-bit, 50 KHz A/D converter. The 16-channels were time multiplexed into a single converter, thus the maximum sampling rate of 50 KHz was achieved if only one channel was sampled. With all 16 channels in operation, the maximum sampling rate per channel is approximately 3 KHz. The 12 bits of data together with the 4-bit channel identification number are latched into two 8-bit parallel ports (Intel 8255) which are then transferred to system RAM under DMA (Direct Memory Access) control. Upon receipt of a request for a DMA transfer from the DAS (Data Acquisition System), the DMA controller issues a hold to the CPU. The CPU then relinquishes control of the bus and allows the DMA controller to transfer data from the DAS to system RAM. The time for data transfer is therefore much less than the time required for the CPU to execute the necessary 10 instructions for data transfer.

Continuous data acquisition was achieved by using a double buffering scheme. Data were continuously read into system RAM which was divided into two 2K buffers. When one 2K buffer was filled, data were then routed to the alternate buffer. At this point, a second DMA channel would begin transferring the contents of the filled buffer to the AED-62000 floppy disk. These two processes of data acquisition and data storage were conducted simultaneously by separate DMA channels at independently programmable transfer rates. Transfer to the floppy, however, was always faster than the sampling thus enabling continuous throughput. Double density, double sided, eight inch floppy

disks were used for data storage and had a maximum capacity of 1 Mbyte. These were subsequently stored on magnetic tape for further processing and data reduction.

Data Manipulation

This section of the system contains that portion of the circuitry in which data and/or instructions are stored and manipulated by the CPU. 16 kbytes of RAM are provided for temporary storage of data and instructions, and 8 kbytes of ROM are available for permanent storage of program instructions. In addition, several RAM locations were reserved and were decoded to provide access to several peripheral devices on the system bus. This technique, known as memory mapping of peripherals, was used in conjunction with I/O mapping in order to provide for the large number of devices controlled by the CPU. The phased heater array, for instance, was seen by the CPU as 32 separate address locations, one corresponding to each of the 32 heaters.

An arithmetic processing unit (Intel 8231) with an additional 4K RAM and 4K EPROM was also provided to augment the data manipulation capabilities of the CPU. Data were written into the APU storage registers by the CPU along with the appropriate instruction codes. A very extensive list of possible functions (multiplication, division, exponentiation, sin, cos, etc.) could be performed by the APU in either 16 or 32-bit fixed formats or a 32-bit floating point data format. As an example of the capability of the APU, an FFT algorithm was written which performed a 1024-point FFT in approximately 10 sec. The various capabilities of the APU were used for a wide range of data manipulations, making the system as a whole extremely versatile for general laboratory use.

Phased Heater Array Interface

A general overview of the organization of the phased heater array control electronics was given in Chapter 2. It was shown in block diagram form that signals from a

programmable frequency generator were fed to a block of 32 programmable phase and gain circuits, to the power amplification circuitry, and finally to the heaters. The programmable frequency generator consisted of an 8-bit D/A converter (Analog Devices DAC-0831) and a waveform generator (Intersil ICL-8038). An 8-bit data word written from the CPU was latched by the D/A converter and converted to an analog voltage. This voltage level then determined the frequency to be output by the waveform generator which was hardwired to output a 50 percent duty cycle sinewave from 1 Hz to 50 Hz.

Following this stage were the 32 phase and gain control stages corresponding to each of the 32 heater elements of the array. Figure C.4 shows the circuit diagram of the phase and gain control stages. The circuitry for each heater was identical with the exception of the location at which each is memory-mapped by the CPU. As indicated earlier, the CPU recognizes the heater array as 32 separate memory locations. A single 8-bit word written to one of these addresses is used to program both the phase and gain of the heater voltage. The 8-bit word is latched by an 8-bit parallel latch (74ls373). The upper 4-bits then are level shifted by a quad op-amp (TL074) making the levels compatible with a quad CMOS analog switch (4046). This switch is used to selectively bypass any of the 4 resistor values (10K, 20K, 40K, or 80K) which form part of a constant amplitude phase-shift stage. This provides 16 discrete phase shifts. The output of this stage is then directed to the next neighboring phase-shift stage (i.e. the next heater) and to the gain stage as well.

The lower 4-bits follow a similar path through a level shift to an additional analog switch. In this stage, the switch selectively connects the output of the previous phase-shift stage to any or all of the 4 resistor values (20K, 40K, 80K, 160K) which form part of a summing amplifier. If, for example, the signal was connected to all of the resistors, the equivalent impedance of this parallel configuration would be 10K (the same value as the feedback resistor), and this stage would therefore function simply as a unity gain

amplifier. If on the other hand, the signal from the phase-shift stage was connected only to the 160K resistor, then the output voltage would be 1/16 of its original value. In this way, 16 discrete voltage levels are possible. The final stage provides a trimming amplifier which is used to compensate for non-uniformities in the heaters.

Stepper Motor Interface

The final section of the digital hardware which is important in the present study is the connection to the mechanical world, namely the interface to the boundary layer traversing mechanism via a feedback controlled stepper motor. A 4-pole stepper motor with a resolution of 200 steps/revolution was used. The motor was driven by a set of 4 appropriately phased pulse trains which were generated by a programmable interval timer (Intel 8254). The pulses were converted to a compatible analog signal by 4 D/A converters (MC-3410). An optical encoder (Datametrics K15 series) was mounted on the shaft of the stepper motor and provided feedback information on the exact position of the traverse. The output of the encoder was connected to the CPU by way of 2 of 4 available A/D converters (Analog Devices AD570). Both the A/D and the D/A converters were interfaced to the CPU through several Programmable Peripheral Interfaces (Intel 8255).

The stepper motor was then connected to a traversing gear through a flexible shaft coupler. The traverse converted one revolution of the shaft into a 1.0 mm displacement normal to the plate surface. During boundary layer profile measurements, the increment in the vertical direction was 0.1 mm or one tenth of a revolution. The hot-film velocity probe was connected to the traverse by the supporting structure as discussed in Chapter 2.

References

- Benny, D. J. and Lin, C. C. (1960). On the Secondary Motion Induced by Oscillations in a Shear Flow. *Phys. Fluids* **7**, 319-326.
- Benny, D. J. (1961). A Non-Linear Theory for Oscillations in Parallel Flow. *J. Fluid Mech.* **10**, 209-236.
- Benny, D. J. and Gustavsson, L. H. (1981). A New Mechanism for Linear and Non-Linear Hydrodynamic Instability. *Stud. Appl. Math.* **64**, 185-209.
- Classen, T. A. C. M. and Mecklenbrauker, W. F. G. (1980). The Wigner Distribution: A Tool for Time-Frequency Signal Analysis. *Phillips Journal of Research* **35**, no. 3-6.
- Craik, A. D. D. (1971). Non-Linear Resonant Instability in Boundary Layers. *J. Fluid Mech.* **50**, 393-413.
- Herbert, T. (1984). Theory of Plane Poiseuille Flow - Theory and Experiment. *Fluid Dynamics Trans.* **11**, 77-126.
- Herbert, T. and Morkovin, M. V. (1980). Dialog on Bridging Some Gaps in Stability and Transition Research. *Laminar-Turbulent Transition* (eds. R. Eppler and H. Fasel), Springer-Verlag, 47-72.
- Imberger, J. and Boashash, B. (1985). Application of the Wigner-Ville Distribution to Temperature Gradient Microstructure: A New Technique to Study Small Scale Variations. Submitted to: *J. Physical Oceanography*.
- Itoh, N. (1980). Three-Dimensional Growth of Finite Wave Disturbances in Plane Poiseuille Flow. *Trans. Japan Soc. Aero. Space Sci.* **23**, 91-103.
- Kachanov, Y. S. and Levchenko, V. Y. (1984). The Resonant Interaction of Disturbances at Laminar-Turbulent Transition in a Boundary Layer. *J. Fluid Mech.* **138**, 209-247.
- Klebanoff, P. S., Tidstrom, K. D., and Sargent, L. M. (1962). The Three-Dimensional Nature of Boundary Layer Instability. *J. Fluid Mech.* **12**, 1-34.
- Liepmann, H. W., Brown, G. L., and Nosenchuck, D. M. (1982). Control of Laminar Instability Waves Using a New Technique. *J. Fluid Mech.* **118**, 187-200.

- Liepmann, H. W. and Nosenchuck, D. M. (1982). Active Control of Laminar-Turbulent Transition. *J. Fluid Mech.* **118**, 201-204.
- Lighthill, M. J. (1950). Contributions to the Theory of Heat Transfer Through a Laminar Boundary Layer. *Proc. Roy. Soc. London A* **202**, 359-377.
- Lin, C. C. (1955). The Theory of Hydrodynamic Instability. *Cambridge University Press*.
- Mack, L. M. (1984). Boundary Layer Stability Theory. *AGARD Special Course on Stability and Transition*, March 26-30, Rhode-St.-Genese, Belgium.
- Mack, L. M. (1984). Line Sources of Instability Waves in a Blasius Boundary Layer. *AIAA-84-0168*.
- Meier, H. U. and Maier, A. (1984). A Preliminary Study on Artificial Transition by Heat Pulsing. Internal Report of the DFVLR, IB-222-84, A 36.
- Nayfeh, A. H. and Bozatli, A. N. (1979). Non-Linear wave Interactions in Boundary Layers. *AIAA-79-1496*.
- Nosenchuck, D. M. (1982). Passive and Active Control of Boundary Layer Transition. *Ph.D. Thesis*, California Institute of Technology.
- Raetz, G. S. (1959). A New Theory of the Cause of Transition in Fluid Flows. Northrop Corporation, Norair Division Report NOR-59-383 (BLC-121).
- Raetz, G. S. (1970). A Hypothetical Model of a Transitional Boundary Layer. Tech Rep. AFFDL-TR-70-123.
- Saric, W. S., Kozlov, V. V., and Levchenko, V. Y. (1984). Forced and Unforced Subharmonic Resonance in Boundary Layer Transition. *AIAA-84-0007*.
- Schubauer, G. B. and Skramstad, H. K. (1947). Laminar Boundary Layer Oscillations and Transition on a Flat Plate. *J. Res. Nat. Bur. Stand.* **38**, 251-292.
- Spalart, P. R. (1984). Numerical Simulation of Boundary Layer Transition. *NASA Technical Memorandum-85984*.
- Squire, H. B. (1933). On the Stability for Three-Dimensional Disturbances of Viscous Fluid Flow Between Parallel Walls. *Proc. Roy. Soc. A*. **142**, 621-628.

- Strykowski, P. J. and Sreenivasan, K. R. (1985). The Control of Transitional Flows. *AIAA-85-0559*.
- Taylor, S. E. (1986). The Effect of Large-Eddy Manipulator Devices on the Turbulent Spot and the Turbulent Boundary Layer. *Ph.D. Thesis*, California Institute of Technology.
- Ward, T. M. (1976). The Hydrodynamics Laboratory at the California Institute of Technology. *Trans. ASME*, Dec., 740-748.
- Williams, D. R., Fasel, H., and Hama, F. R. (1984). Experimental Determination of the Three-Dimensional Vorticity Field in the Boundary Layer Transition Process. *J. Fluid Mech.* 149, 179-203.

FIGURES

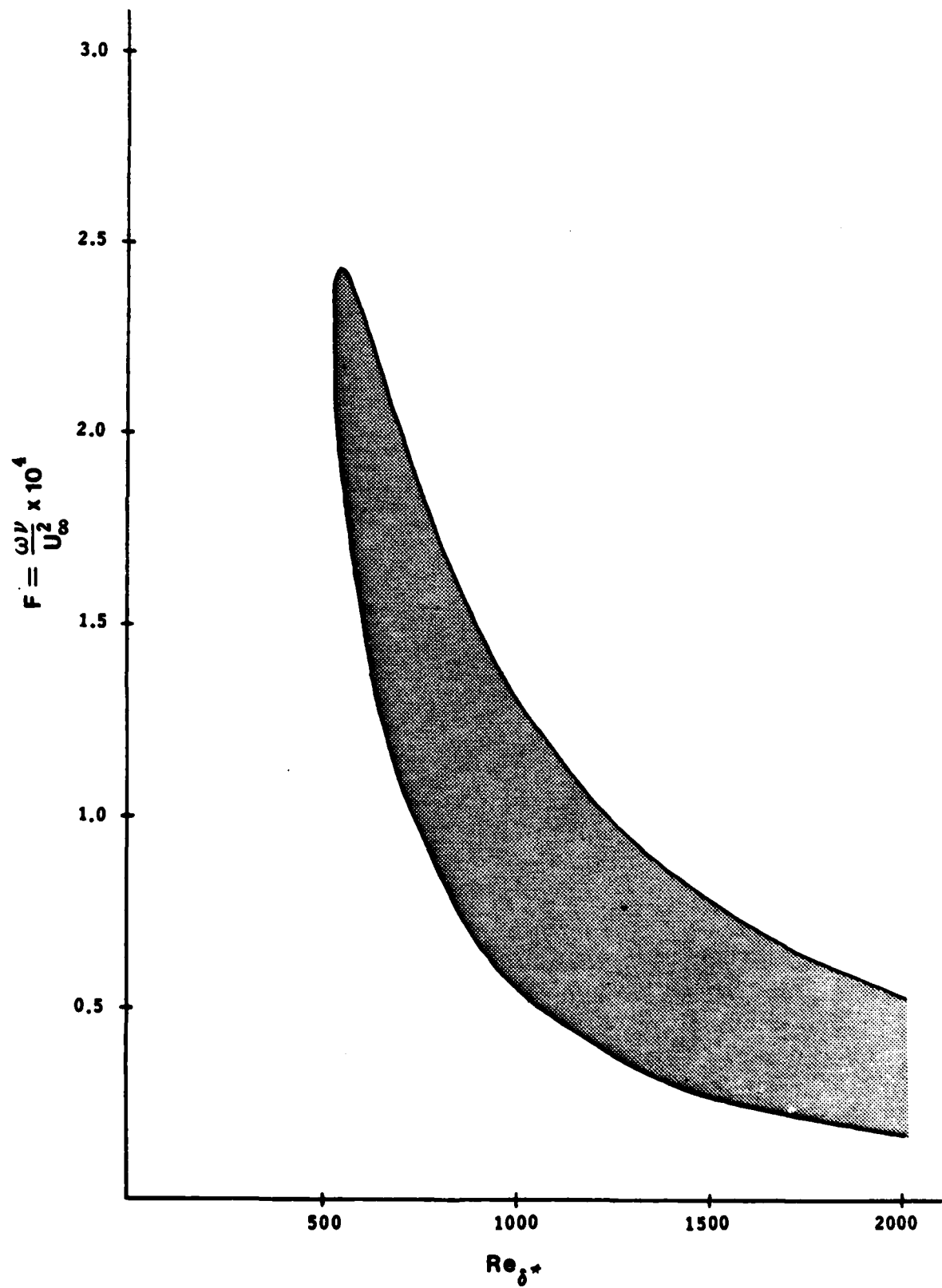


Figure 1.1 Neutral Stability Curve

AD-A188 812

ON THE NATURE OF OBLIQUE INSTABILITY WAVES IN BOUNDARY
LAYER TRANSITION(U) CALIFORNIA INST OF TECH PASADENA
GRADUATE AERONAUTICAL LABS H F ROBEY 23 MAY 86

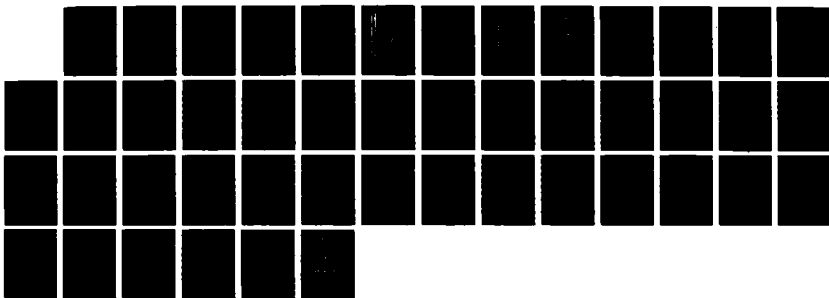
2/2

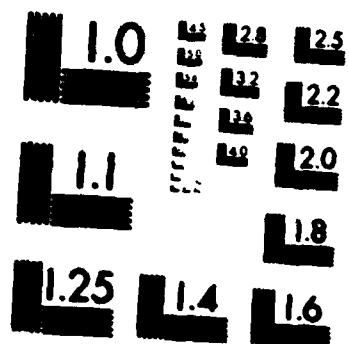
UNCLASSIFIED

NO0014-85-K-0205

F/G 20/4

NL





MICROCOPY RESOLUTION TEST CHART
NATIONAL BUREAU OF STANDARDS-1963-A

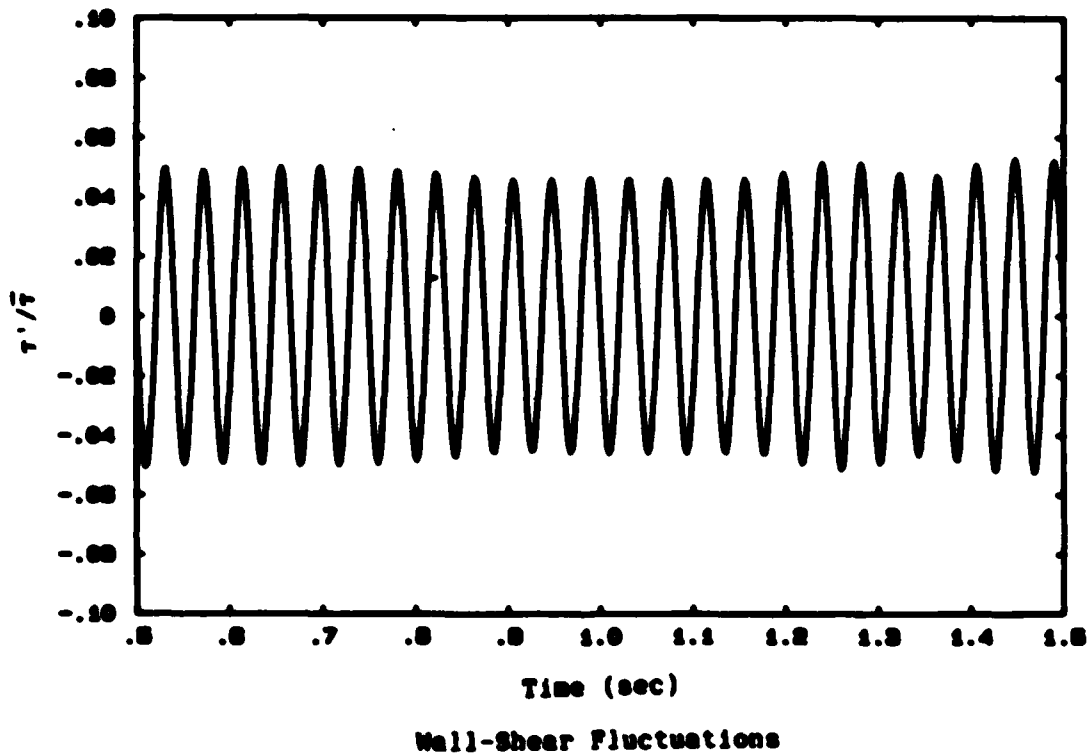
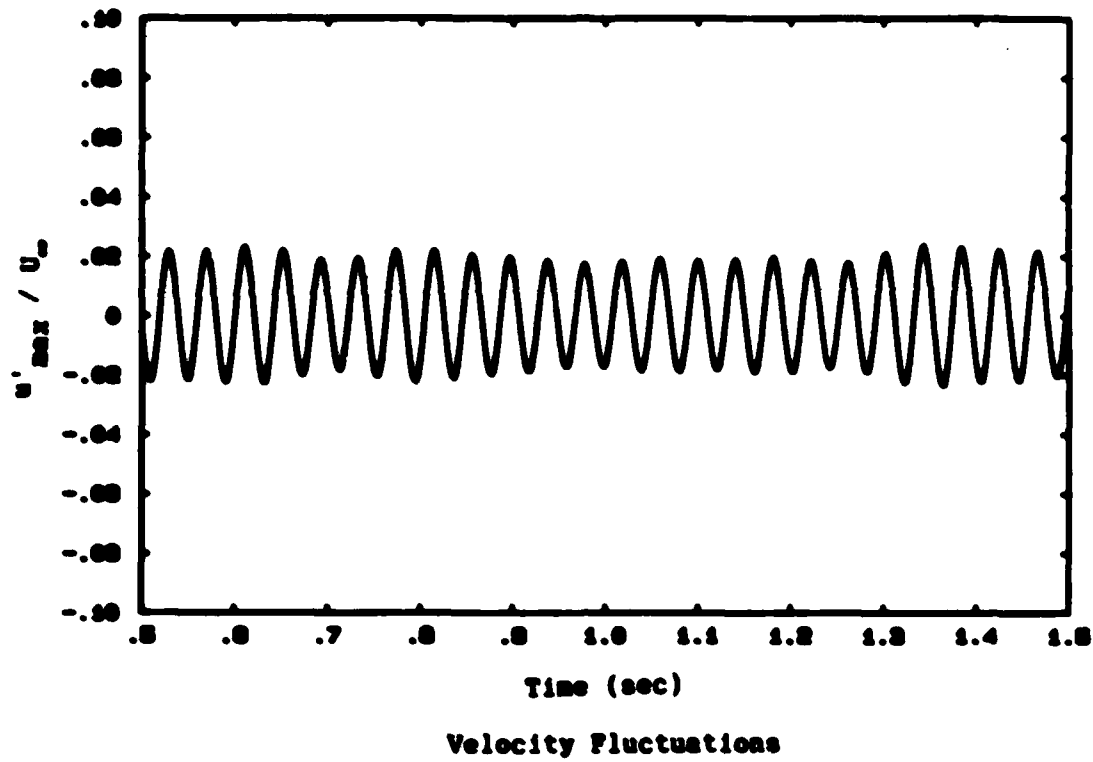


Figure 1.2 Comparison Between Wall-Shear and Velocity Fluctuations

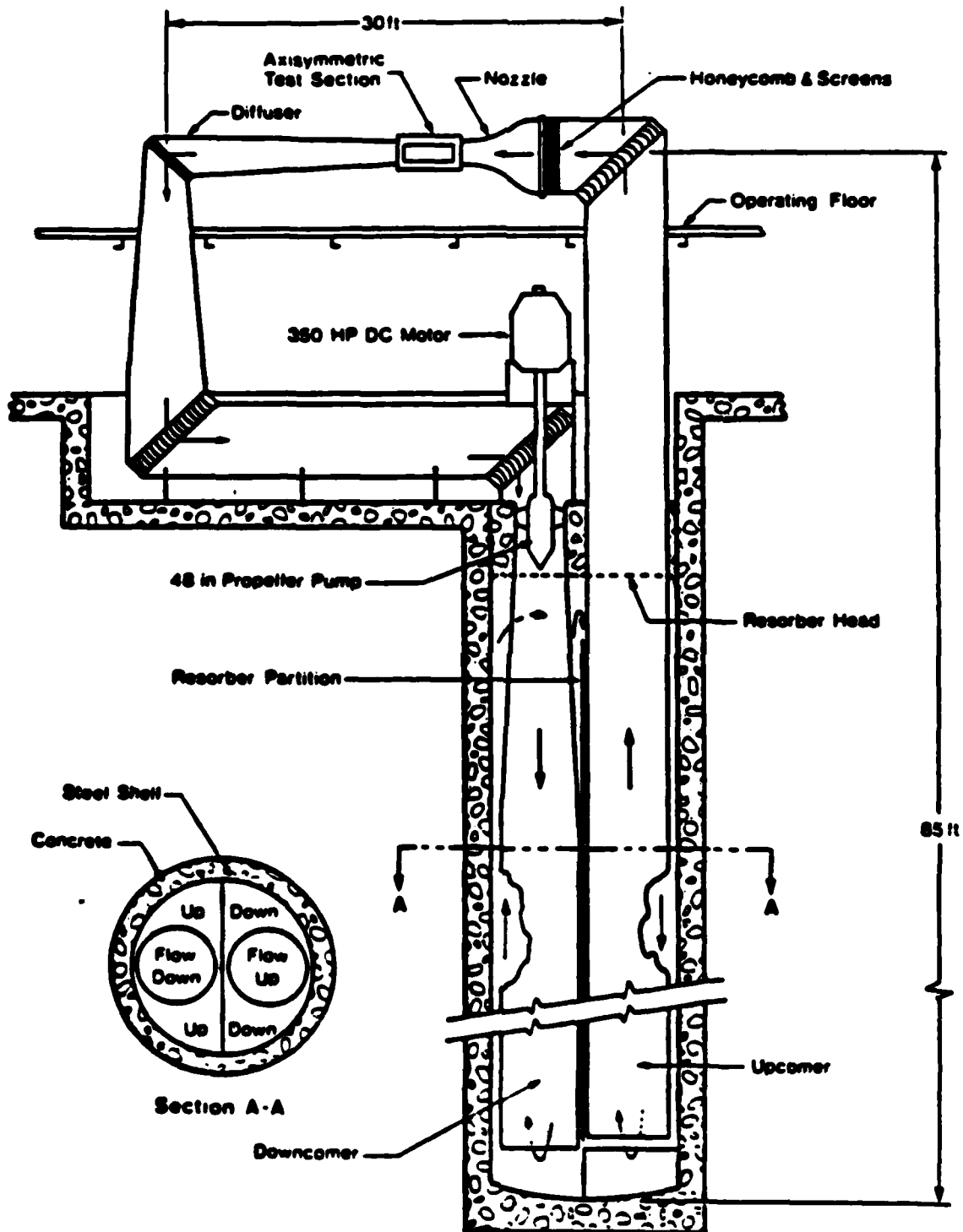
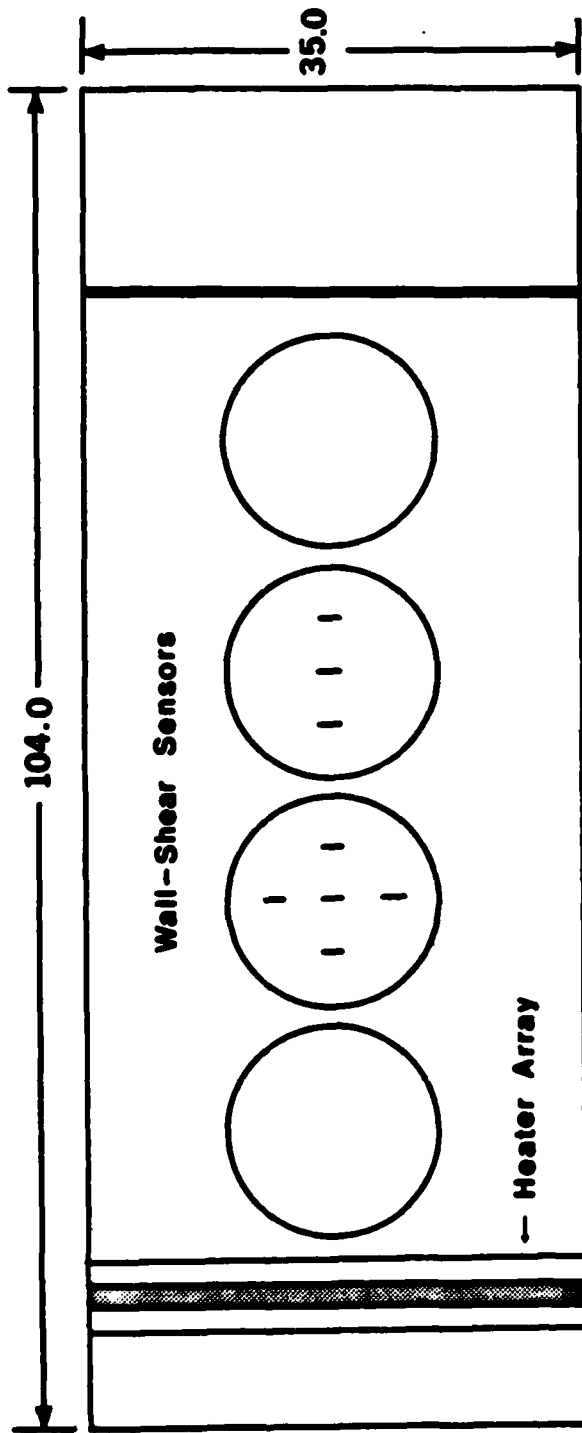


Figure 2.1 GALCIT High-Speed Water Tunnel (HSWT)



Planform View



Side View

Figure 2.2 Schematic Drawing of Flat Plate Model

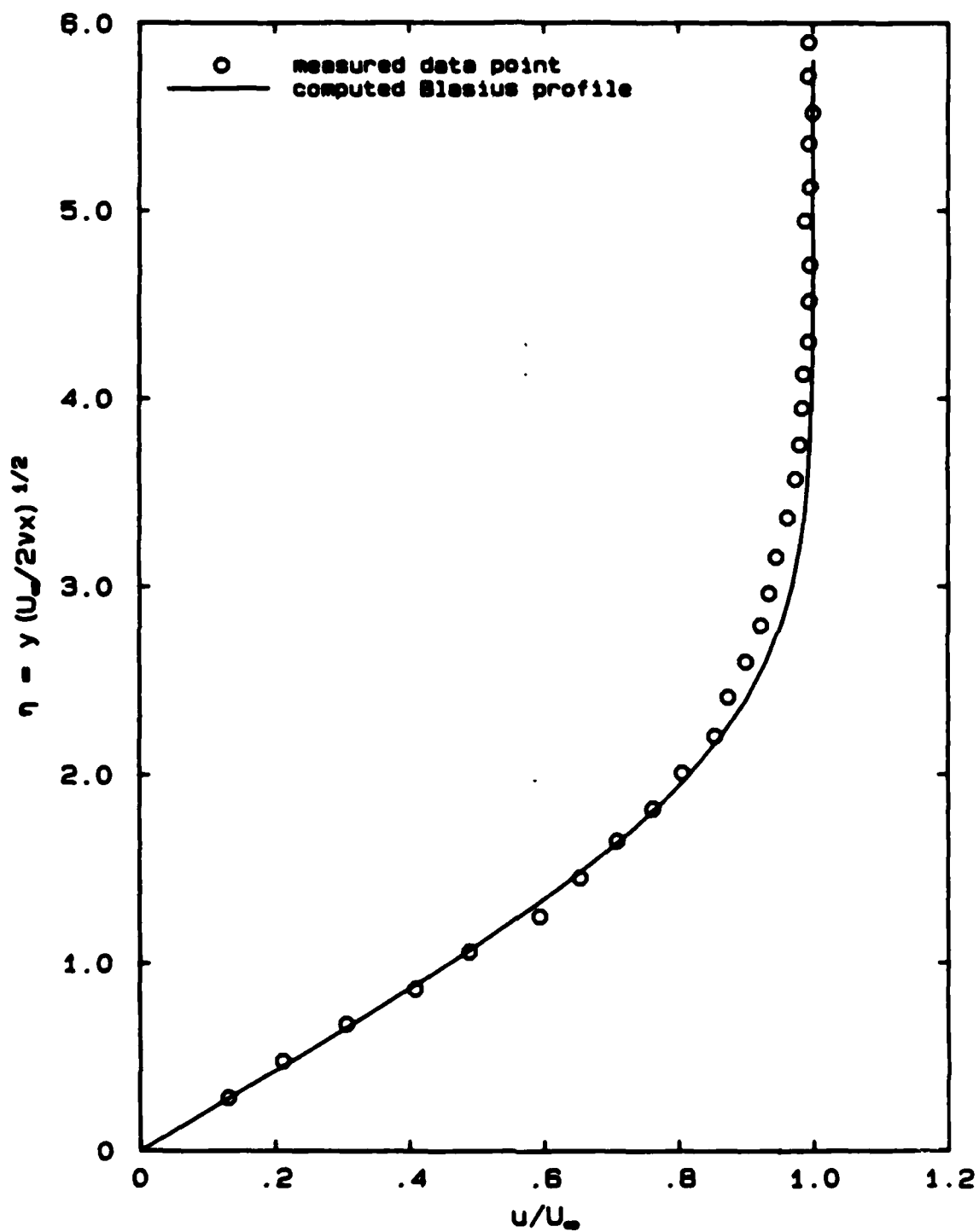


Figure 2.3 Mean Velocity Profile

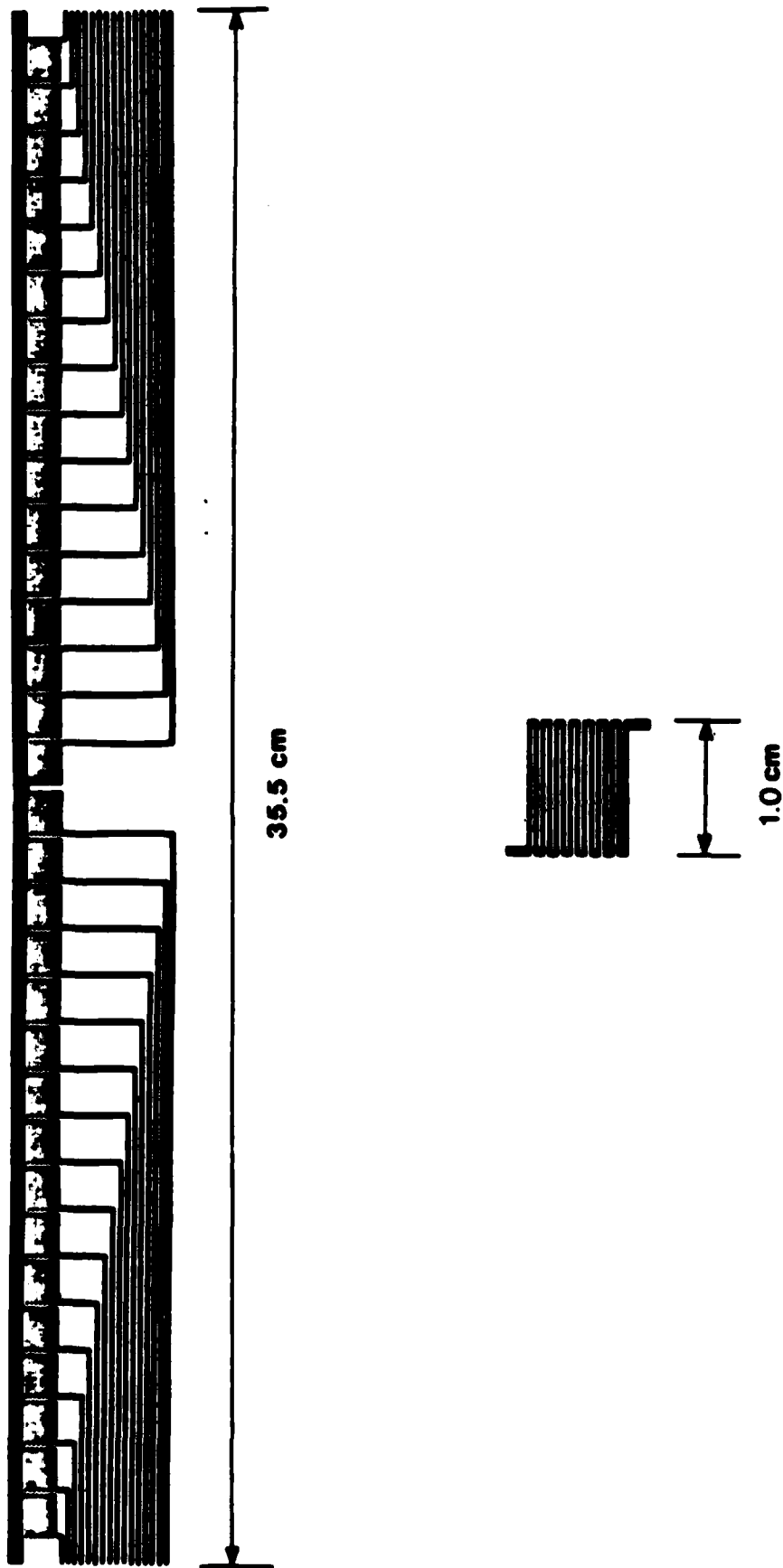


Figure 2.4 Planform View of Phased Heater Array

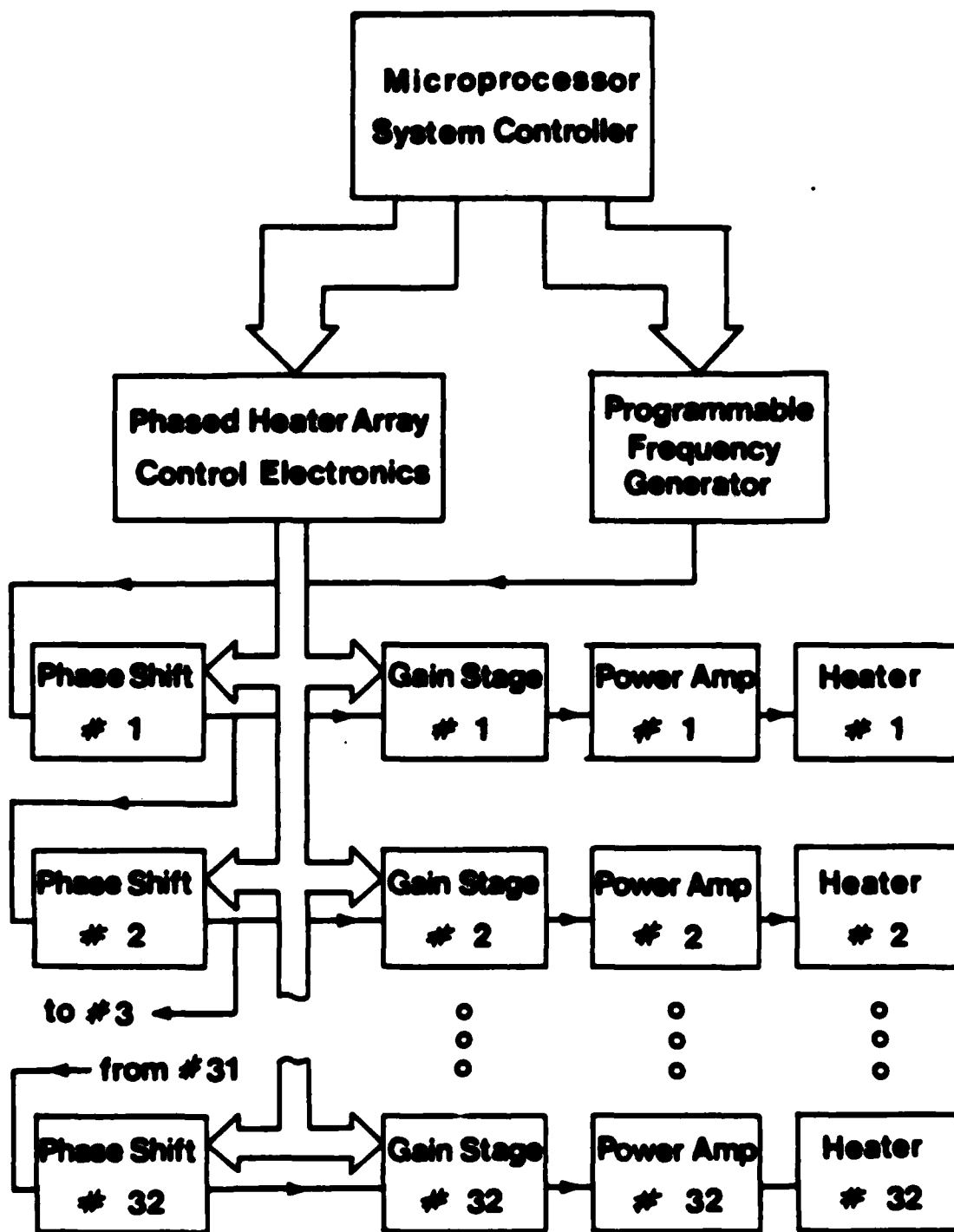


Figure 2.5 Schematic Drawing of Phased Heater Array Control Electronics

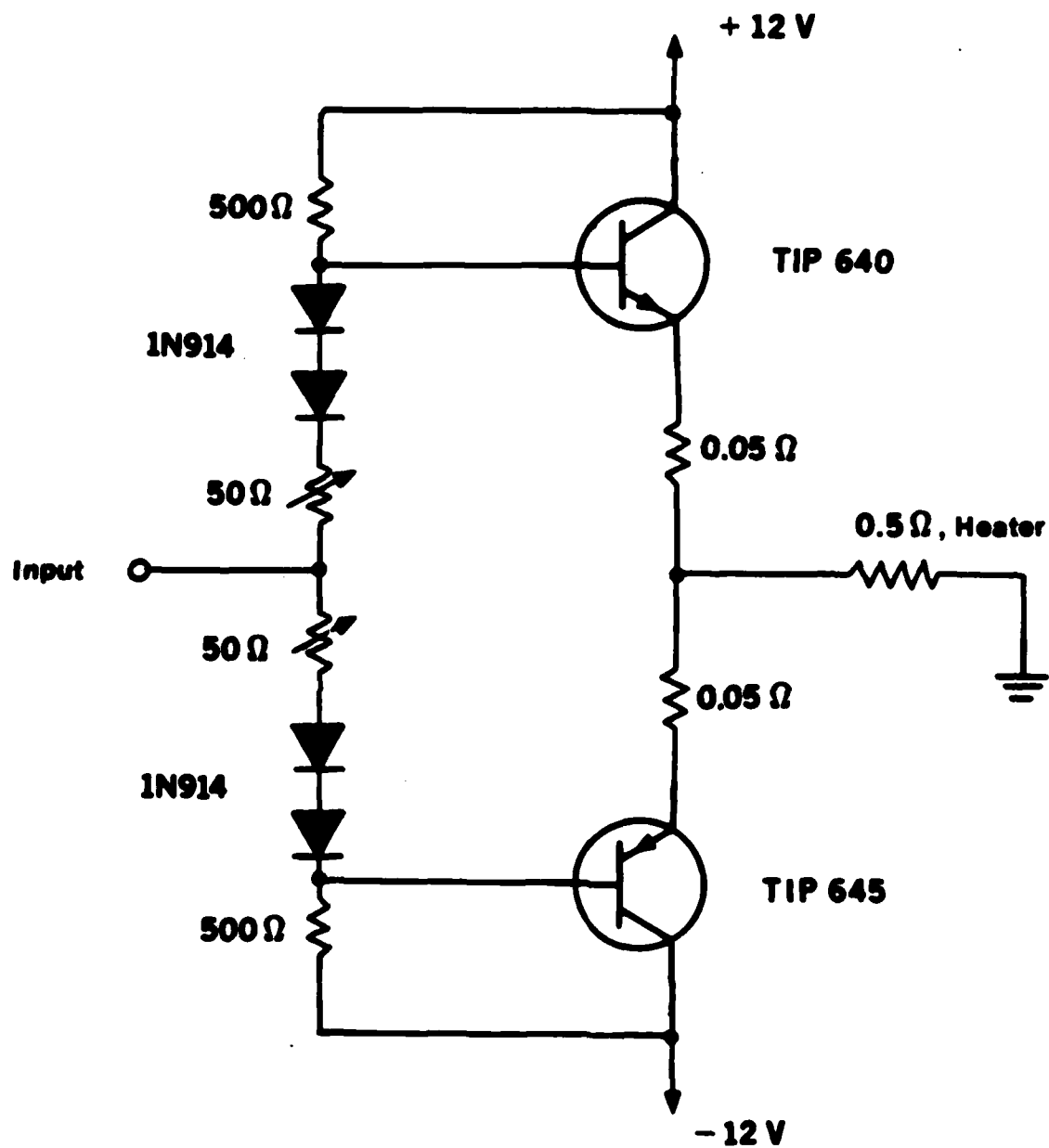


Figure 2.6 Power Amplifier Circuit

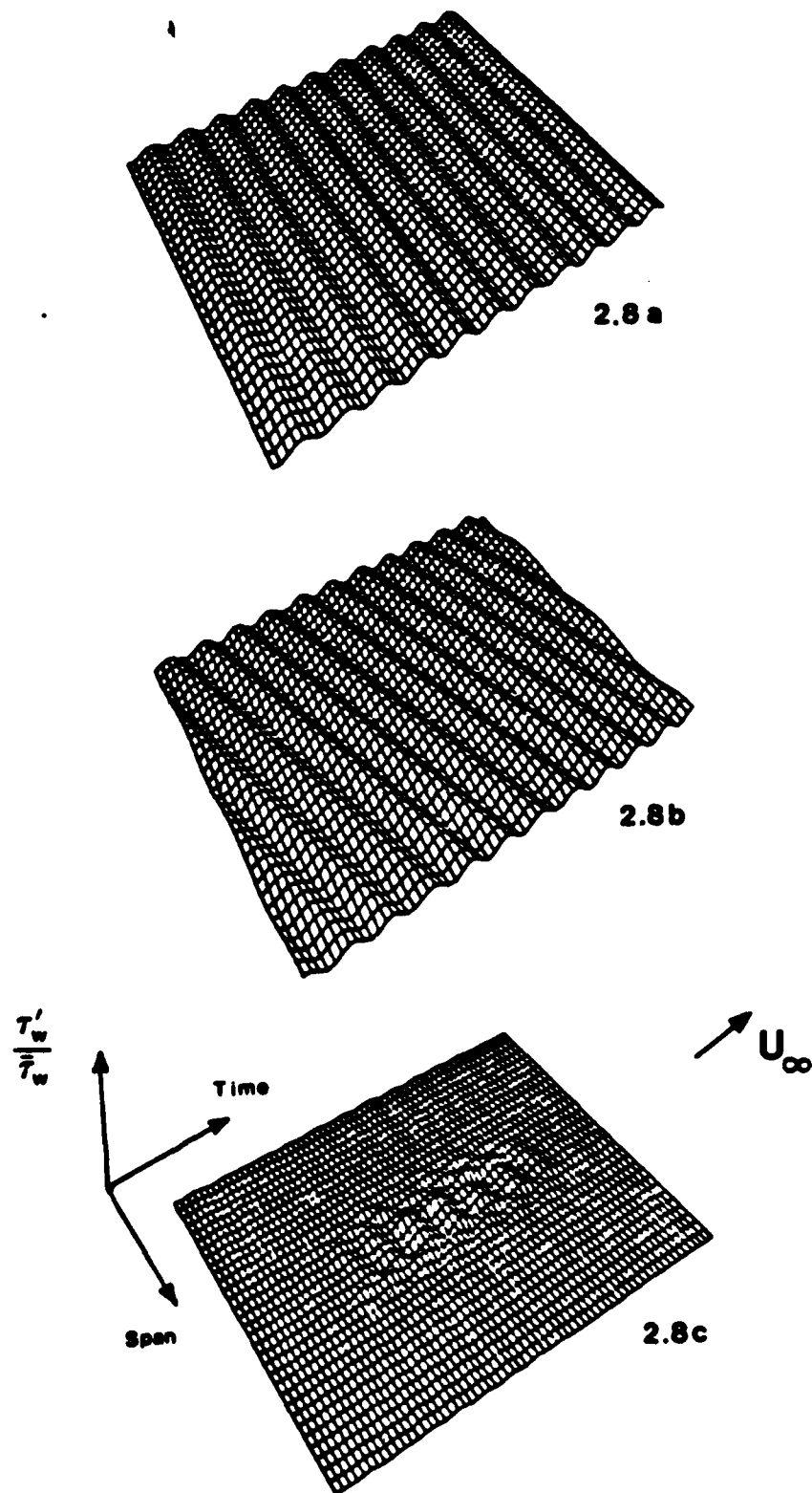


Figure 2.7 Three-Dimensional Views of T.S. Wave 'Surfaces'

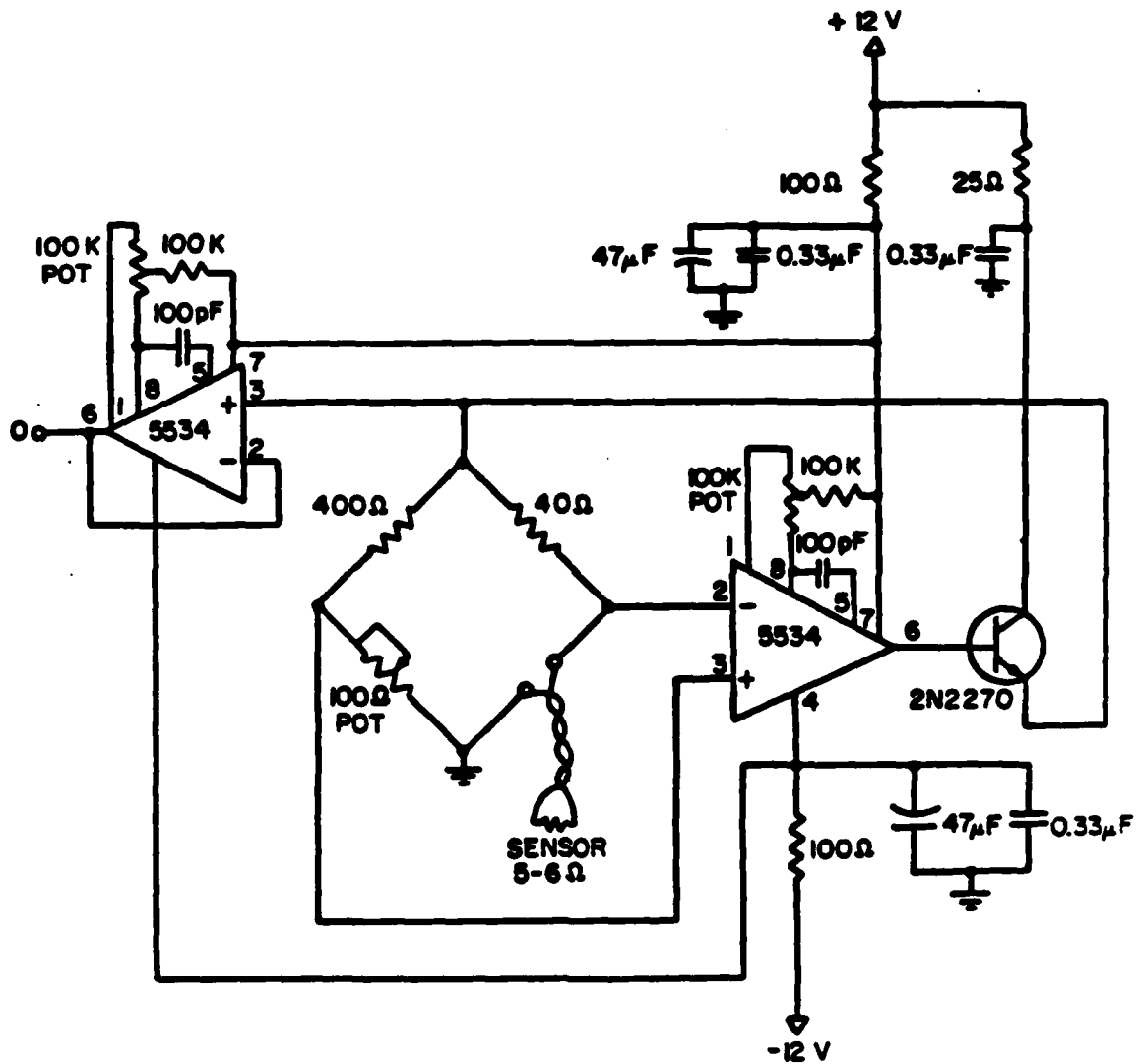


Figure 2.8 Constant Temperature Anemometer Circuit

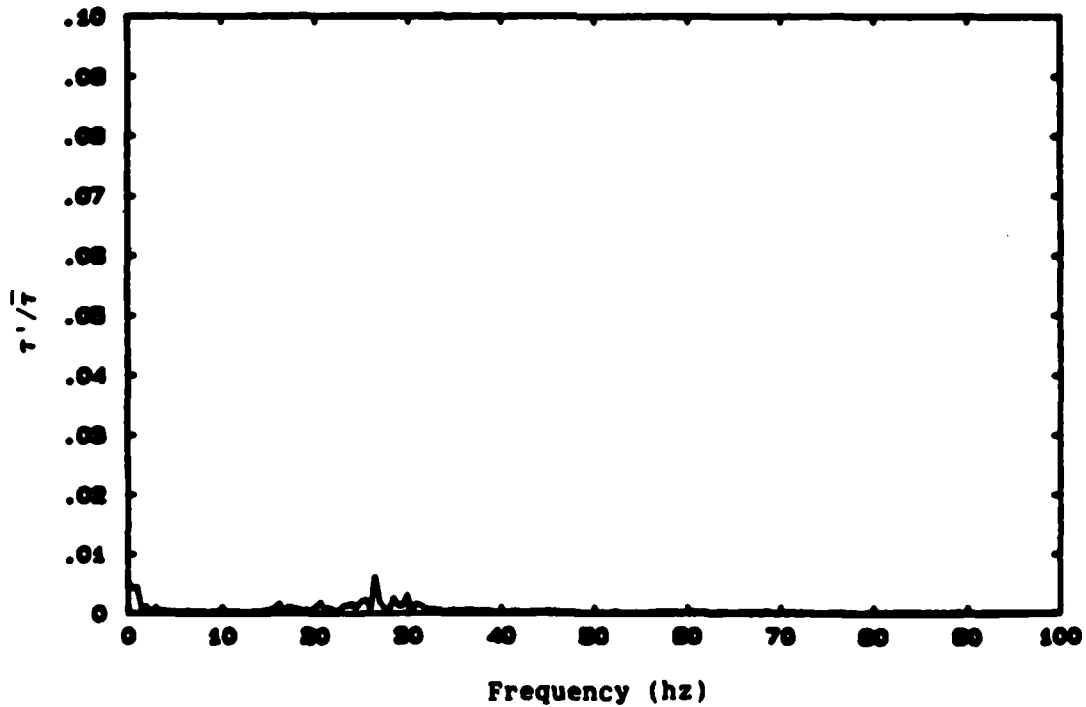
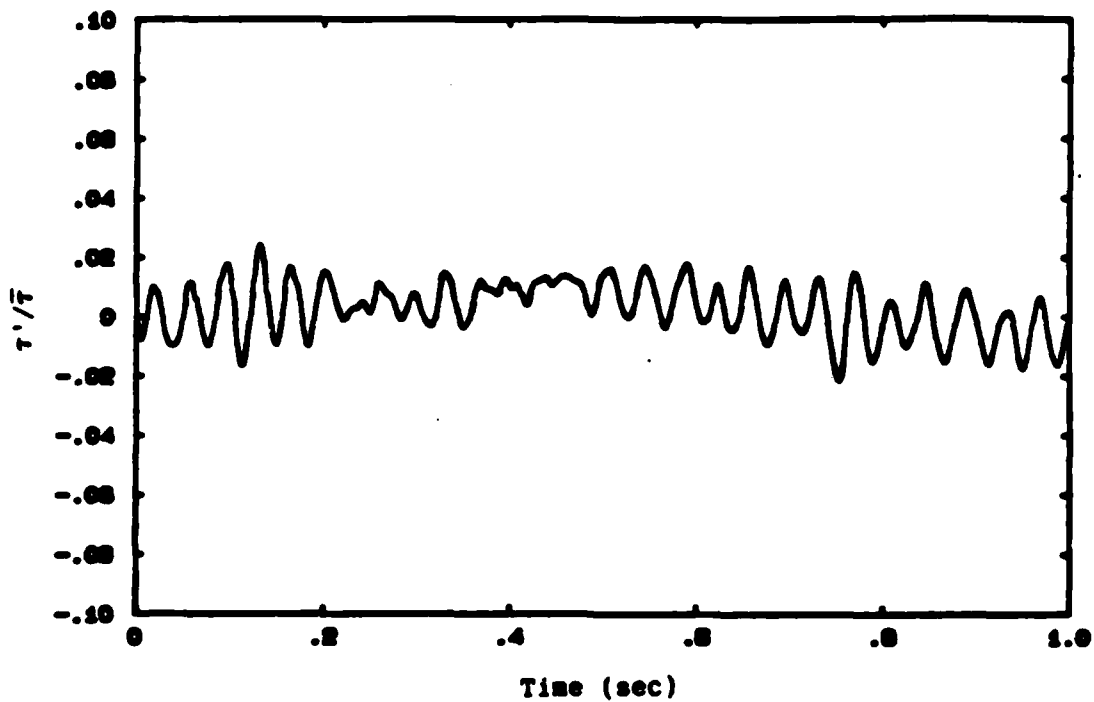


Figure 3.1 Naturally Occurring Tollmien-Schlichting Waves

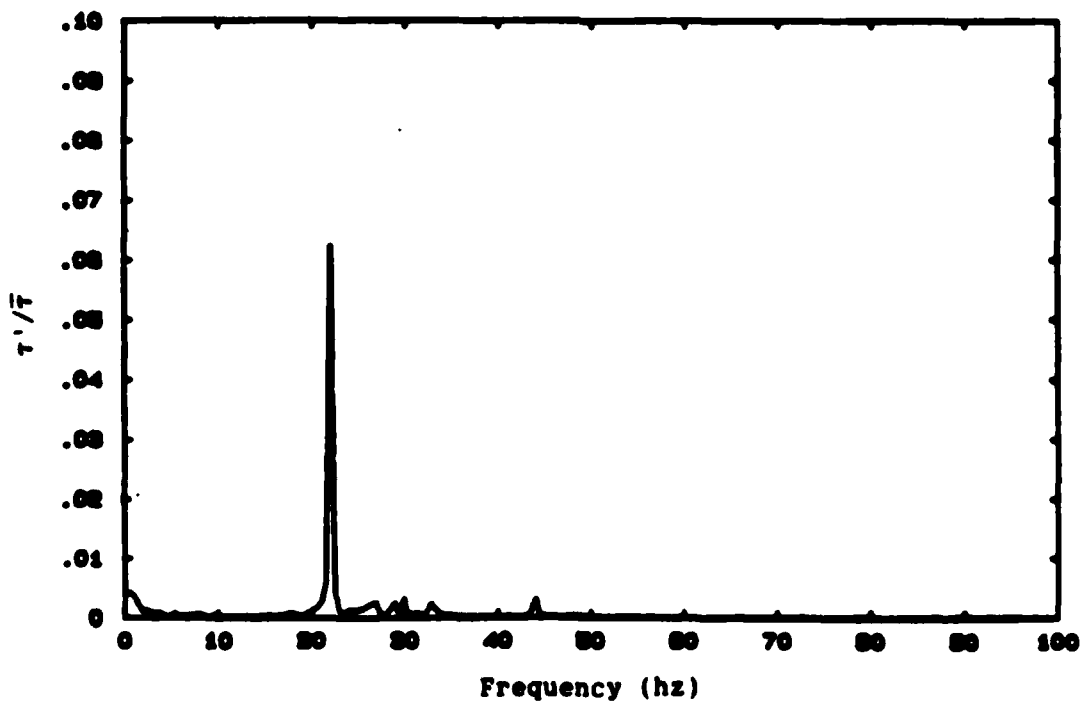
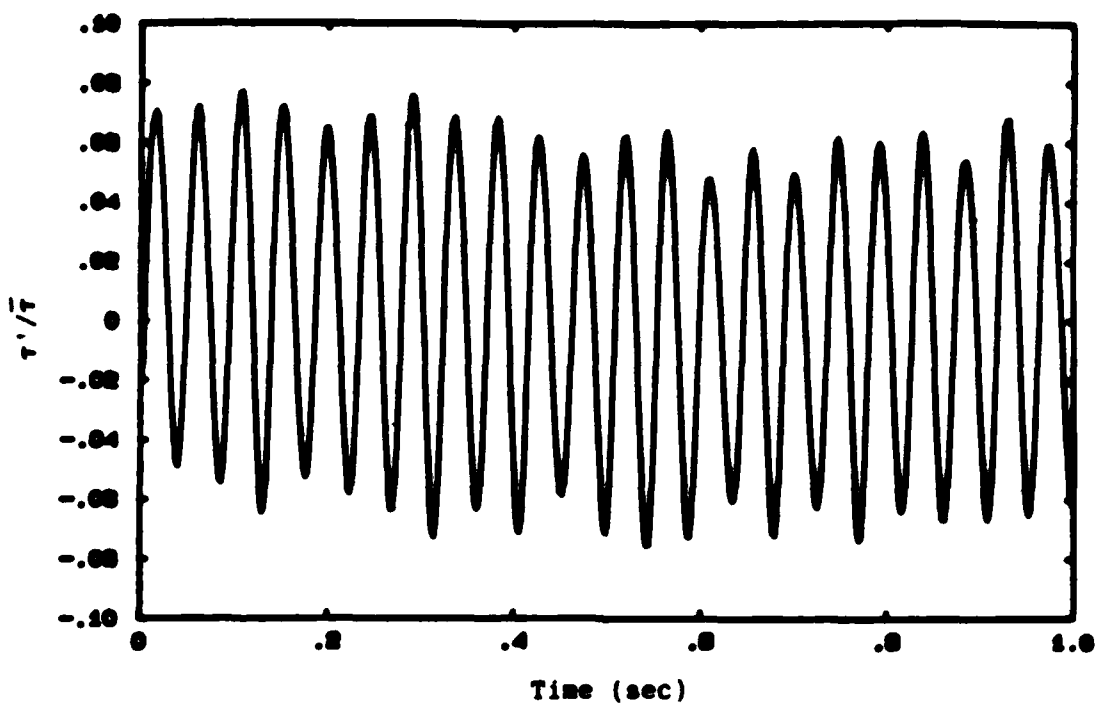


Figure 3.2 Forced Two-Dimensional Tollmien-Schlichting Waves

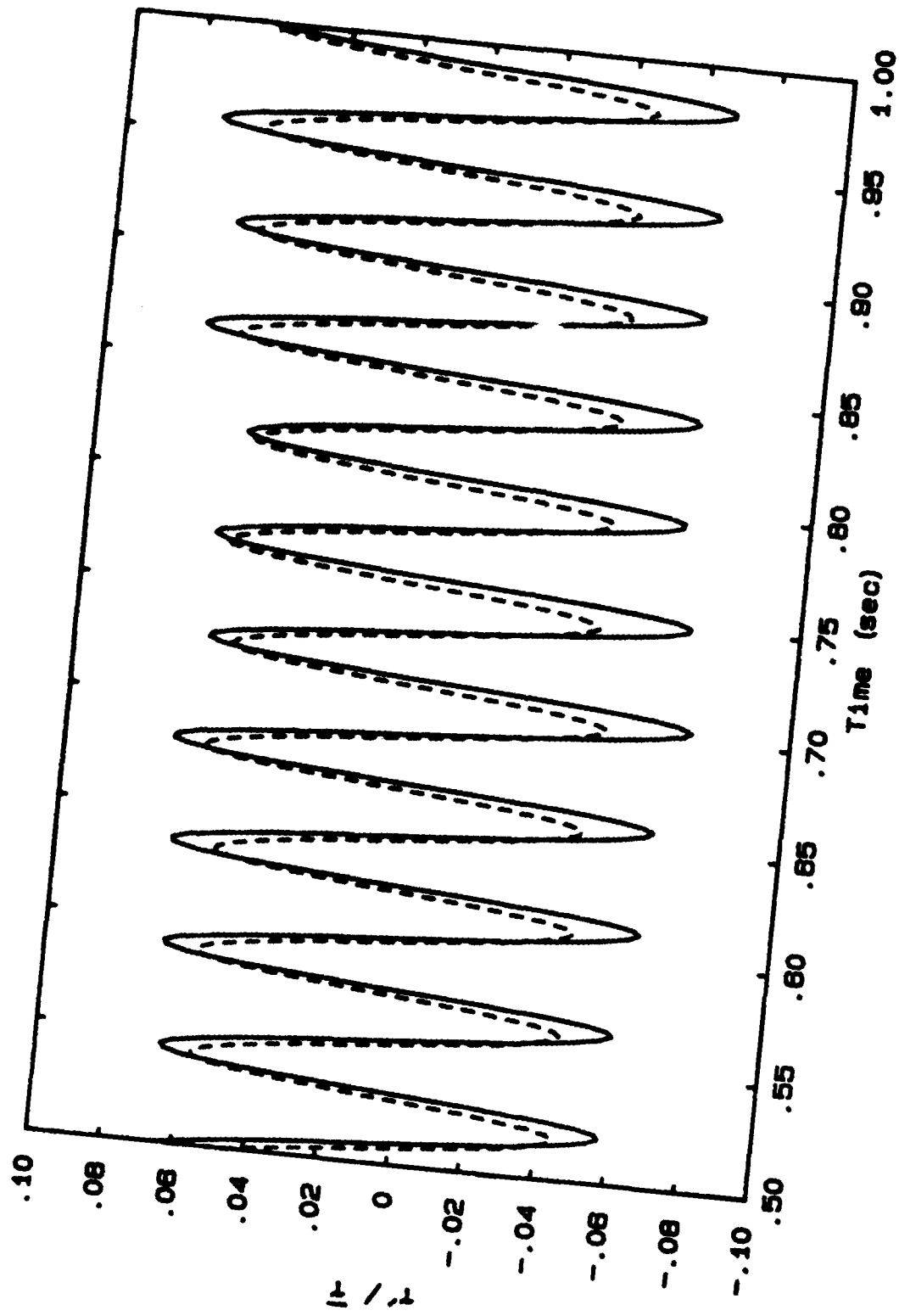


Figure 3.3 Two-Dimensionality of Forced Waves

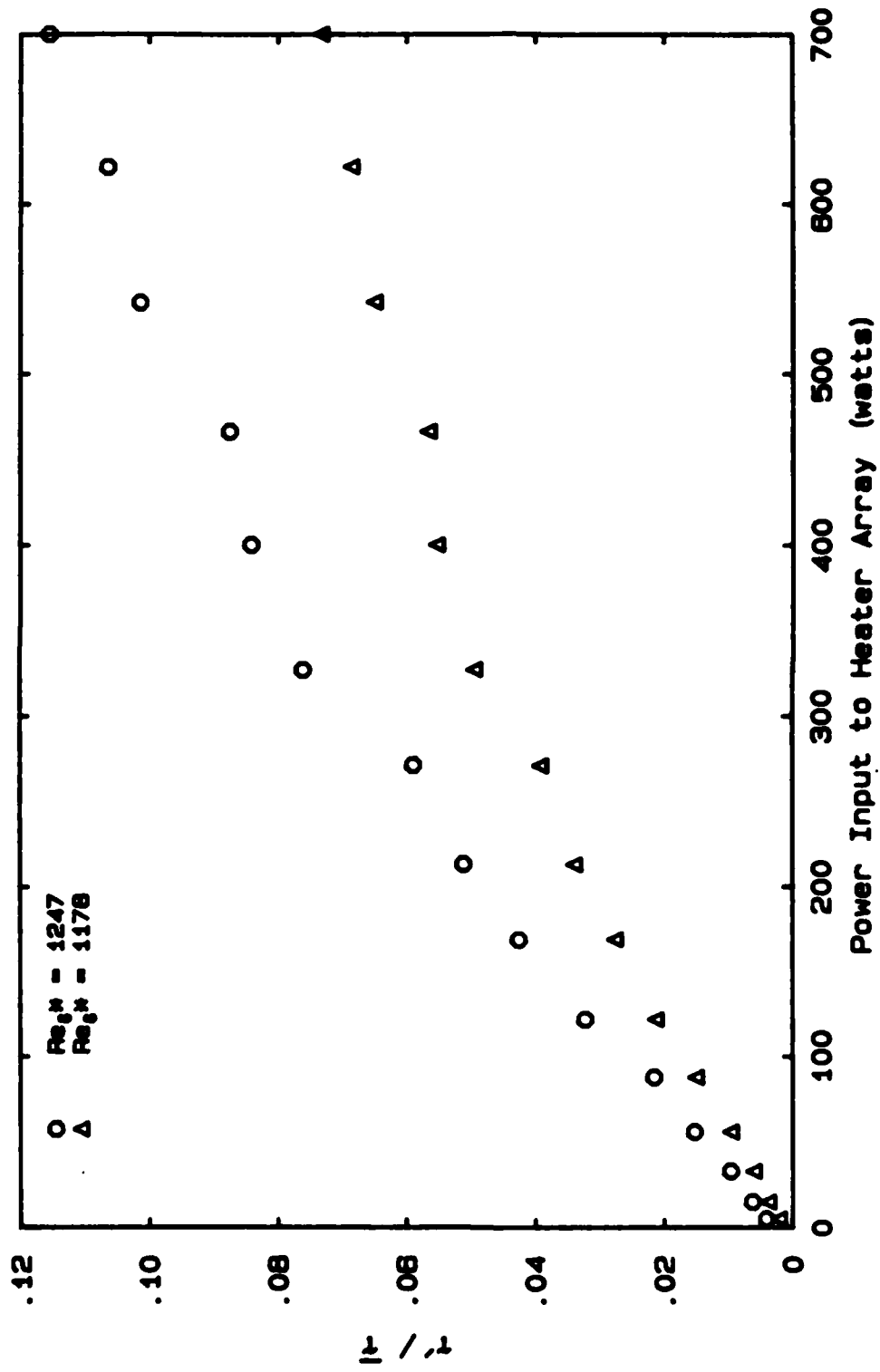


Figure 3.4 Disturbance Amplitude vs. Forcing Level

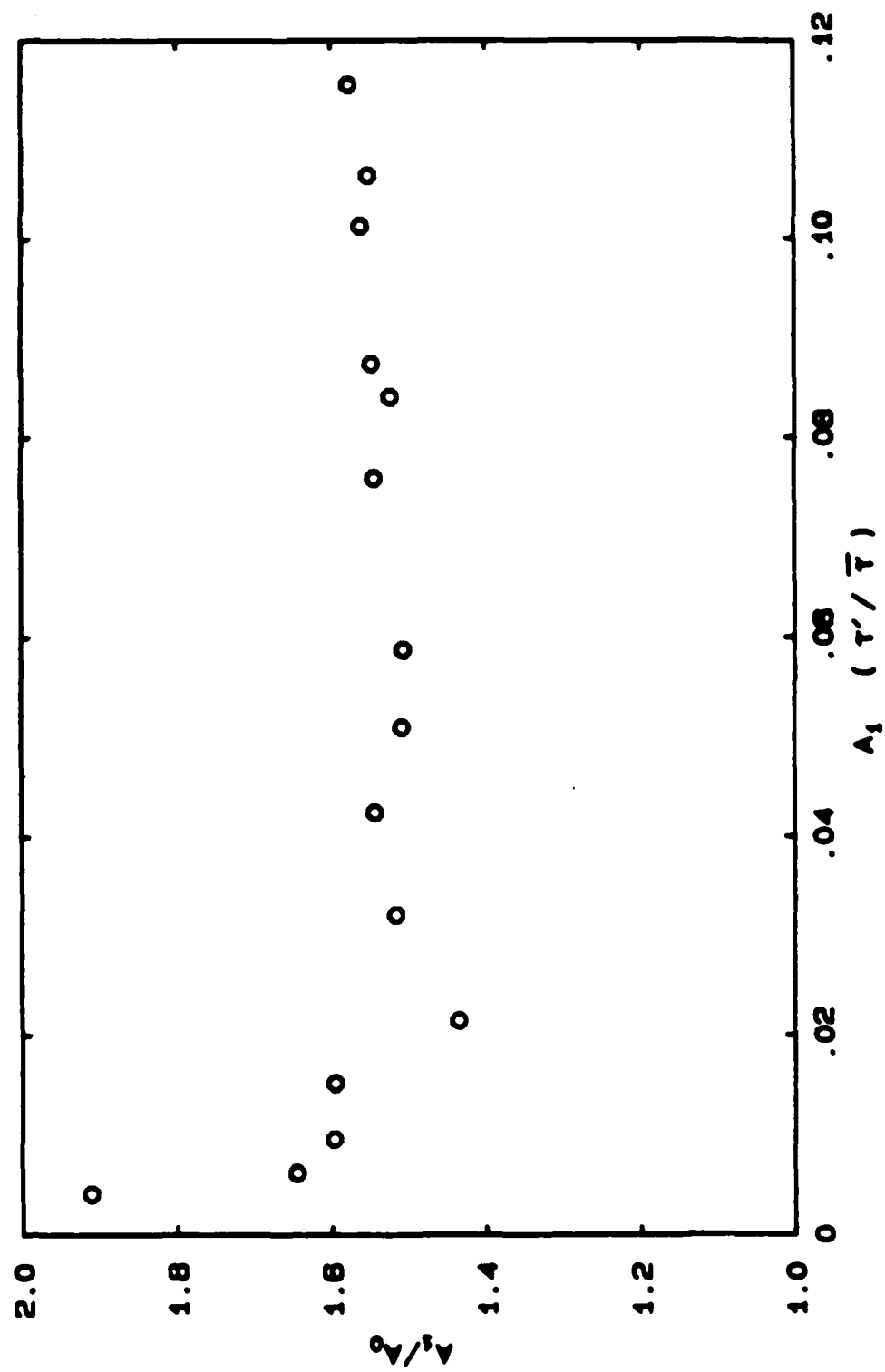


Figure 3.5 Disturbance Amplification vs. Disturbance Amplitude

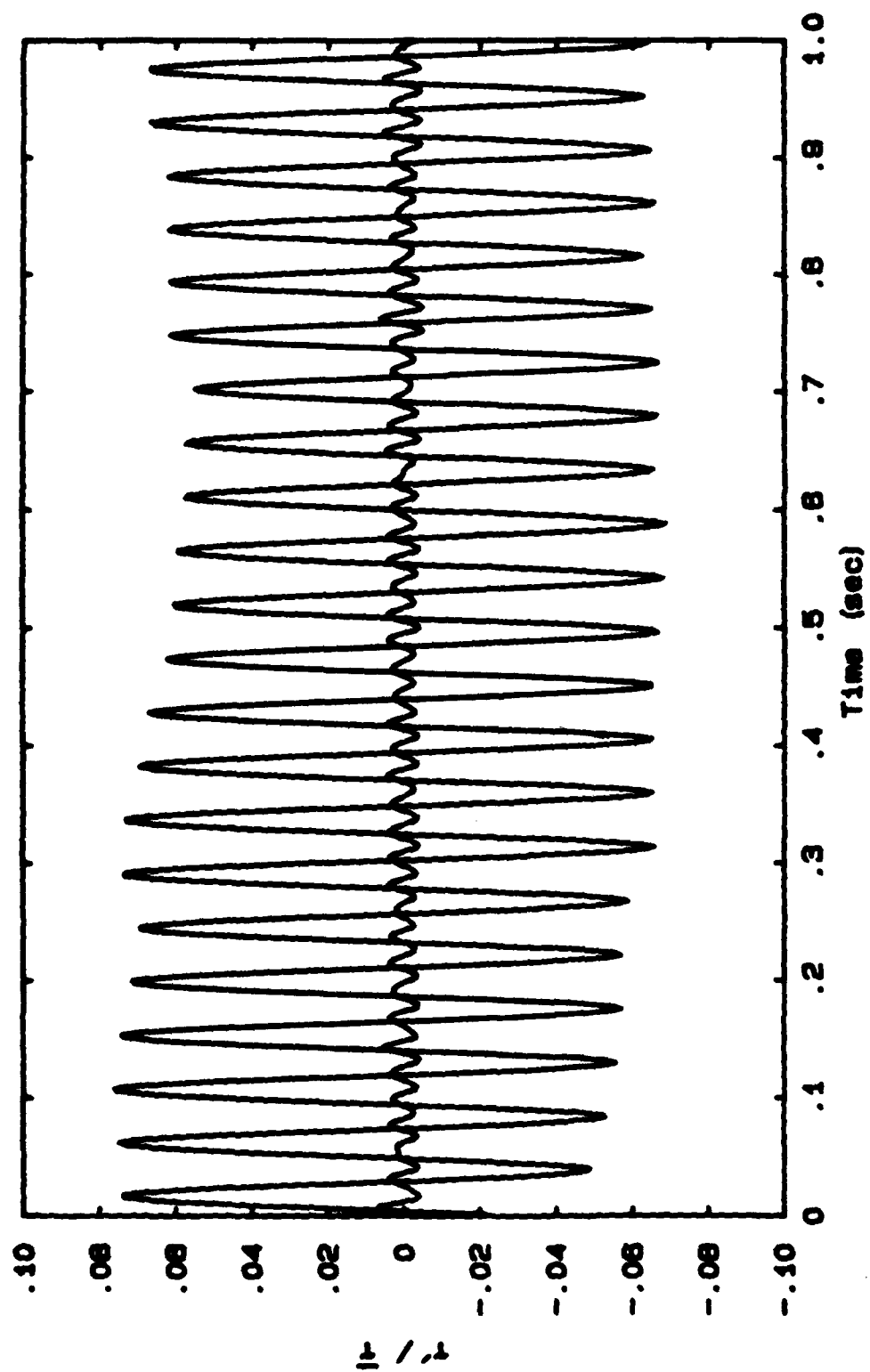


Figure 3.6 Time-Series Behavior of Fundamental and First Harmonic

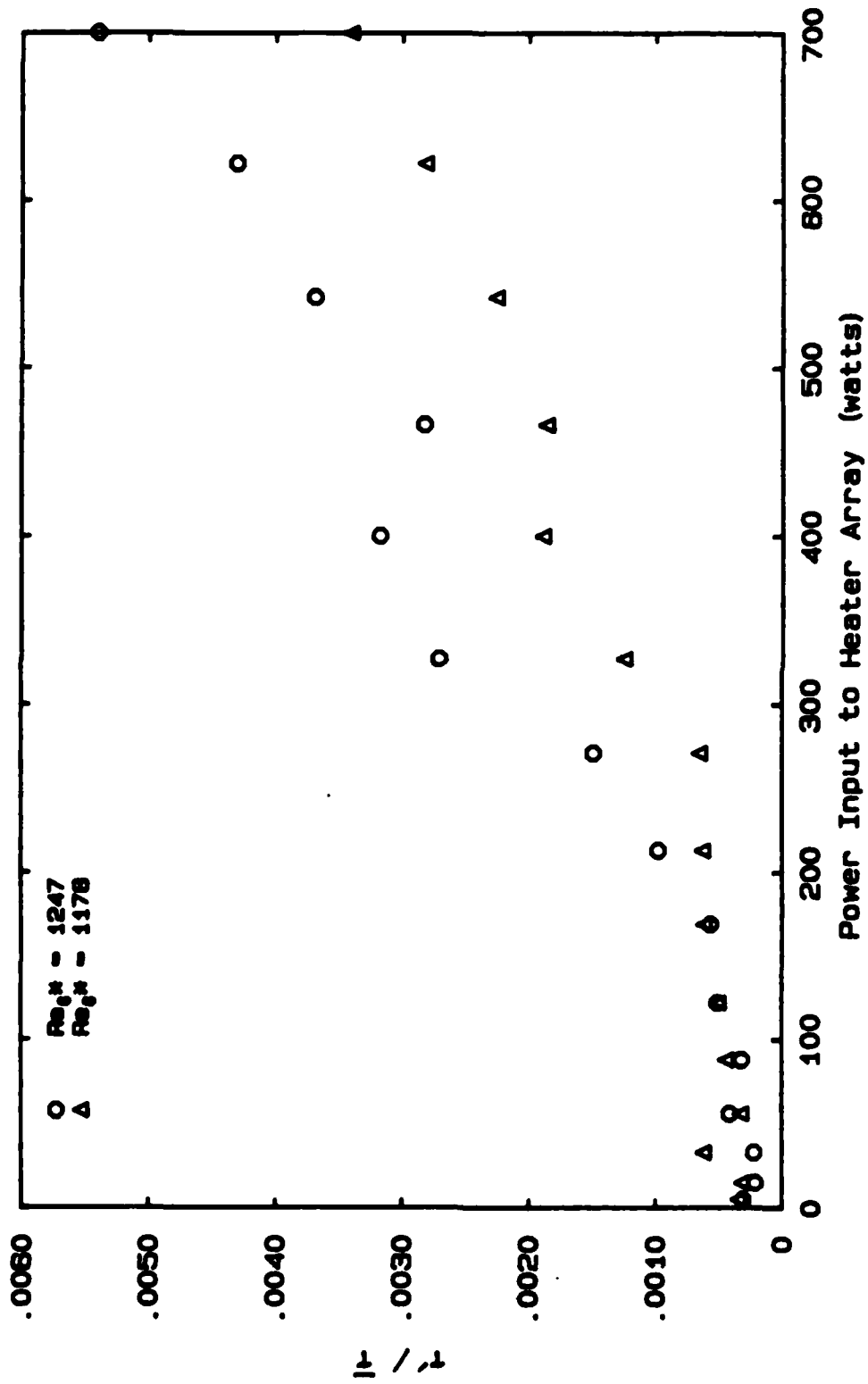


Figure 3.7 Amplitude of First Harmonic vs. Forcing Level

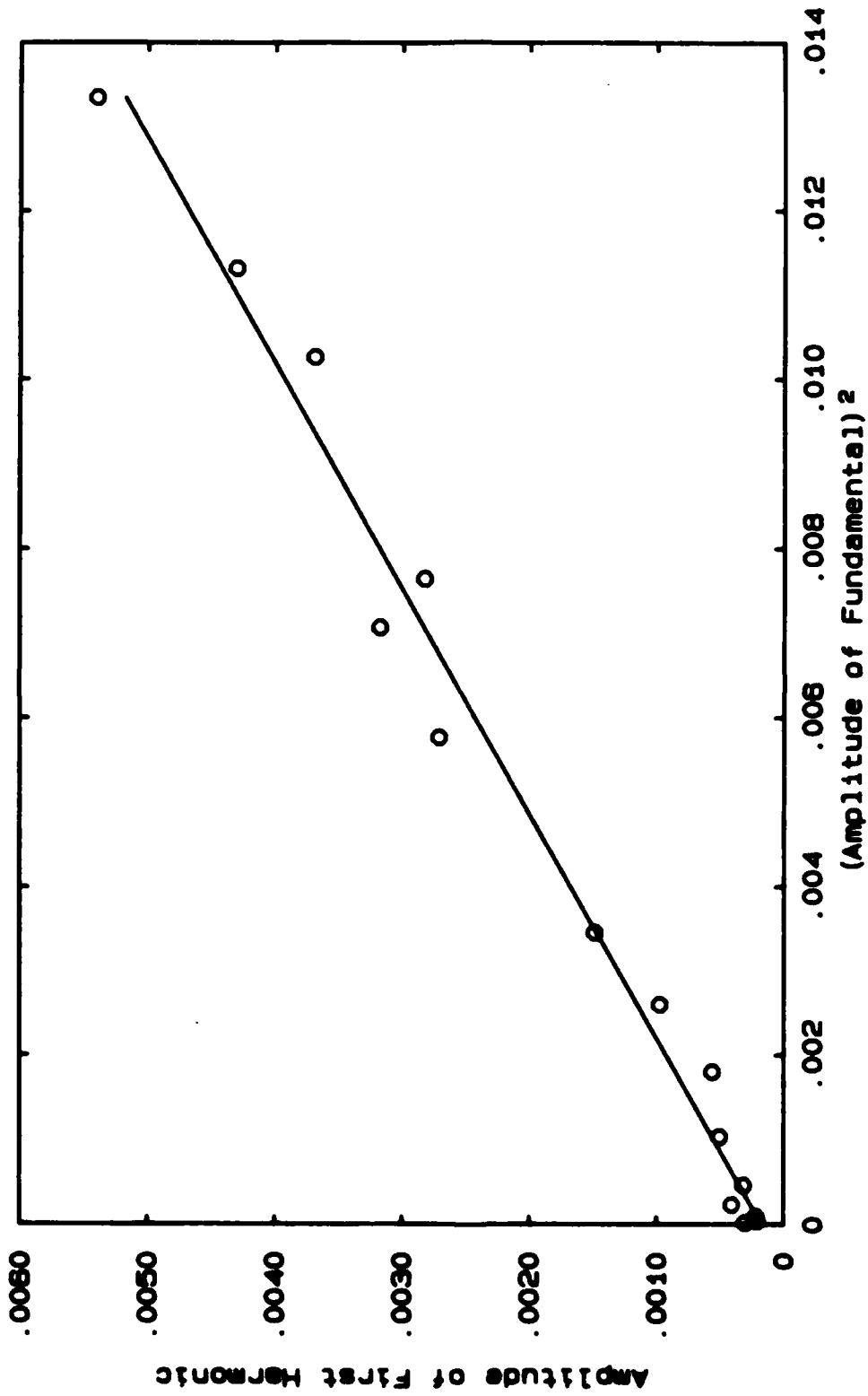


Figure 3.6 Amplitude of First Harmonic vs. Amplitude of Fundamental

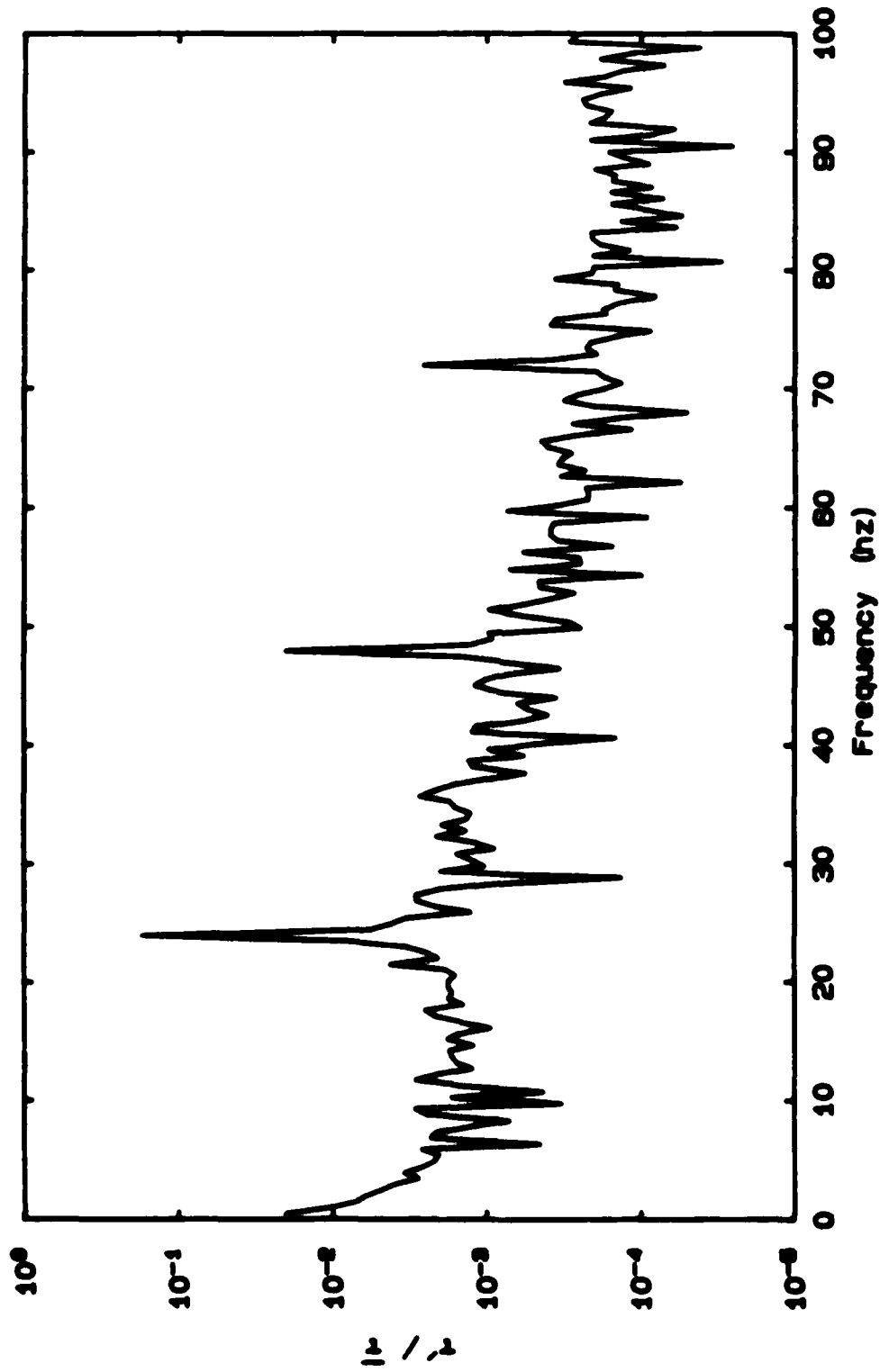


Figure 3.9 Appearance of Higher Harmonics

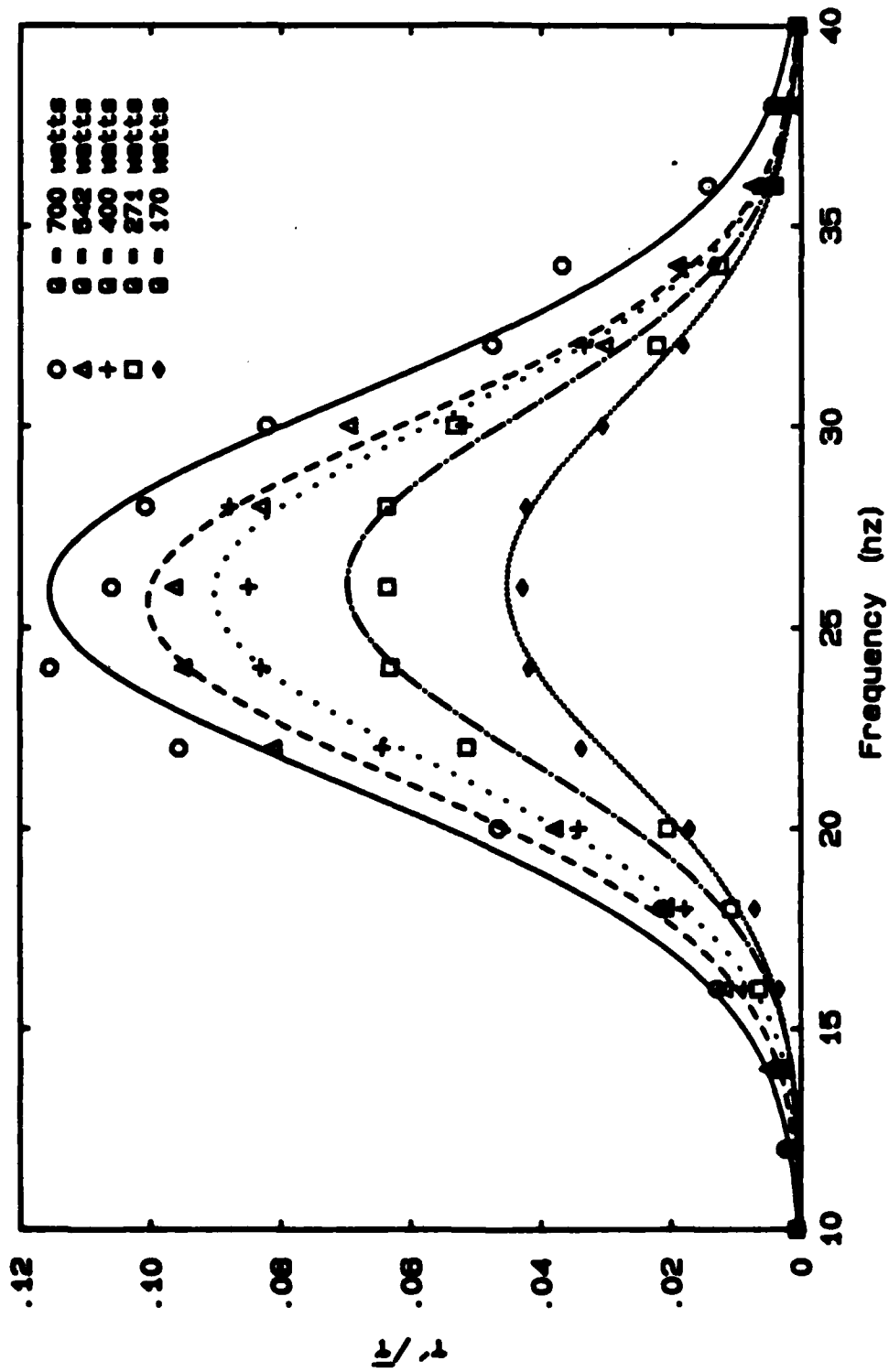


Figure 3.10 Frequency Dependence

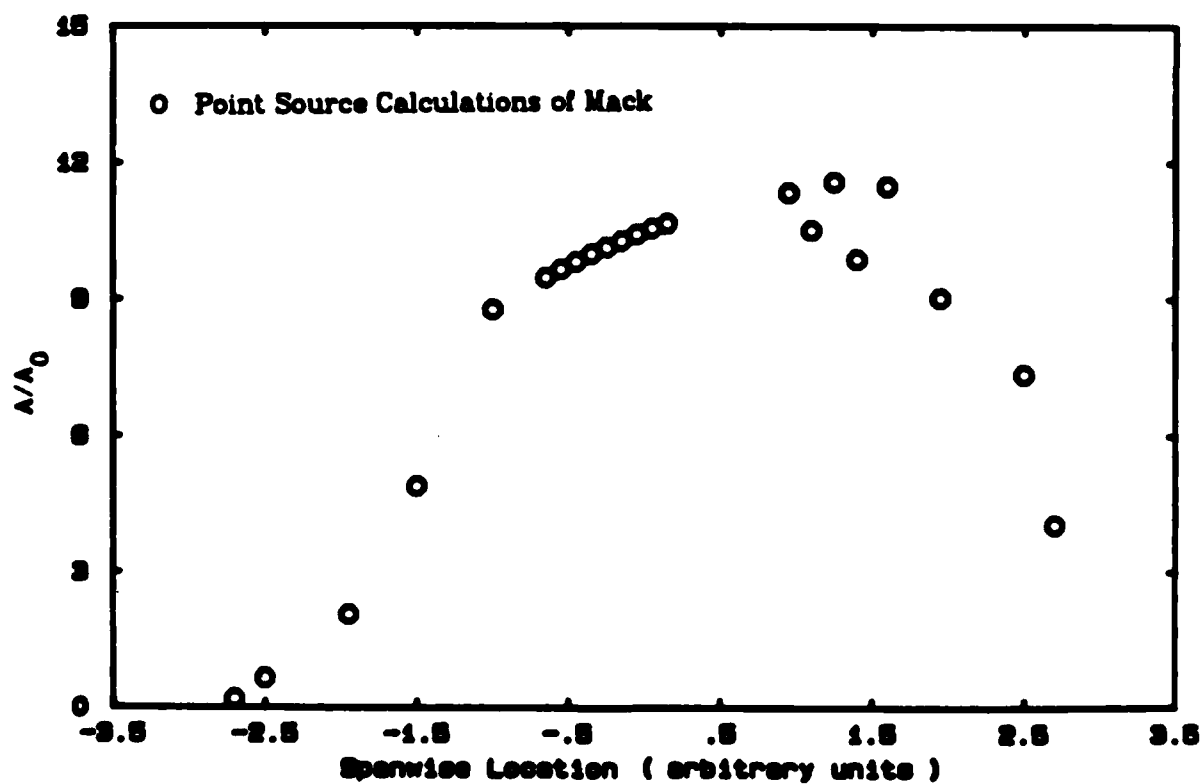
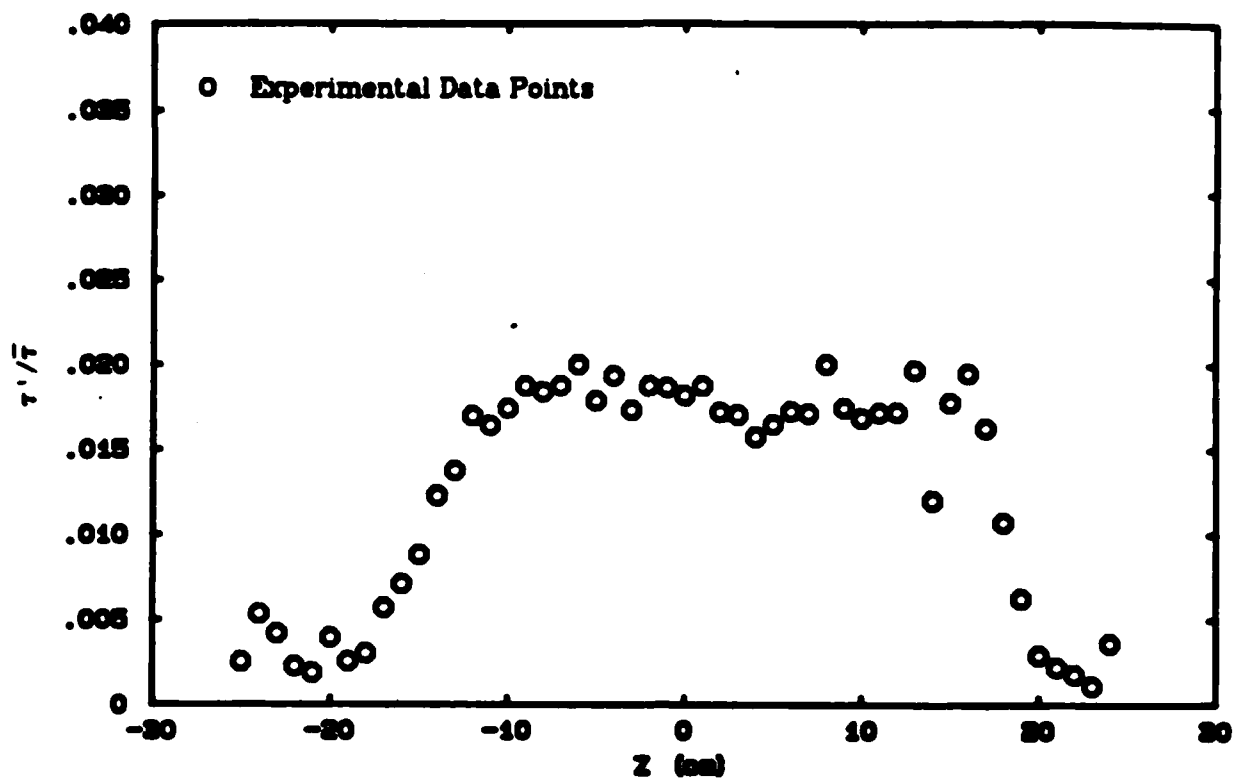


Figure 4.1 Spanwise Amplitude Distribution for a Single Oblique Mode

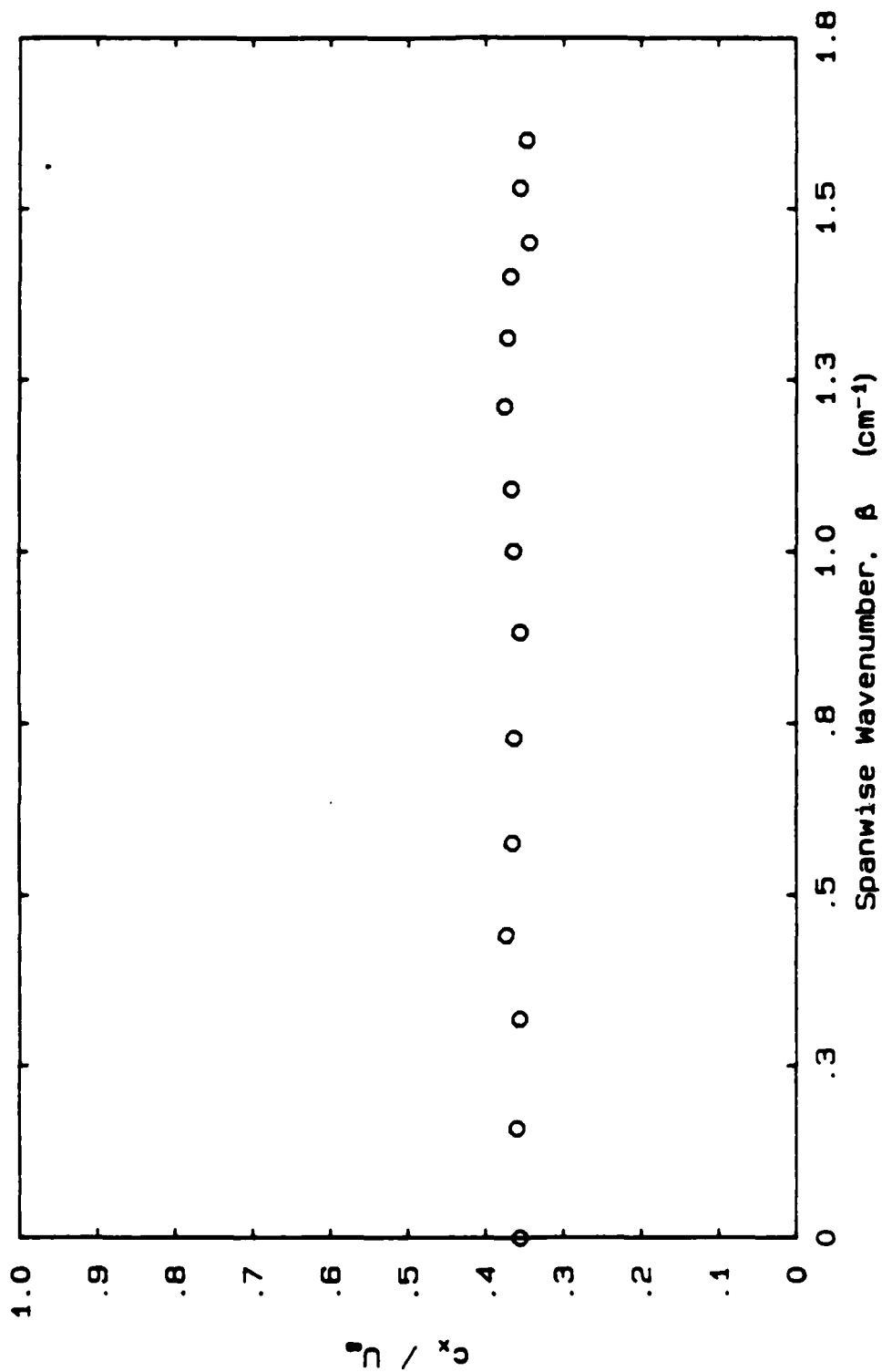


Figure 4.2 Phase Velocity vs. Spanwise Wavenumber

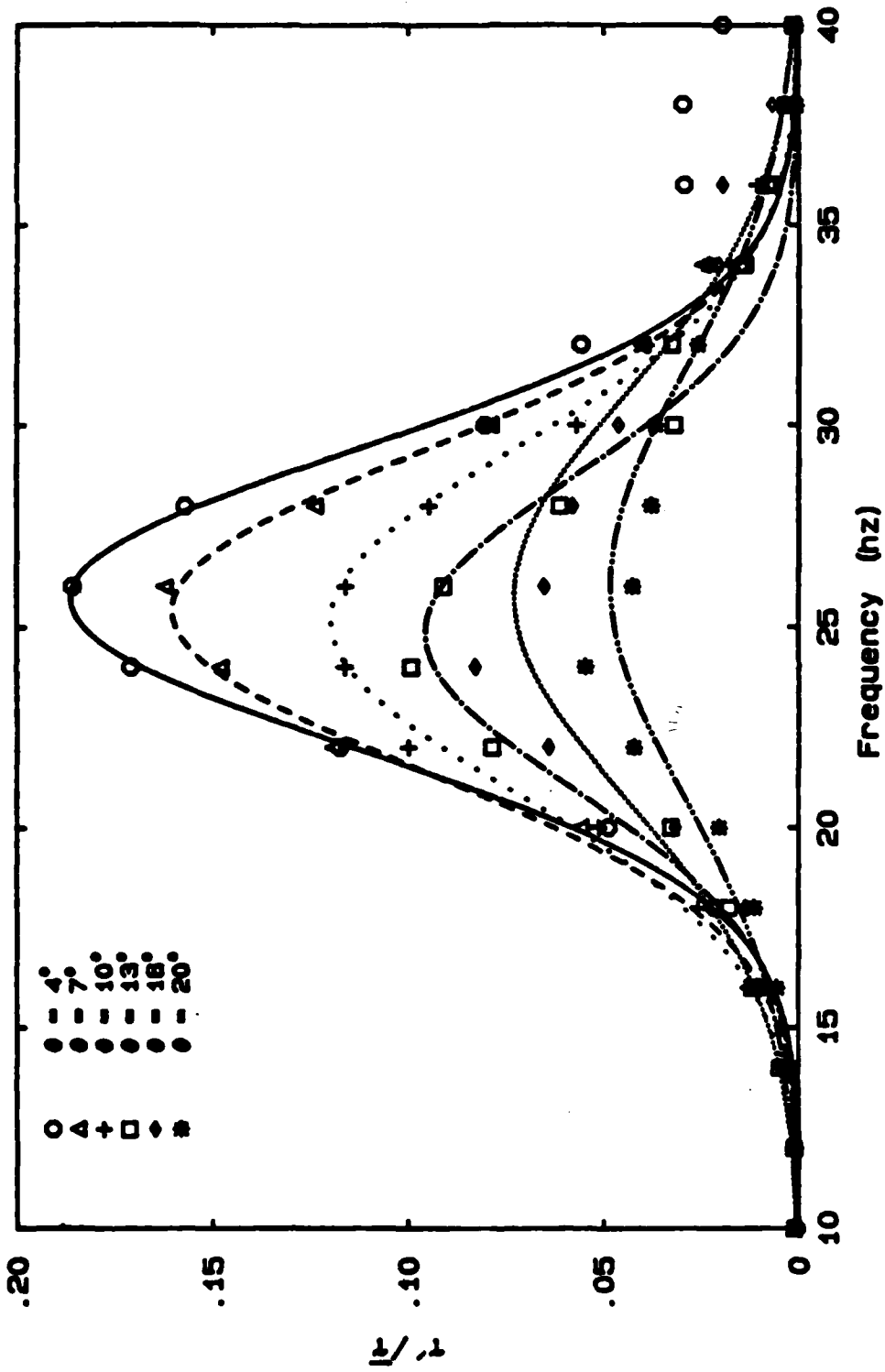


Figure 5.1 Disturbance Amplitude vs. Frequency for Oblique Waves

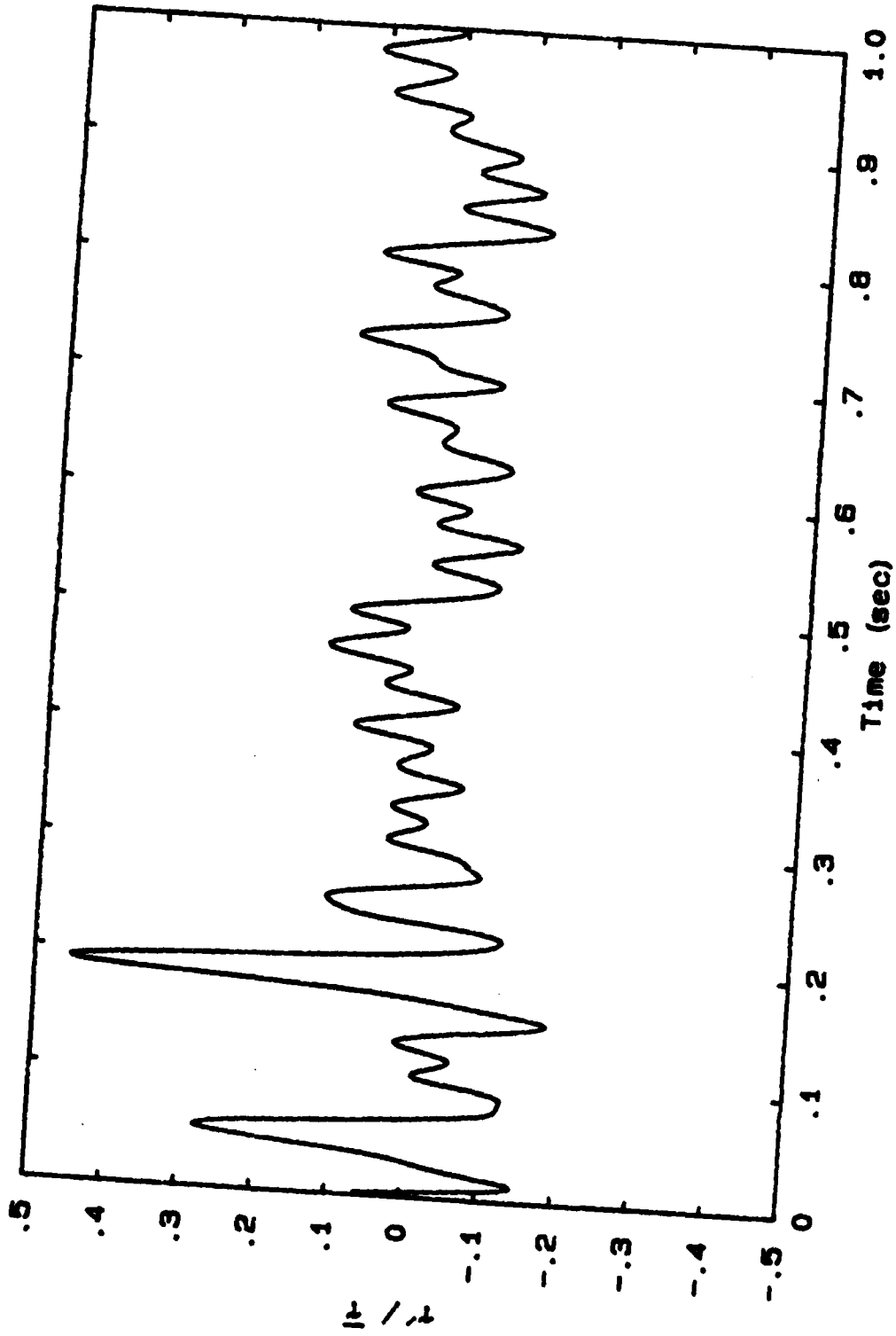


Figure 5.2 Non-Stationarity of Time-Series for a 15° Oblique Wave

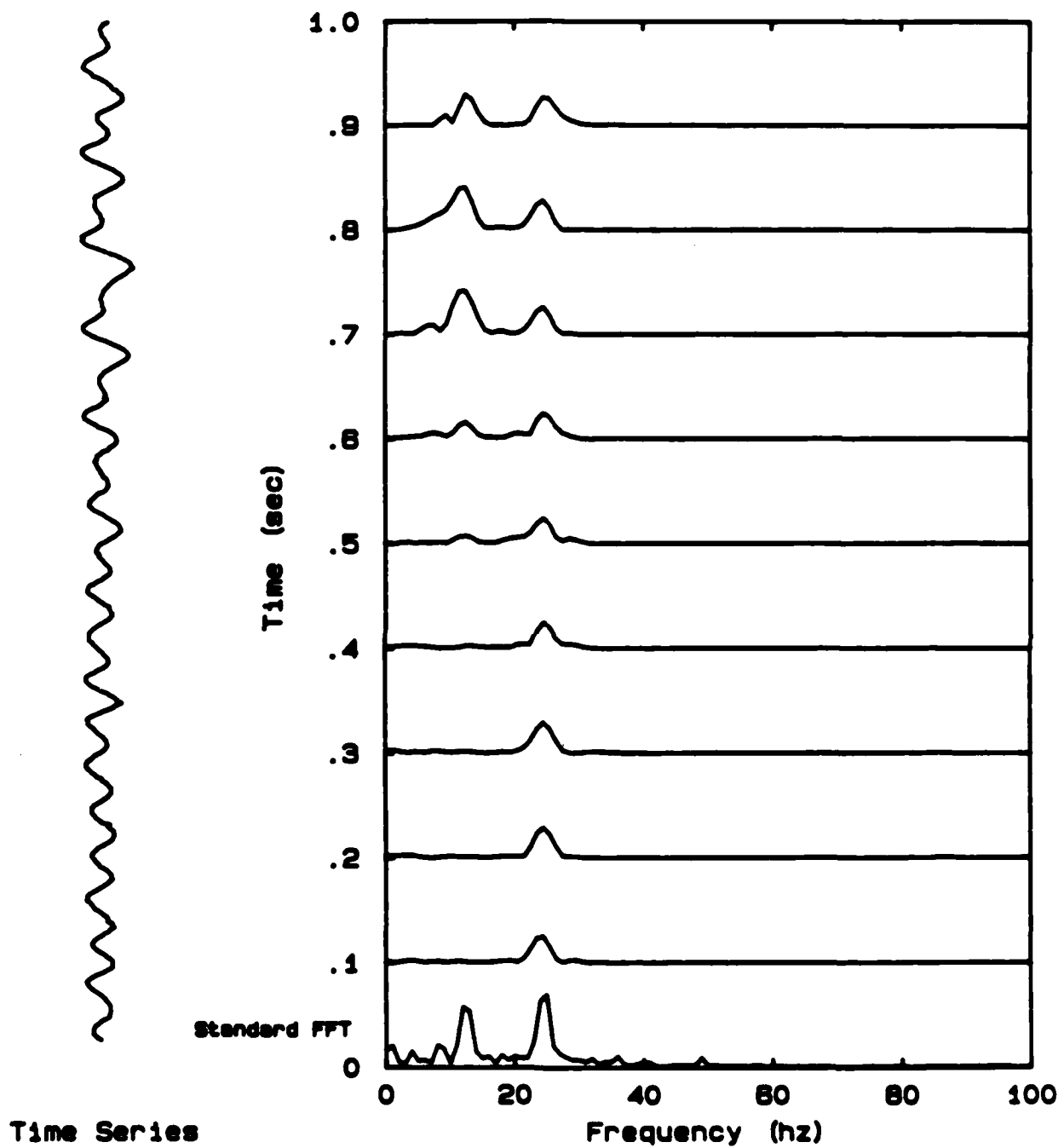
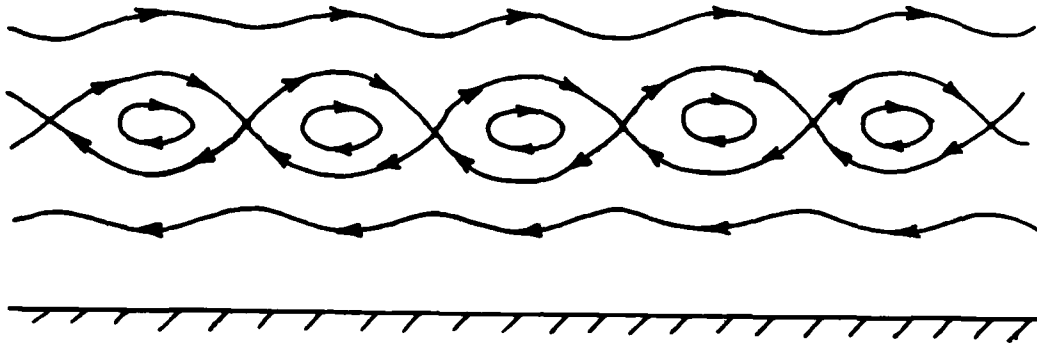


Figure 5.3 Wigner Transform of a Non-Stationary Time-Series



Typical "Cat's eye" Streamline Pattern

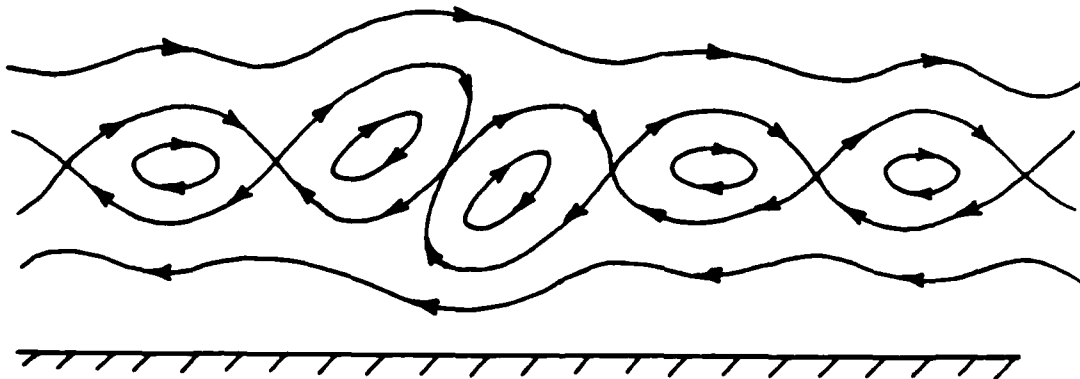


Figure 5.4 Altered Streamline Pattern Due to Vortex Pairing

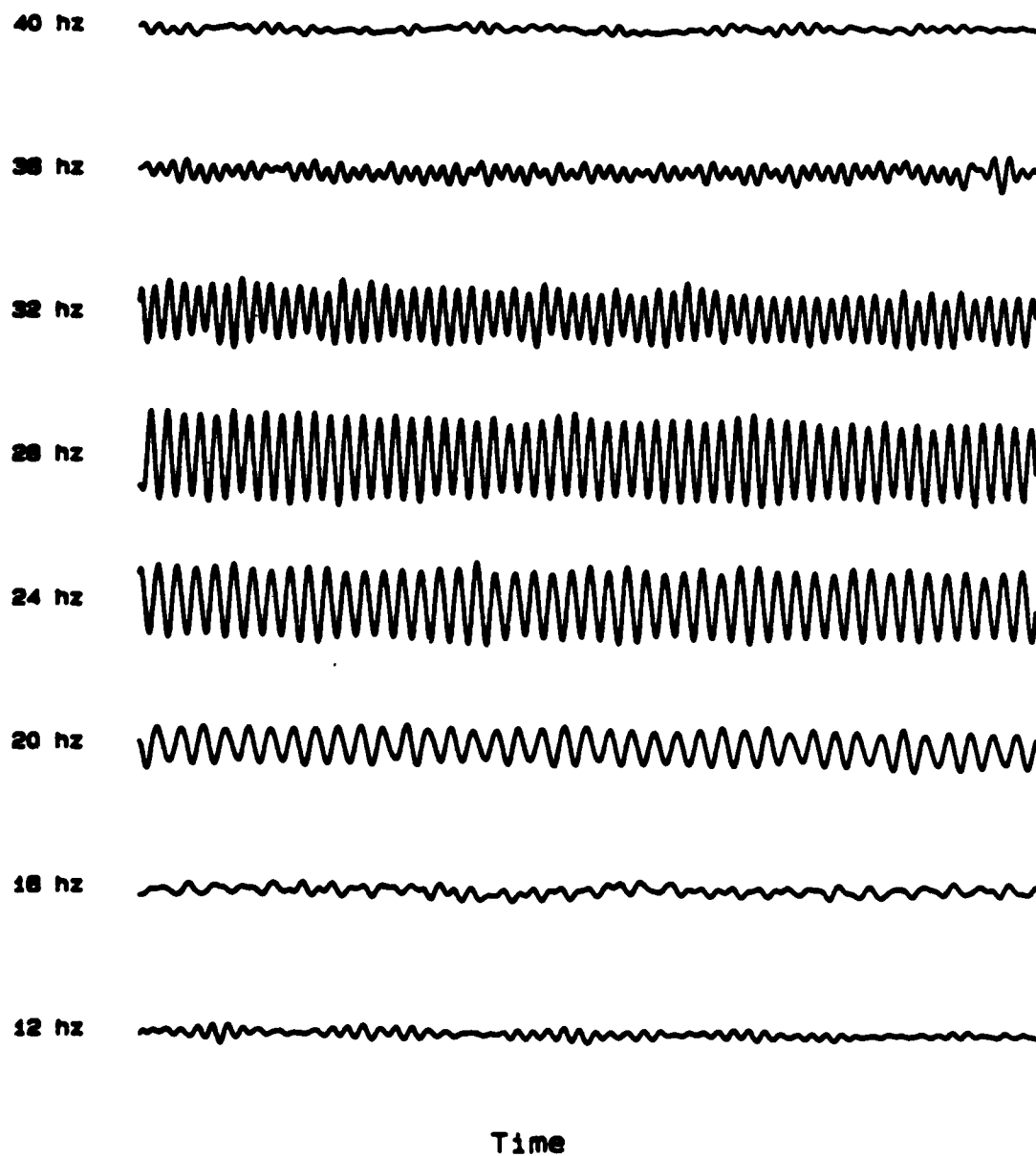


Figure 5.5 Time-Series Response vs. Forcing Frequency for Two-Dimensional Waves

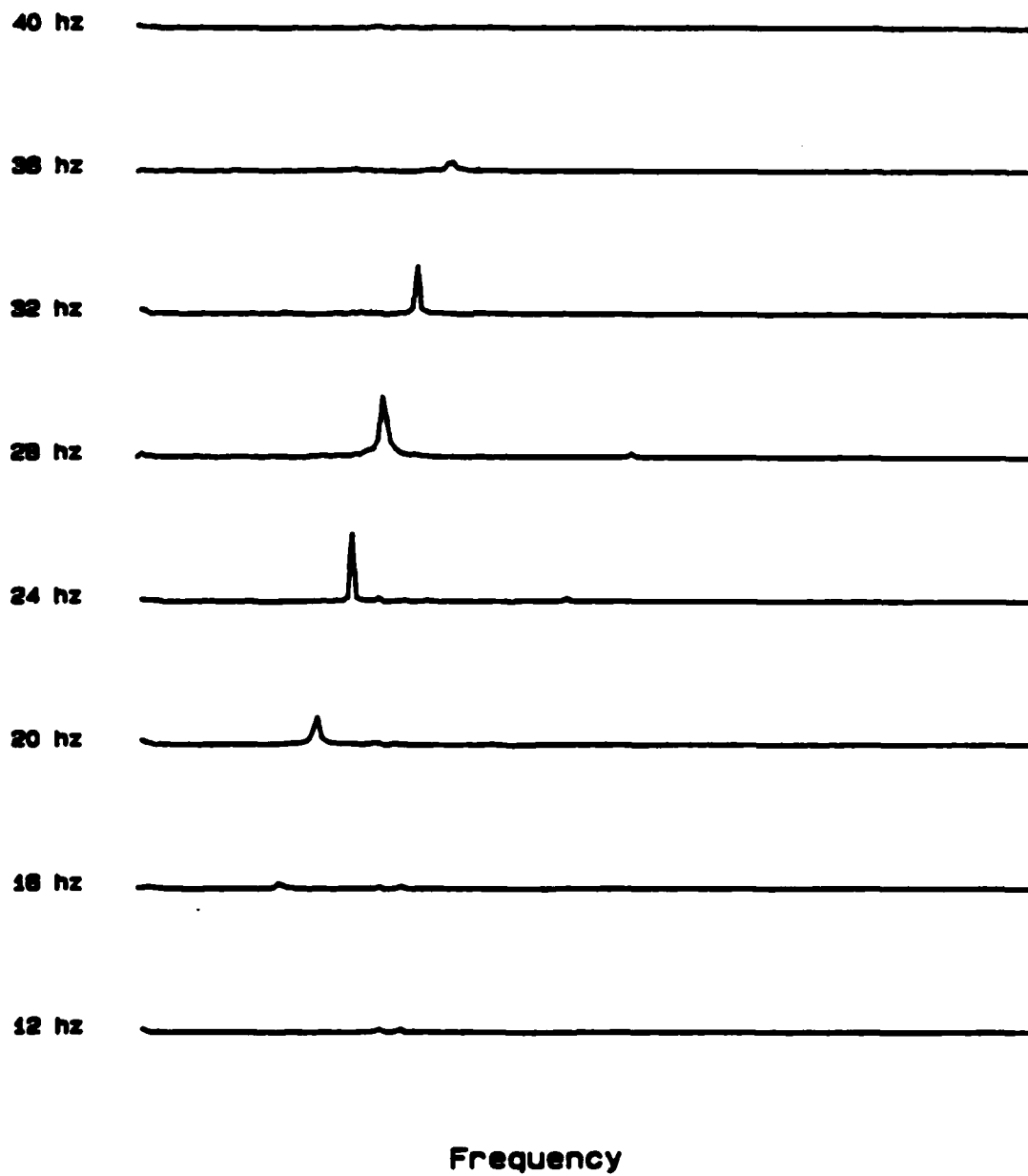


Figure 5.6 Spectral Response vs. Forcing Frequency for Two-Dimensional Waves

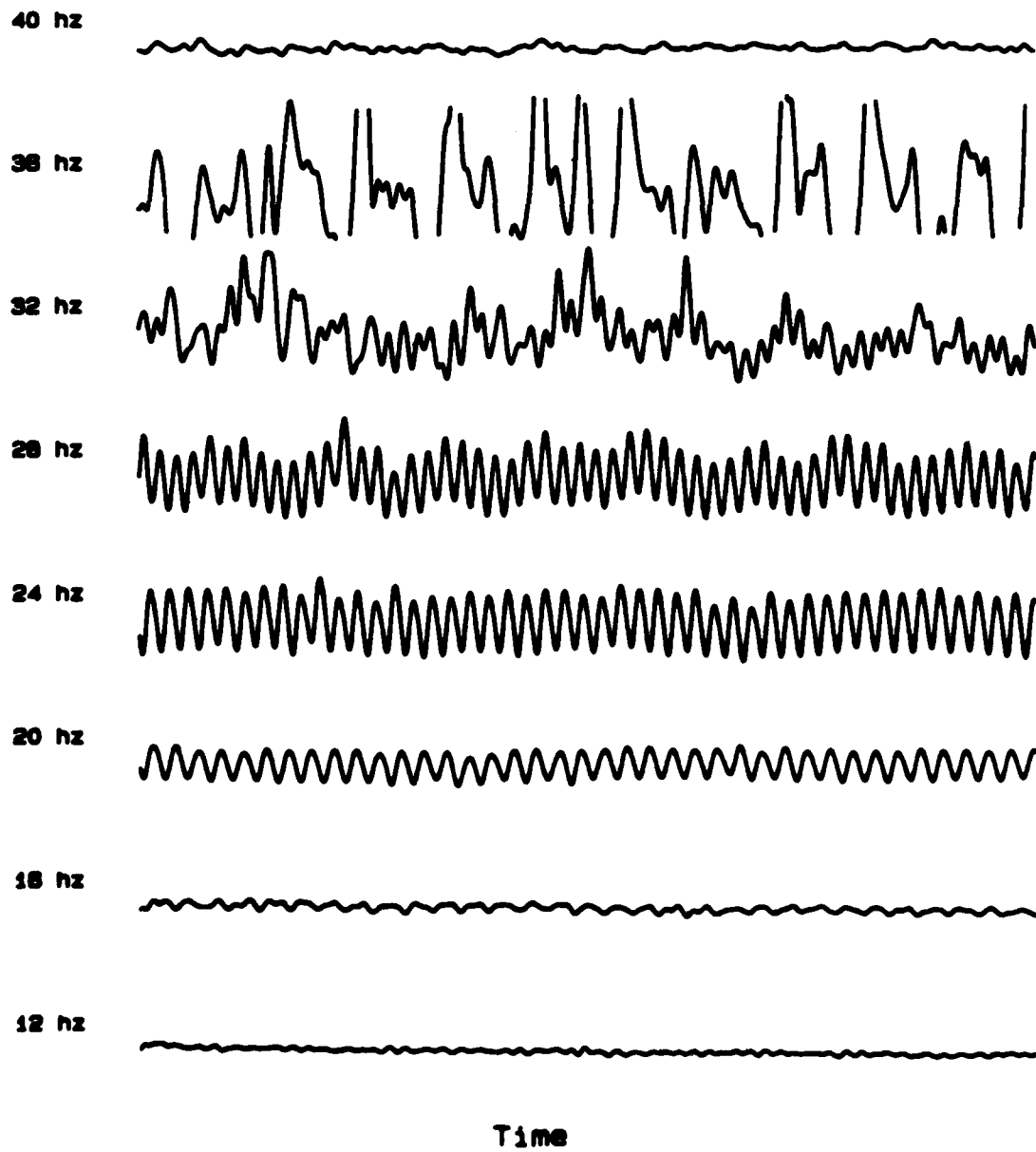


Figure 5.7 Time-Series Response vs. Forcing Frequency for 10° Oblique Waves

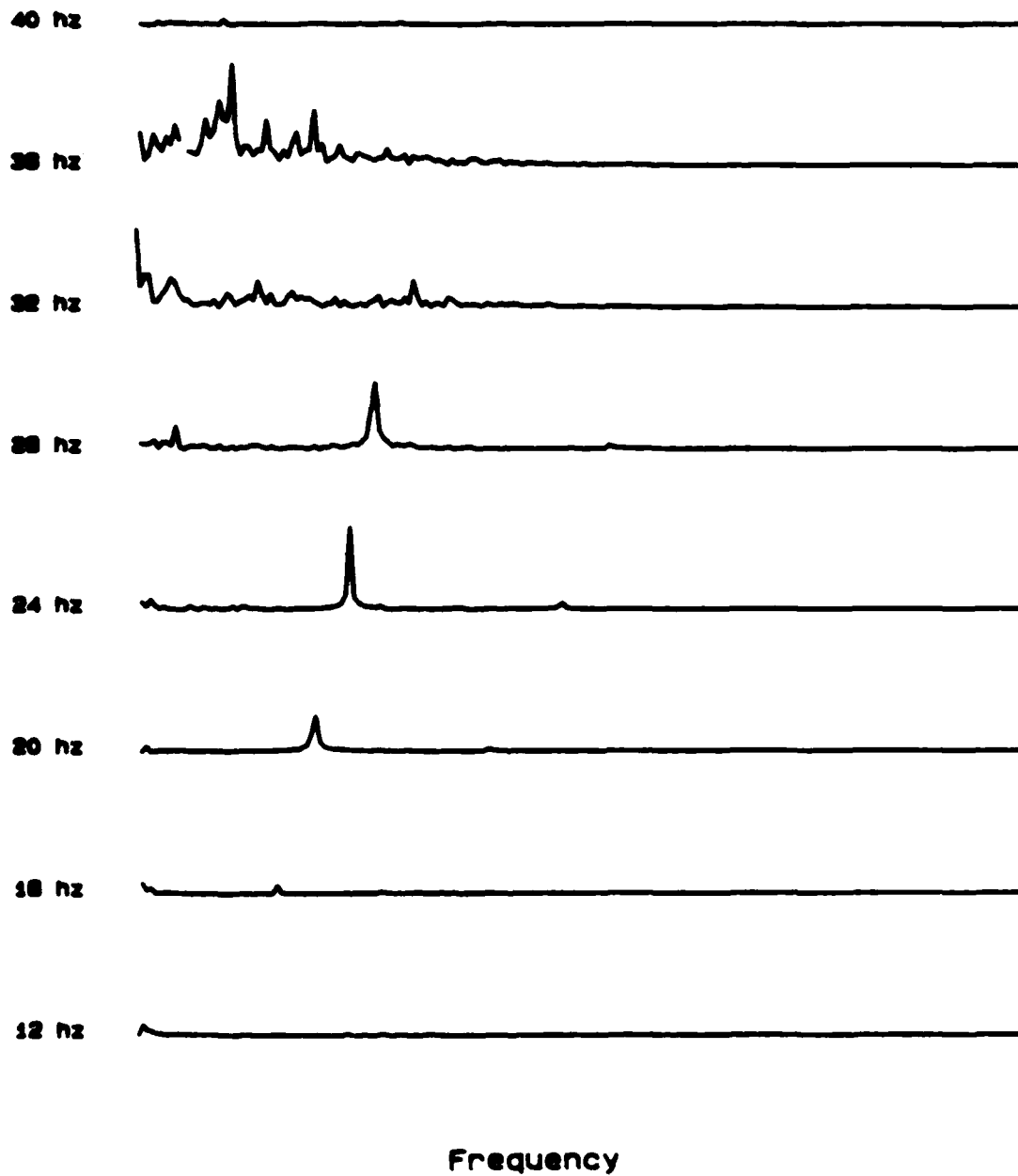


Figure 5.8 Spectral Response vs. Forcing Frequency for 10° Oblique Waves

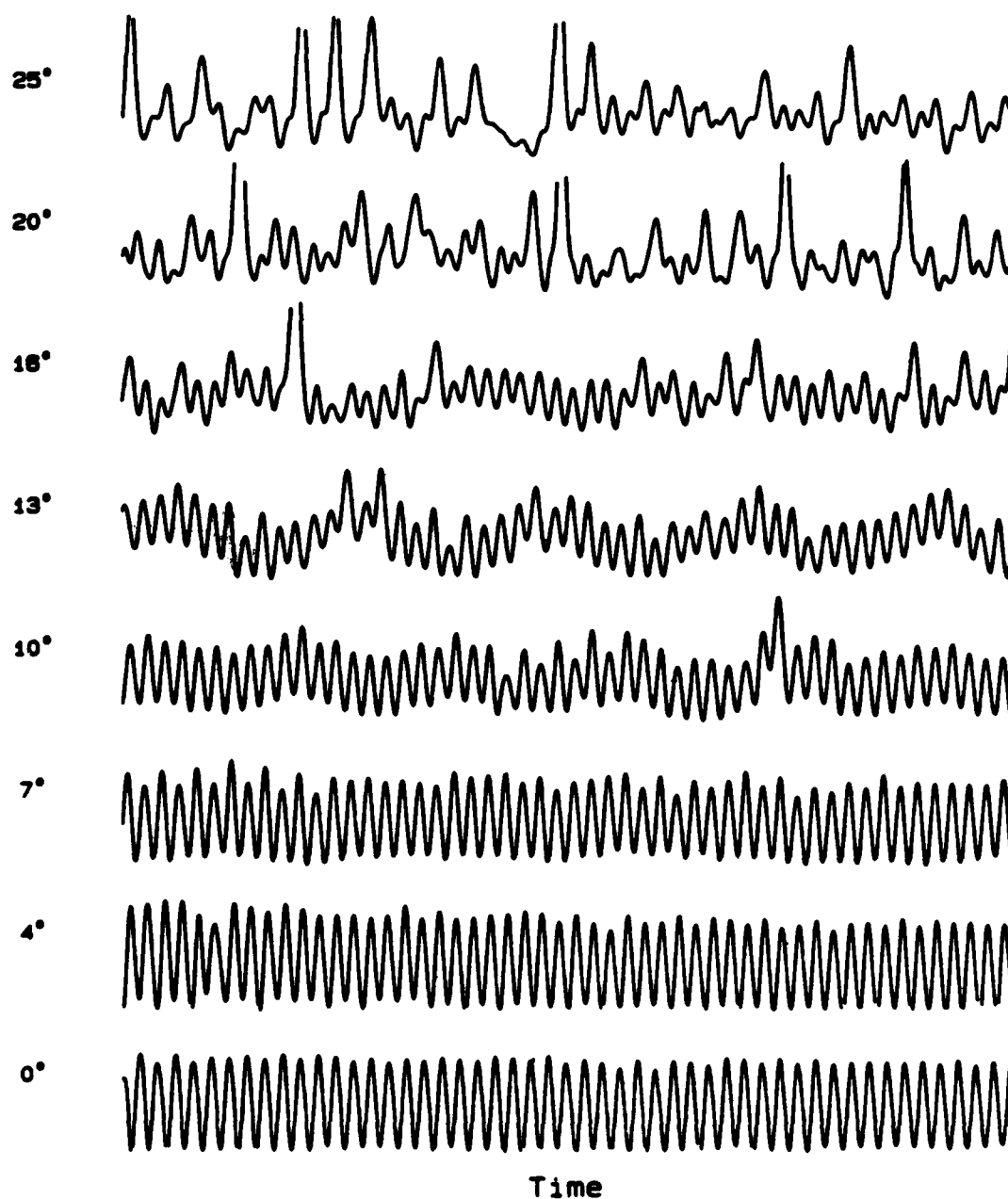


Figure 5.9 Time-Series Response vs. Wave Angle

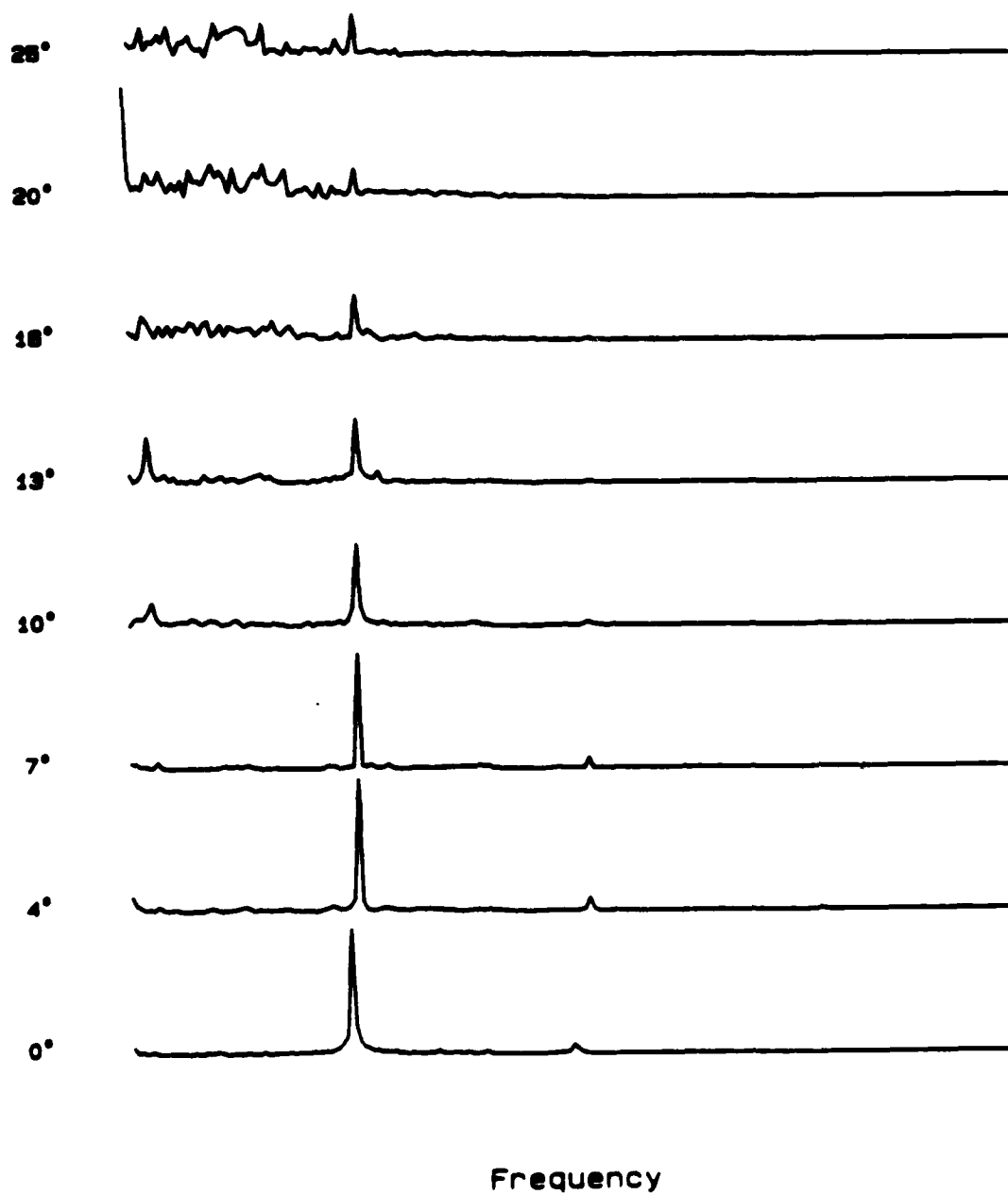


Figure 5.10 Spectral Response vs. Wave Angle

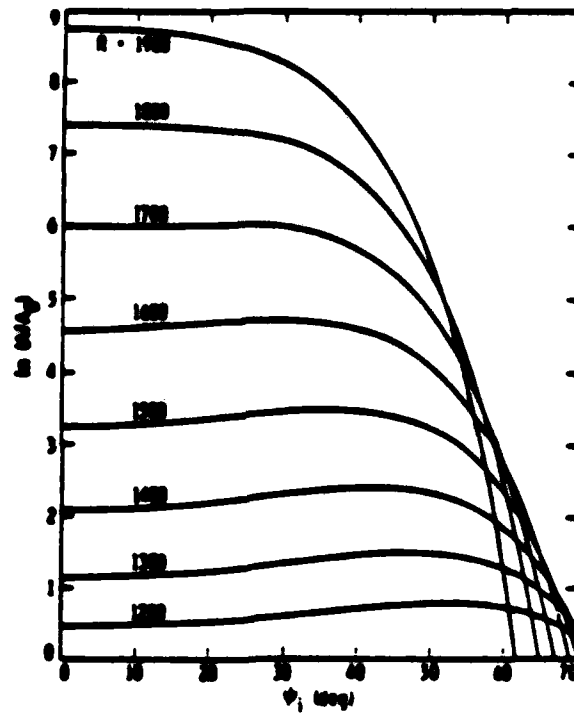


Figure S.11 Integrated Amplification vs. Wave Angle (Mack)

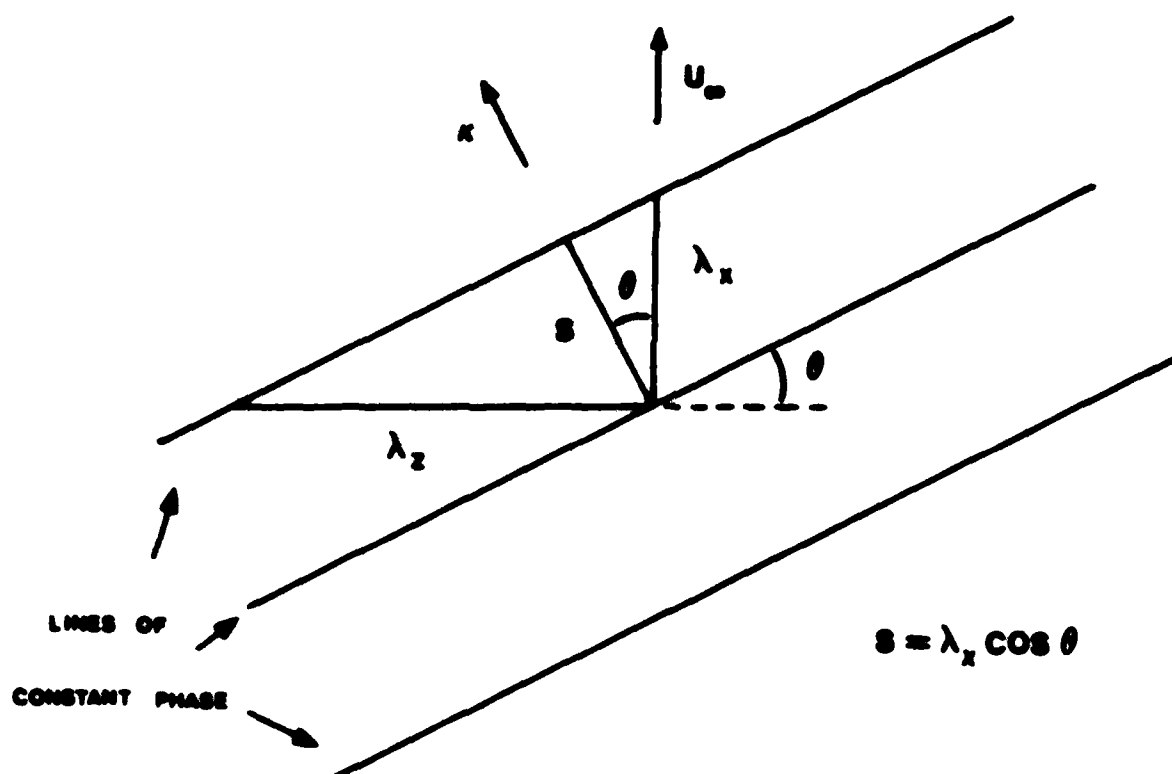


Figure 8.12 Geometry of Oblique Waves

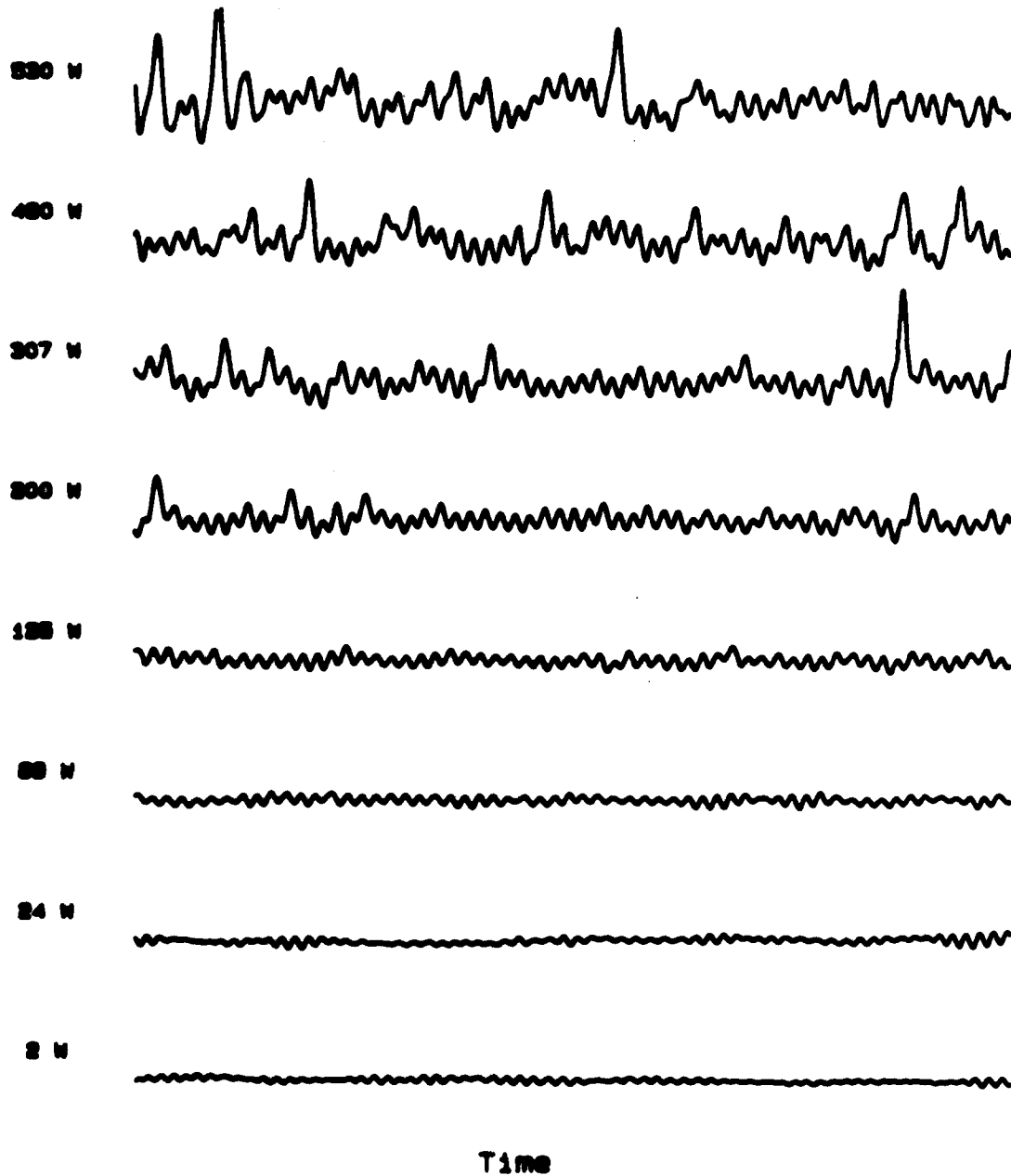


Figure 5.13 Time-Series Response vs. Forcing Amplitude

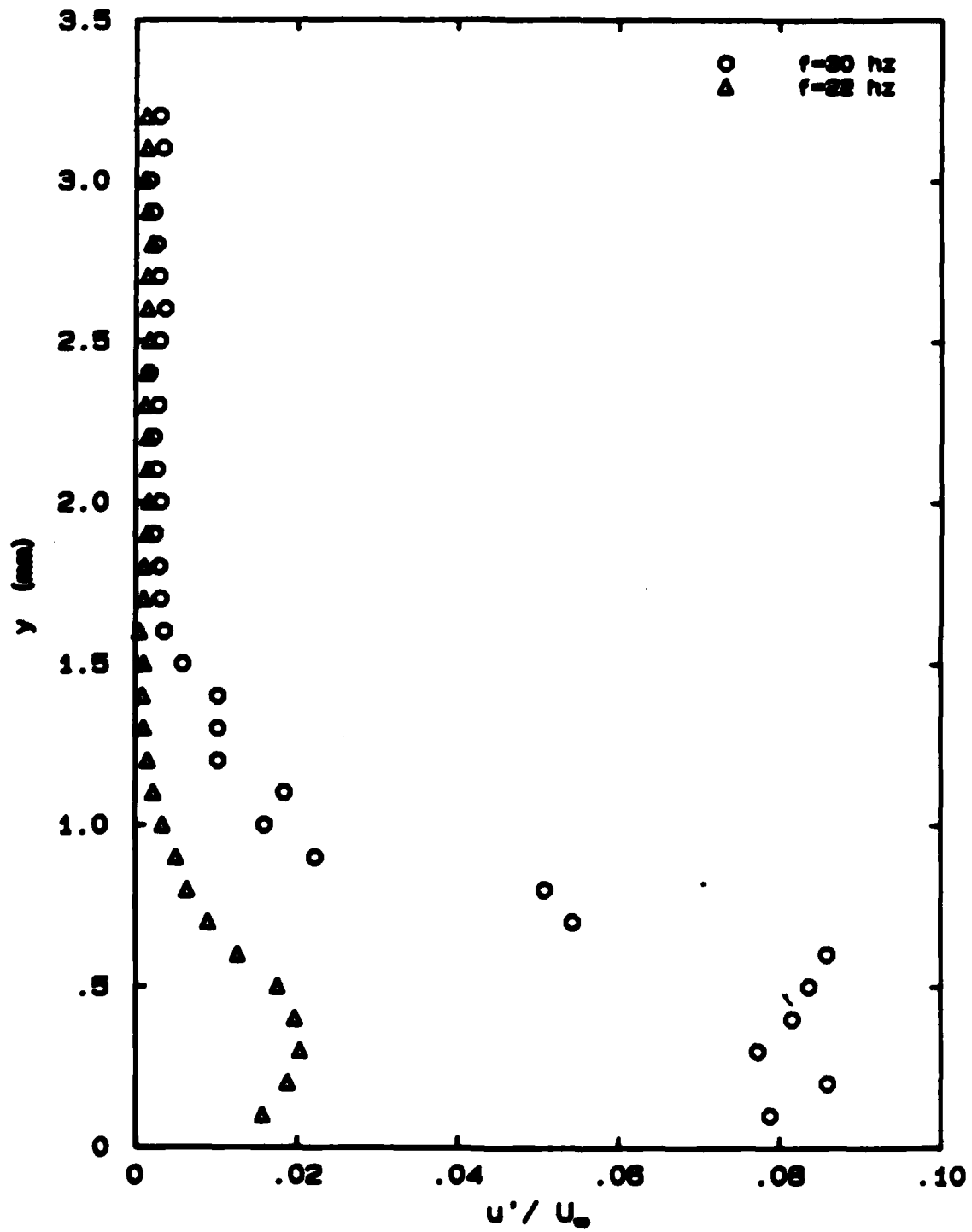


Figure 5.14 Eigenfunction Behavior of Oblique Waves

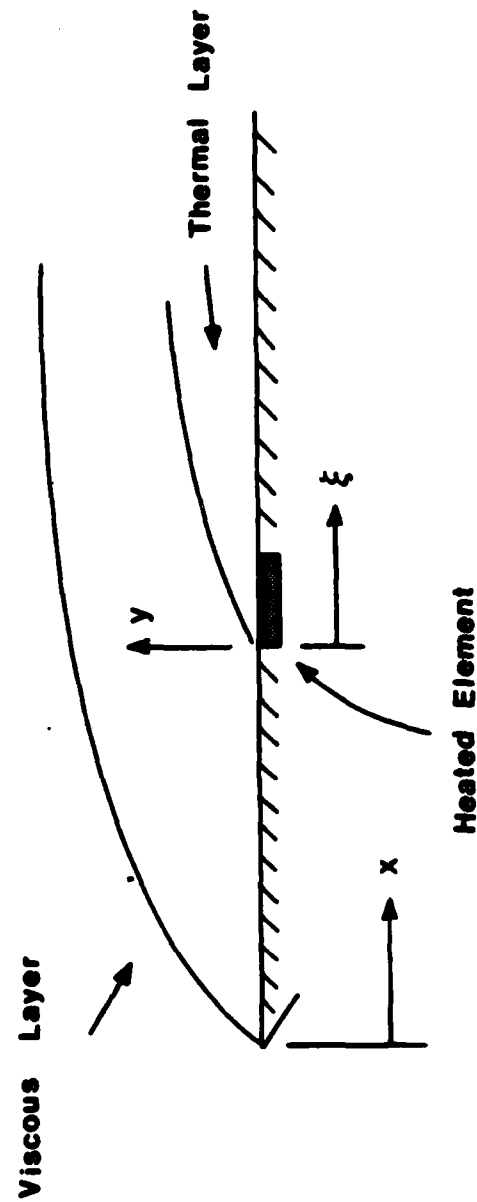


Figure A.1 Geometry for Similarity Analysis of Surface Heating Technique

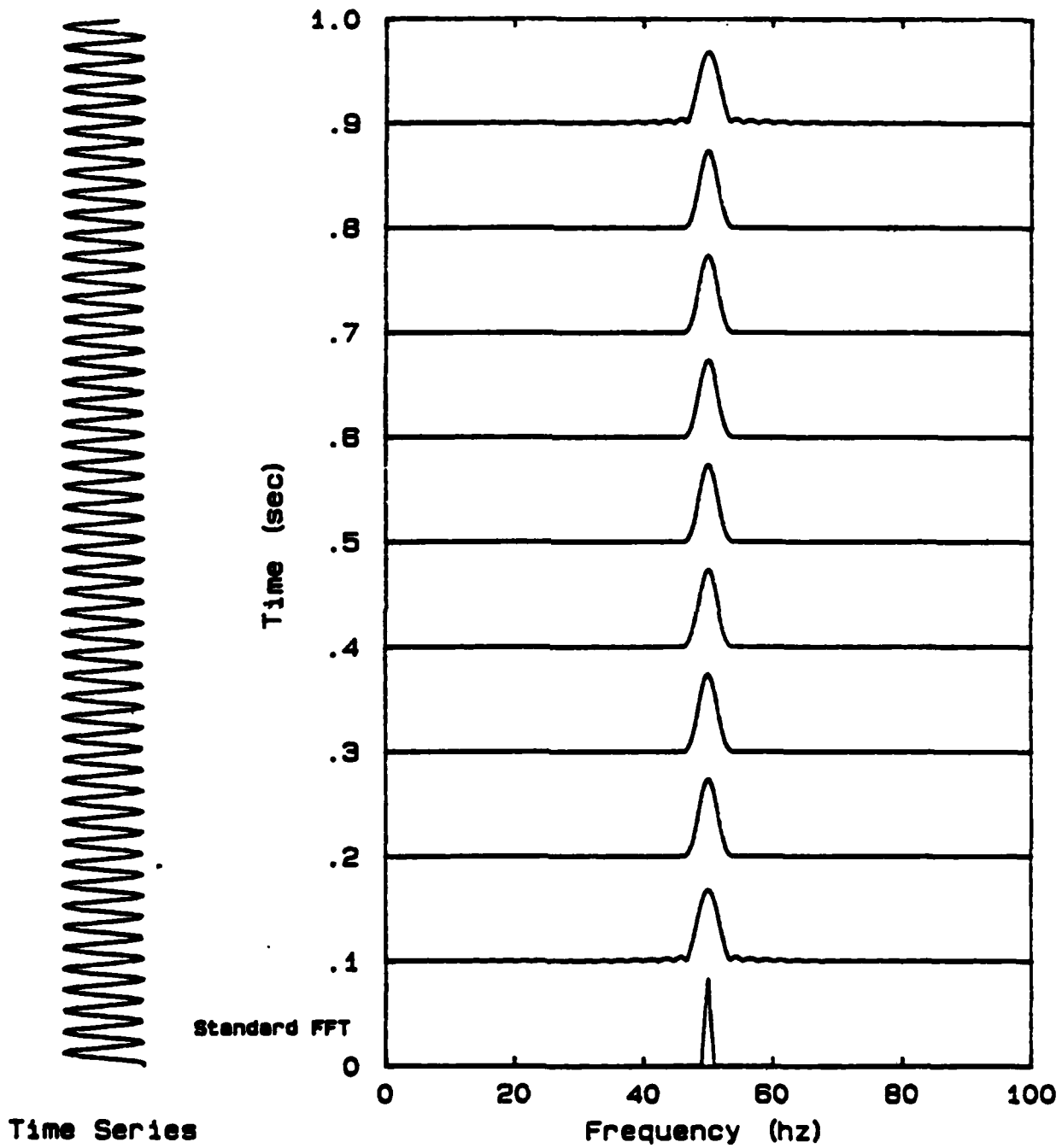


Figure B.1 Wigner Transform of a Stationary Signal

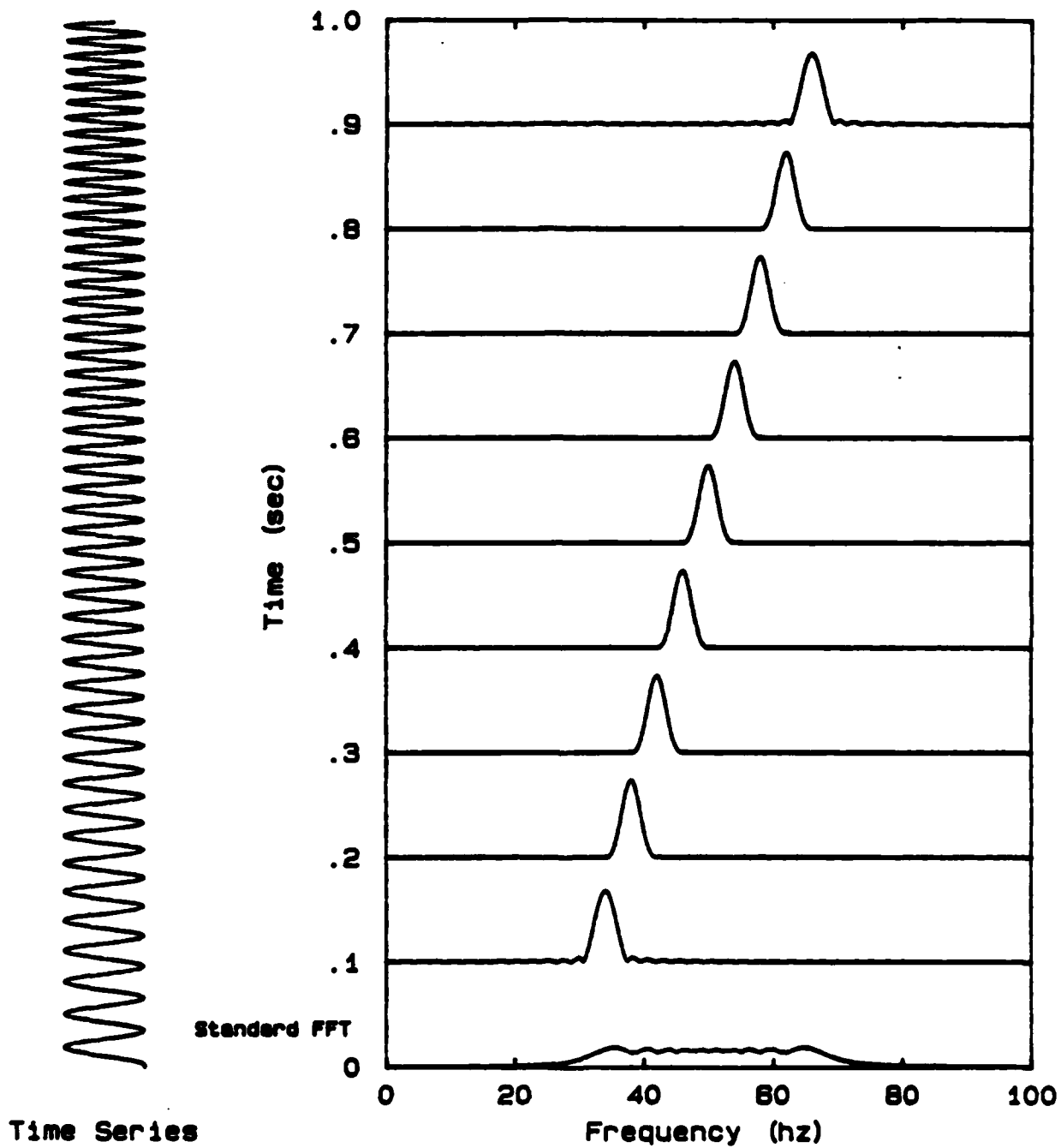


Figure B.2 Wigner Transform of a Non-Stationary Signal

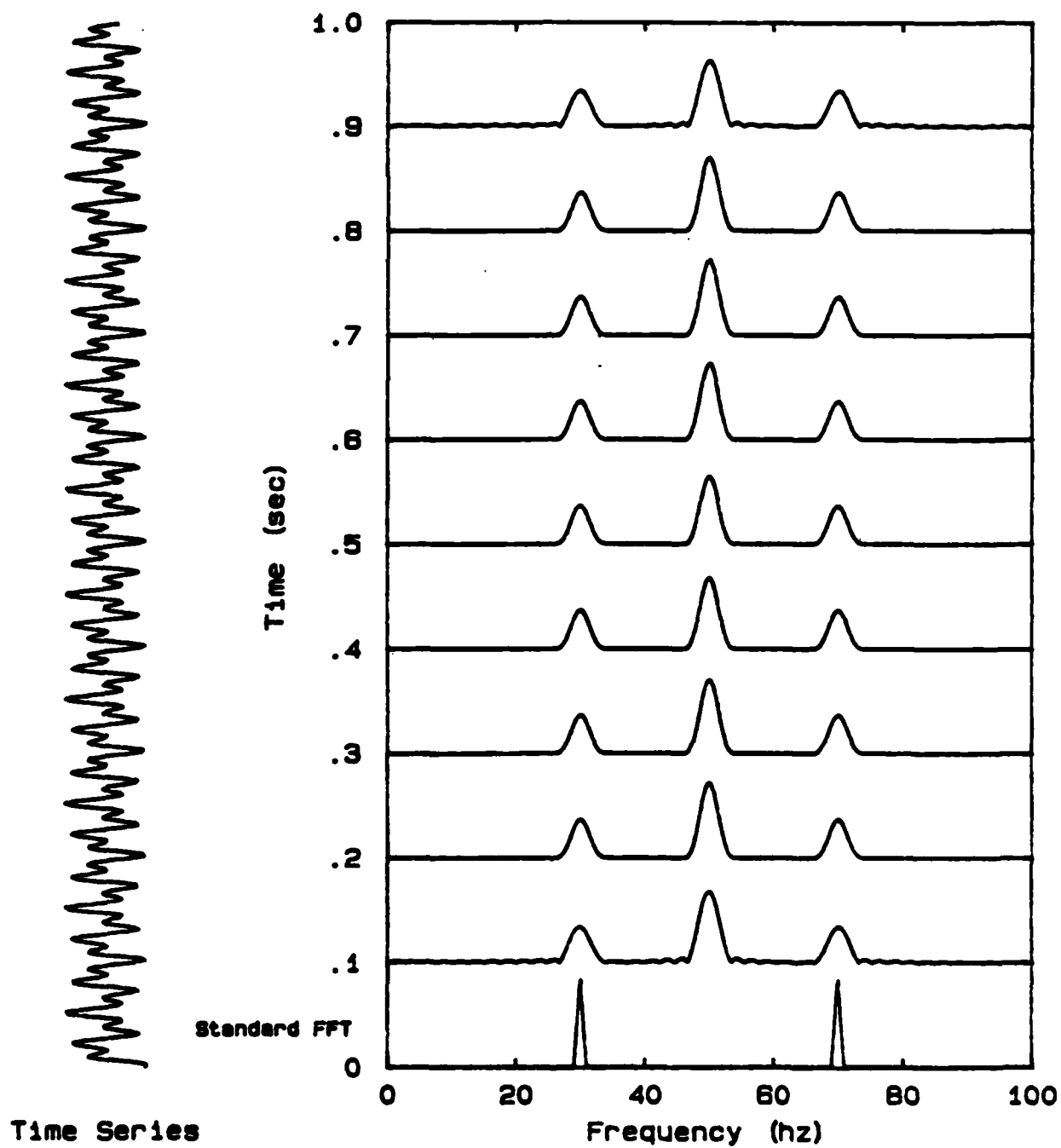


Figure B.3 Wigner Transform of a Signal Composed of Two Stationary Contributions

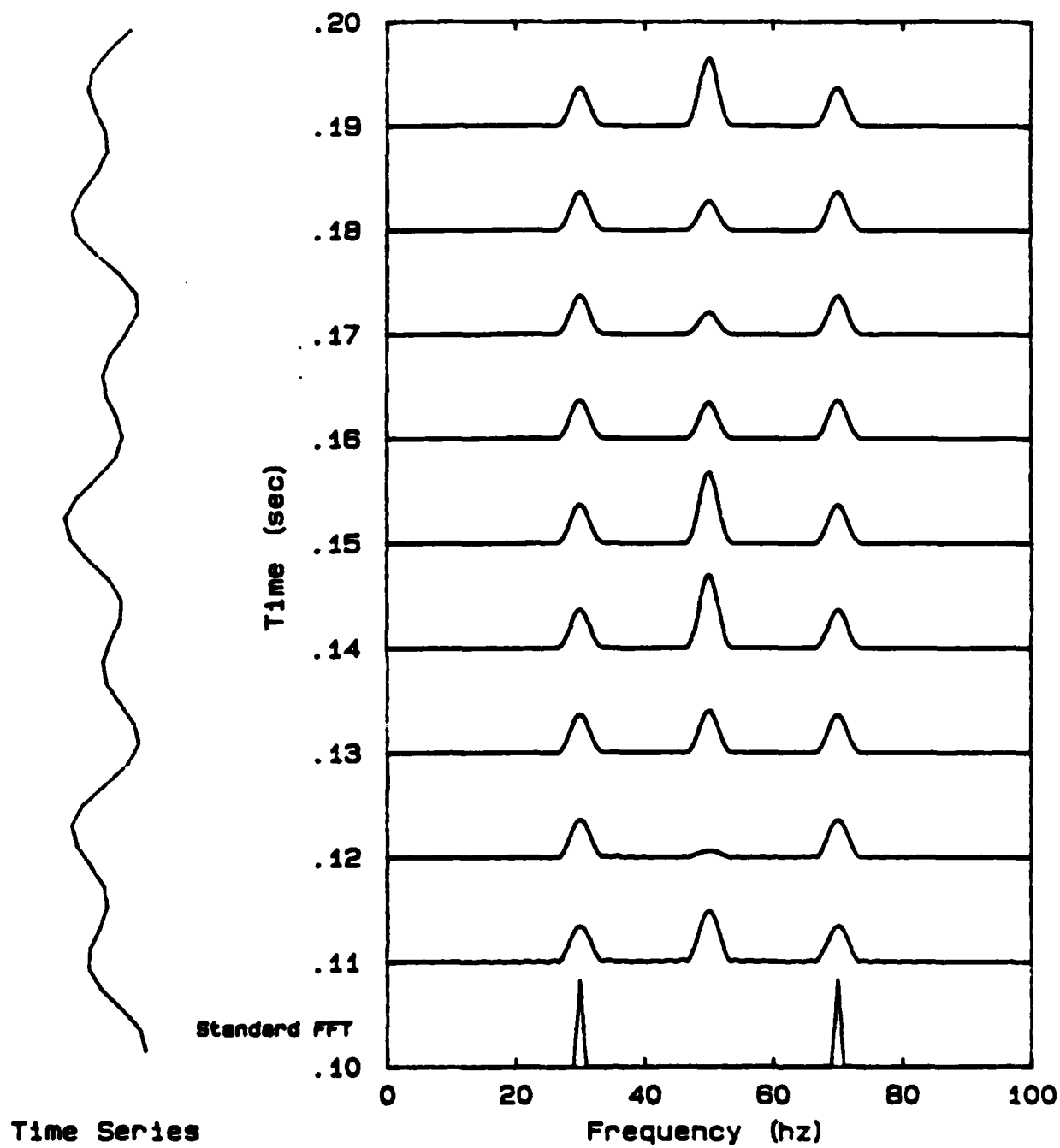


Figure B.4 A Detailed Look at the Wigner Transform of Figure B.3

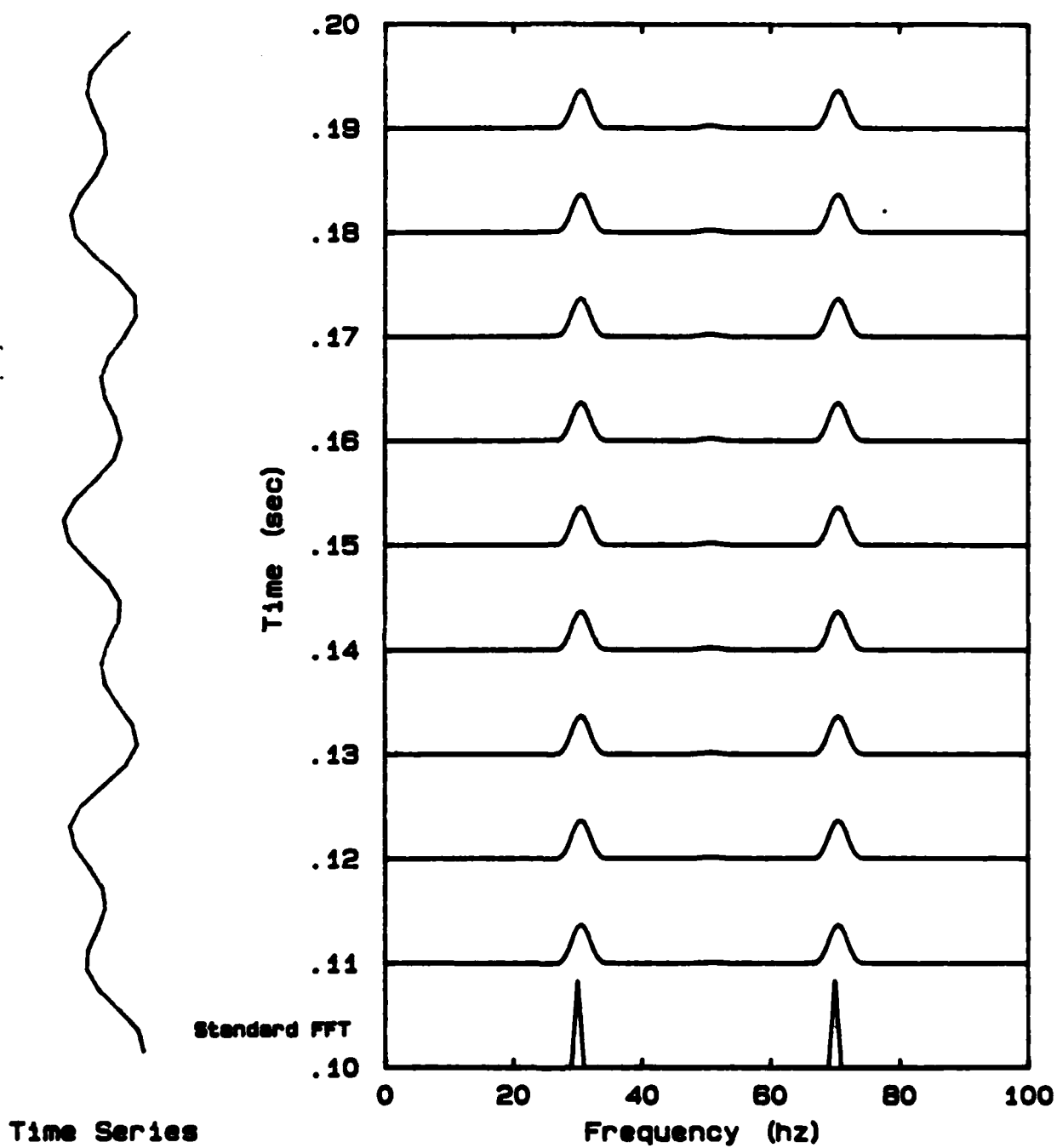


Figure B.5 The Result of Low-Pass Filtering on the Wigner Transform

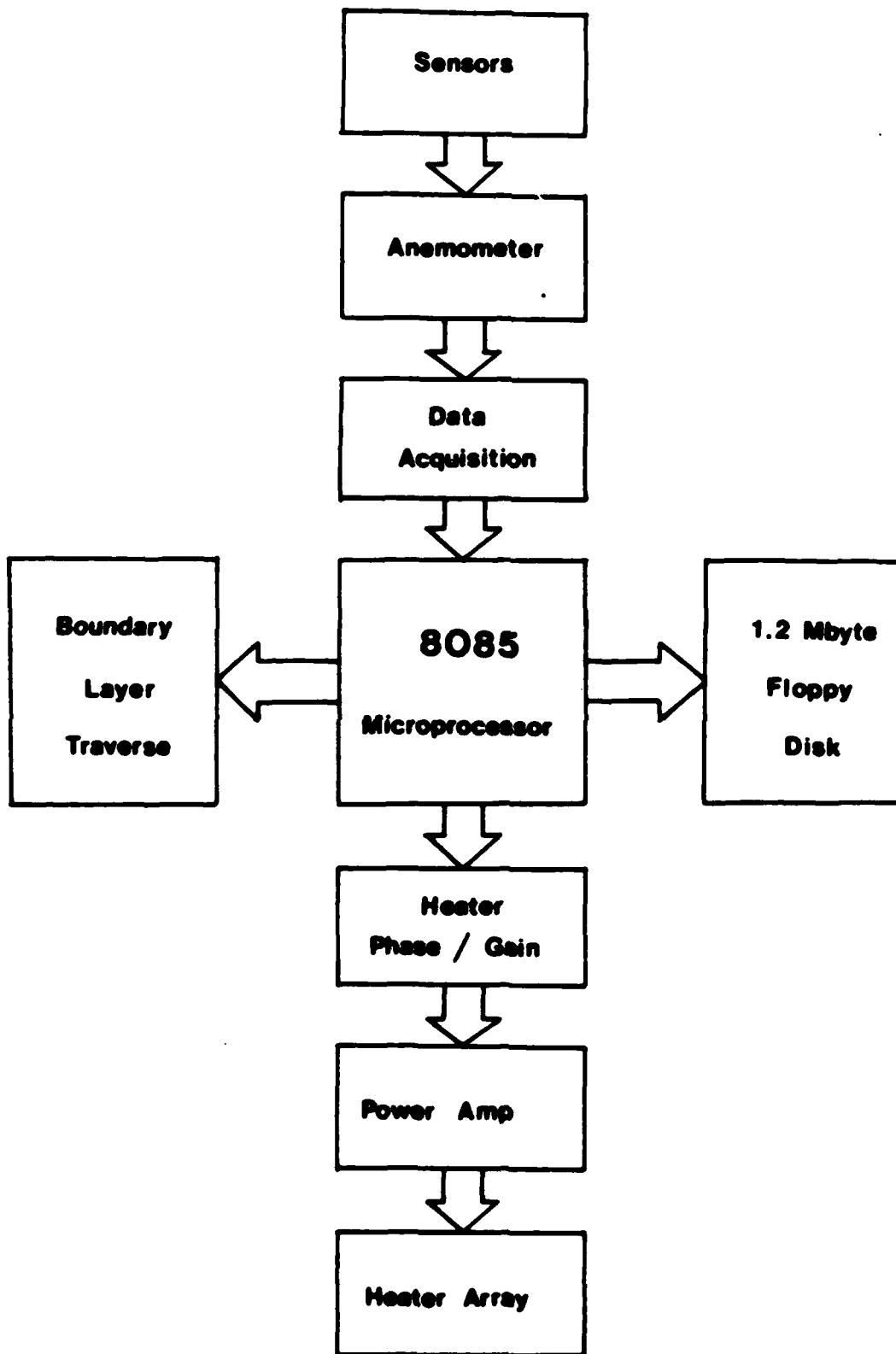


Figure C.1 Experimental Aparatus

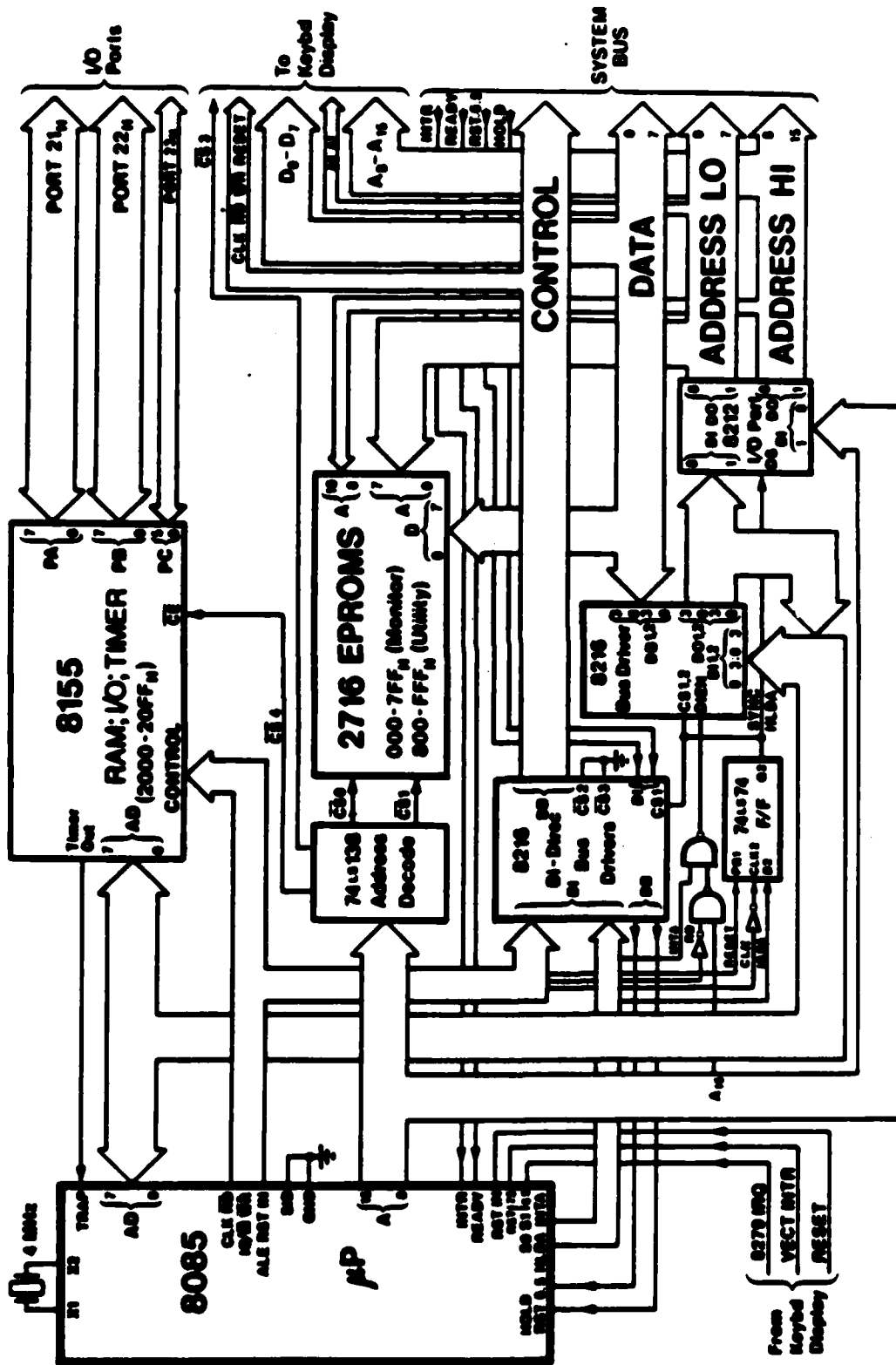


Figure C.2 Block Diagram of the Central Processing Unit (CPU)

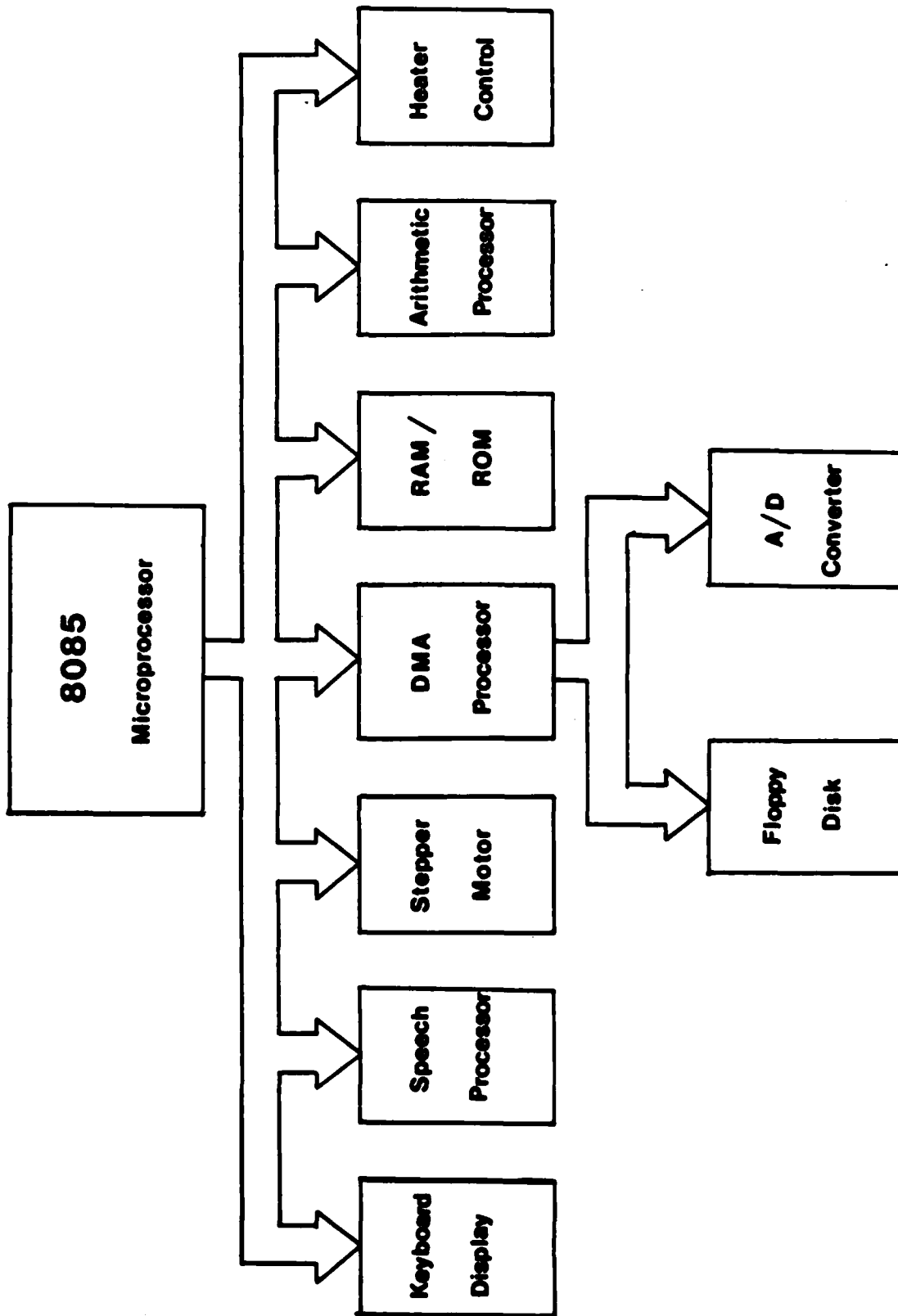


Figure C.3 Block Diagram of the CPU/Peripheral Interface

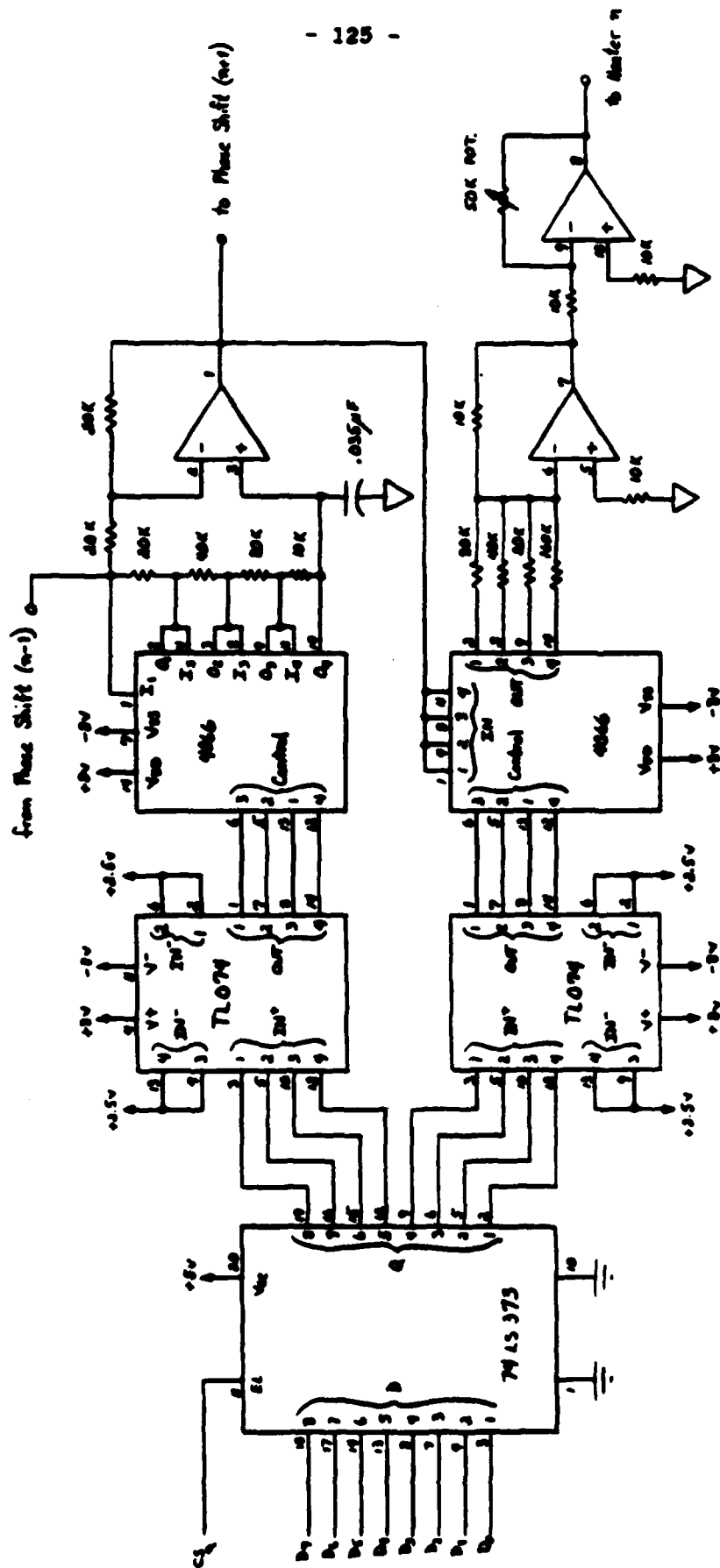


Figure C.4 Circuit Diagram of the Phased Heater Control Electronics

END

FILMED

MARCH, 19 88

DTIC